Hydraulic load reduction as a function of depth in a filter layer consisting of logs

MSc Thesis report

July 2018

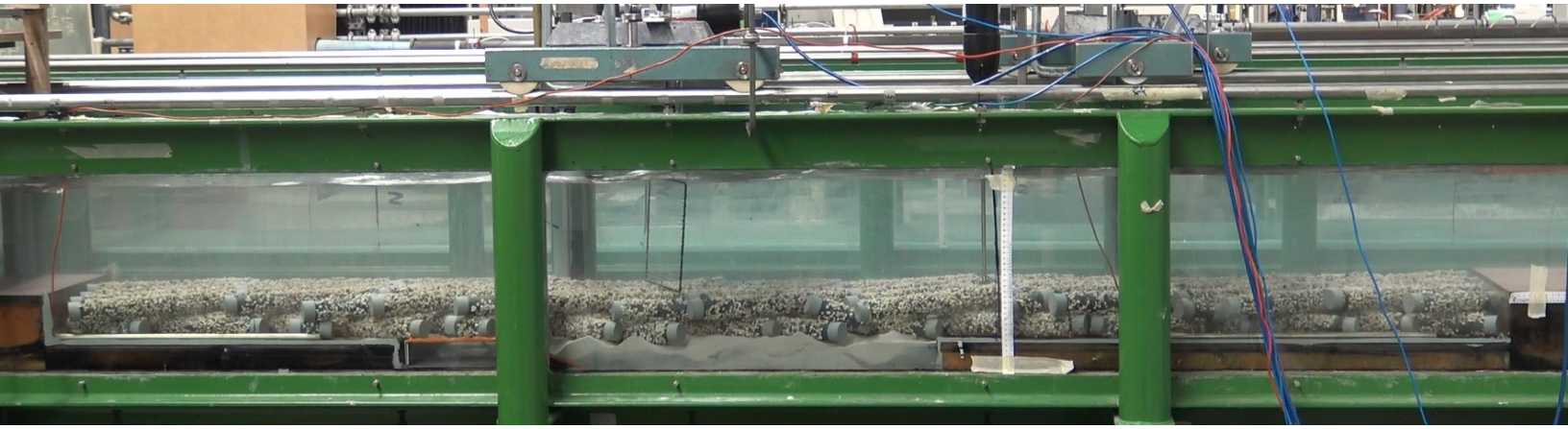

Name:
R.M. Rubaij Bouman

Supervisors:

Prof. dr. ir. W.S.J. Uijttewaal	Delft Universiy of Technology
Ir. H.J. Verhagen	Delft Universiy of Technology
Dr. ir. J.D. Bricker	Delft Universiy of Technology
Dr. ir. A. Sieben	Rijkswaterstaat

TU Delft

Deltares
Enabling Delta Life

Rijkswaterstaat
Ministerie van Infrastructuur en Milieu

Hydraulic load reduction as a function of depth in a filter layer consisting of logs

by

Roland Rubaij Bouman

in partial fulfillment of the requirements for the degree of

Master of Science

in *Civil Engineering*

at the Delft University of Technology,

to be defended publicly on Thursday July 12, 2018 at 2:00 PM.

Thesis committee:

Prof. dr. ir. W.S.J. Uijttewaal	Delft Universiy of Technology
Ir. H.J. Verhagen	Delft Universiy of Technology
Dr. ir. J.D. Bricker	Delft Universiy of Technology
Ir. A. Sieben	Rijkswaterstaat

Acknowledgements

I would like to thank my supervisors from the Delft University of Technology, Wim Uijttewaal, Henk-Jan Verhagen, for helping me and steering me in the right direction during the progress meetings. Subsequently, I especially want to thank Jeremy Bricker for his weekly support and sympathy when something went wrong during the experimental set-up.

In addition, I would like to express gratitude to Arjan Sieben on behalf of Rijkswaterstaat and Gijs Hoffmans on behalf of Deltares for sharing their knowledge during my master thesis.

Also, I would like to thank the staff in the Fluid Mechanics Laboratory, Sander de Vree, Frank Kalkman, Arno Doorn and Jaap van Duin, for ordering materials for my experiment setup, for helping me with building my experiment setup, and repairing my measurement instruments when they were broken. They always helped me thinking about finding new solutions.

Furthermore, I would like to thank my college friends, Raoul and Gustav, for giving me advice, supporting me in the Laboratory, especially during the evenings and weekends when we were performing measurements at the same time.

Finally, I want to thank my parents, sister and especially Larissa Scholte. They supported me all the time and gave me the encouragement to finish my thesis. When I was stuck, they were able to provide me, direct and indirect, new insights in what I should do and they ensured that I do not think about my thesis when I do not have to. Finishing my thesis was not possible without them. Thank you.

Preface

This report titled 'Hydraulic load reduction as a function of depth in a filter layer consisting of logs' is submitted for the Degree of Master of Science in Hydraulic Engineering at the Delft University of Technology. The thesis project was commissioned by Deltares and Rijkswaterstaat, with the supervision of Arjan Sieben. The project was performed at the Delft University of Technology under the supervision of Wim Uijttewaal, Henk-Jan Verhagen and Jeremy Bricker at the Department of Hydraulic Engineering of the Faculty of Civil Engineering and Geosciences of Delft University of Technology.

Delft, July 2018
Roland Rubaij Bouman

Summary

The formation of scour holes is a vital thread of retaining the water infrastructure of rivers. Nowadays, protective filters are used to prevent washing away of the underlying material. Rijkswaterstaat started the program 'Stroomlijn', in which trees (logs) are cut from the floodplains and placed in a sheltered zone of the river to test whether this would increase the flora and fauna. After some years, the logs might be re-used as bottom protection. This kind of bottom protection is formed by placing multiple logs next to each other, which together form a log carpet, and placing multiple log carpets on top of each other. This is called a log filter.

Until now, no research has been carried out into the use of logs as bottom protection. The main function of a log filter is to reduce the hydraulic load so that the erosive capacity of the grains of the bottom will not be reached. Since a log filter has the same main function as a geometrically open filter, the question arises whether the hydraulic load reduction of a log filter could be described by the current theory of granular open filter.

The main objective of this research is to look whether logs could be used as bottom protection to prevent the formation of scour holes. Therefore, this research provides an insight of the hydraulic load reduction as a function of depth inside a log filter. Subsequently, the effect of the filter on the underlying soil is regarded. Thereafter, the results are compared with the theory of granular open filters and it is concluded whether the theory of granular open filter could also be used in case of a log filter.

In this research, the failure mechanism which concerns bed transport and winnowing is considered. This failure mechanism depends on the hydraulic load above and inside the filter layer. In granular open filter theory, the hydraulic load is defined as the pore flow velocity and turbulent kinetic energy inside the filter layer. The hydraulic load is caused by the influence of the energy slope and the influence of the flow over the filter structure. The formulas describing the pore flow velocity and turbulent kinetic energy by both influences are derived by Hoffmans (2012). The pore flow velocity and turbulent kinetic energy caused by the energy slope is always present, regardless of how thick the layer is. The influence of flow over the filter structure decreases exponentially and depends on the load damping length. The stability of a geometrically open filter also depends on the bed pressure fluctuations due to low-frequency vortices in the free flow above the filter. These low frequencies are able to lift the grains in the base layer. Klar (2005) showed that the shear stress decreases significantly with depth inside the filter. Therefore, the bed shear stress in open granular filter is negligible.

In order to provide the hydraulic load reduction of a filter consisting of logs, experiments have been conducted in a flume of The Fluid Mechanics Laboratory at the Delft University of Technology. A filter consisting of logs has been mimicked and tested. The hydraulic load, i.e. increasing the depth

average flow velocity and discharge, was increased until erosion occurred. During each increasing step, flow velocities above and inside the filter layer were measured.

From the experiments, it is concluded that at least two layers are needed in order to ensure a significant decrease of the pore flow velocity and turbulent kinetic energy. Adding more than two layers will not lead to further reduction of the pore velocity or turbulent kinetic energy. The pore flow and turbulent kinetic energy beneath layer 2 are dominantly caused due to the influence of the energy slope. Hence, the equation of Hoffmans (2012) describing the influence of the energy slope is appropriate in case of a log filter. However, the influence of the flow over the filter structure on the pore flow velocity and turbulent kinetic energy in a log filter does not decrease exponentially over depth. Therefore, we concluded that the formula of Hoffmans (2012) describing the exponential decay of the pore flow velocity and turbulent kinetic energy due to the influence of the flow over the filter construction could not be applied in a log filter.

In addition, we concluded that the flow in a log filter is very anisotropic. The flow characteristics differ in front, halfway and behind the log. In front of the log, stagnation is present, which leads to a vertical jet flow directed downwards. This flow causes erosion in front of the logs in the first layer. The erosion process in case of a log filter differs from granular open filters, which stated that erosion is predominantly caused by the hydraulic load, i.e. pore flow velocity and turbulent kinetic energy, in the filter and the bed pressure fluctuations due to low-frequency vortices.

We also concluded that at locations where the porosity is higher, erosion occurred at lower hydraulic load conditions, i.e. discharge and depth-averaged flow velocity. This indicates that the porosity is an important variable when logs are used as bottom protection.

This research gave an insight into the reduction of the pore flow velocity and turbulent kinetic energy over depth inside a filter layer consisting of logs. However, it is difficult to derive a physical formula which quantifies the decay of the pore flow velocity and turbulent kinetic energy over depth. In addition, the flow measurements were done in the middle and between two logs, whereas the flow in front of the log causes the erosion. For future research, it is essential to perform research in the flow properties of the anisotropic flow caused by the logs. Subsequently, it is recommended to carry out more research in the aspect ratio, porosity and geometry, since this research does not provide the influence of these variables.

Contents

List of Figures

List of Tables

List of symbols

Parameters which are important for this research

Symbol	Description	Unit
A_f	total surface filter layer	m^2
A_p	pore surface filter layer	m^2
C	Chézy coefficient	$m^{1/2}/s$
$\hat{C}$	drag factor	-
C_D	drag coefficient	-
D_f	filter layer thickness	-
F_D	drag force	N
F_F	flow force	N/m^3
F_G	gravitational force	N
F_L	lift force	N
F_W	gravity force	N/m^3
Fr	Froude number	-
L_d	damping length	m
L_f	length of the filter	m
R	hydraulic radius ($u_* D/\nu$)	m
Re	Reynolds number	-
Re_*	particle Reynolds number	-
Re_f	Reynolds filter number	-
S	sediment transport rate	m^3/s
T	parameter for the bed shear stress	-
U	depth-avergaed flow velocity	m/s
V_p	pore volume	m^3
V_t	total volume	m^3
c	sediment concentration	kg/m3
c_f	friction coefficient (between flow and wall)	-
d	1:layer thickness	m
	2:grain diameter	m
d_*	dimensionless parameter for the grain diameter	-
d_f	depth in filter layer	m
d_{xB}	grain diameter of the base material where x % of the grain mass has a lower diameter	m
d_{xF}	grain diameter of the filter material where x % of the grain mass has a lower diameter	m
d_x	grain diameter where x % of the grain mass has a lower diameter	m
d_{50}	median grain diameter	m

Symbol	Description	Unit
d_{n50}	median nominal diameter	m
g	acceleration of gravity	m/s^2
h	piezometric head	m
h_t	top piezometric level above the underlying layer	m;
h_u	under piezometric level above the underlying layer	m;
i	gradient material	-
i_b	bed slope	$^\circ$
i_c	critical gradient material	-
k	turbulent energy	[m^2/s^2]
$k_{f,dm}$	filter turbulence energy inside filter of deepest measurement	m^2/s^2
$k_{f,S}$	filter turbulence energy due to the mean energy slope (or gravity)	m^2/s^2
k_{log}	roughness of the logs	m
k_r	roughness height	m
k_{ref}	turbulence nergy at a reference level close to the transition between the free flow and the filter	m^2/s
n	1:porosity	-
	2:scale	-
n_l	number of layers	-
n_f	porosity filter layer	-
p	pressure	kPa
$p_{f,S}$	pressure due to the mean energy slope	kPa
p_m	maximum pressure fluctuation	kPa
$p_{m,f}$	maximum pressure fluctuation in the filter layer	kPa
$\bar{r}$	relative turbulence intensity	-
r_u	relative fluctuation intensity x-direction	-
r_v	relative fluctuation intensity y-direction	-
r_w	relative fluctuation intensity z-direction	-
r_{xz}	relative turbulent shear stress in x,z	-
s	relative density (ρ_s/ρ)	-
s_b	bedload transport	m^3/s
t	time step in experiment	-
u	velocity	m/s
$\bar{u}$	average velocity	m/s
u_*	shear velocity	m/s
u_{*c}	critical shear velocity	m/s
u_c	critical flow velocity	m/s
u_f	filter velocity	m/s
$u_{f,c}$	critical filter velocity	m/s
$u_{p,dm}$	lowest measured pore velocity	m/s
u_p	pore velocity	m/s
$u_{p,S}$	pore velocity cause by the mean energy slope	m/s
w_s	fall velocity	m/s
z_b	position of the bed in z-direction	m
Δ	relative density ($(\rho_s - \rho)/\rho$)	-
Δ_b	relative density of the bed	-
γ	safety coefficient due to irregularities of the soil	-
δ_v	viscous sublayer	m

Symbol	Description	Unit
κ	permeability	m/s
μ	ripple factor	-
ν	kinematic viscosity of water	m^2/s
ρ	water density	kg/m^3
ρ_s	sand density	kg/m^3
θ	bedding angle	$^\circ$
τ_0	bed shear stress at the transition between free flow and filter	N/m^2
τ_b	bed shear stress	N/m^2
$\tau_b^{'}$	the bottom (bed) shear stress related to the grains	N/m^2
$\tau_{b,c}$	critical bed shear stress	N/m^2
τ_f	shear stress in filter	N/m^2
ϕ_b	bed transport parameter	-
ϕ_s	angle of repose	$^\circ$
ψ	mobility parameter ($=\tau/\Delta gd$)	-
ψ_c	Shields (stability) parameter	-

Coordinate system

In this thesis a coordinate system is used in which:

- x-direction is a horizontal coordinate which is aligned with the main flow direction, i.e. longitudinal direction;
- y-direction is a horizontal coordinate which is perpendicular to the main flow direction, i.e. transverse direction;
- z-direction is a vertical coordinate which is positive upwards.

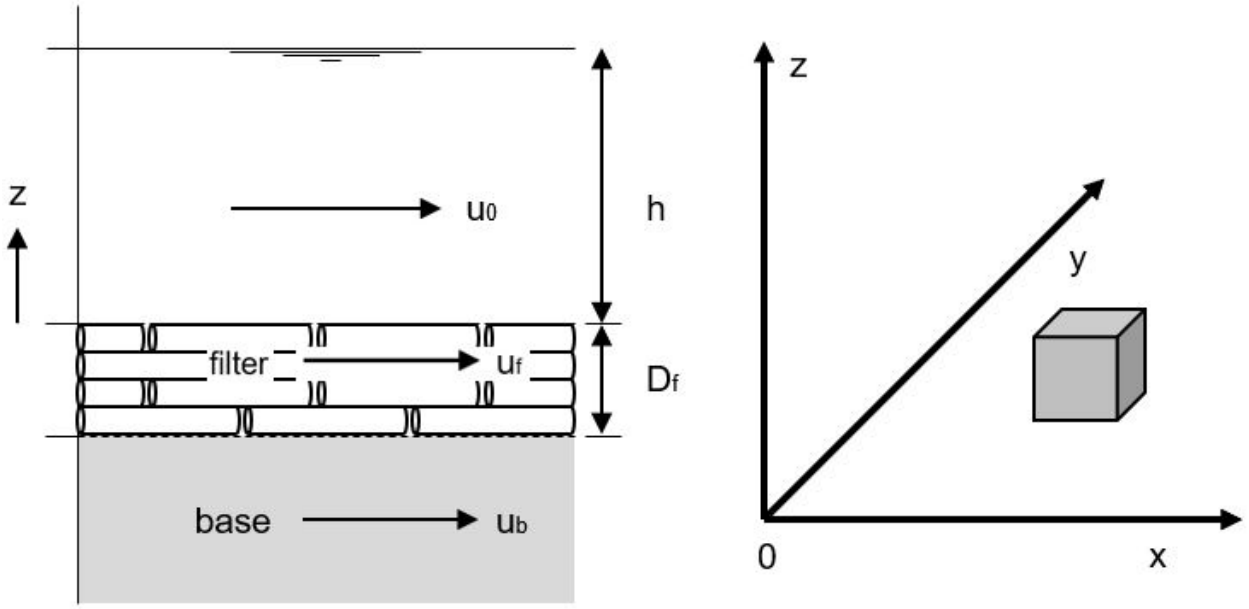

The location of the origin of the axis is:

- x = 0 is defined at the start from the filter layer in longitudinal direction;
- y = 0 is defined at the wall at the side of the flume in transverse direction;
- Two different locations were used for z = 0:
  - z = 0 is defined in the top of the filter;
  - z = 0 is defined in the bottom of the flume.

Frequently used indices

Indices		Description
u		velocity parameter in x direction
v		velocity parameter in y direction
w		velocity parameter in z direction
b	1:	base layer
	2:	base material
f	1:	filter layer
	2:	filter material
c		critical
p		pore
-		average
’		fluctuation
σ		standard deviation
μ		average

1 Introduction

1.1 Background information

In coastal and river engineering, scour holes are the vital threats of retaining the water infrastructure [Burns et al., 2011]. Scour holes form when the hydrodynamic bottom shear stress is larger than the critical shear stress of the sediment. If the scour holes grow and become too large, the water infrastructure could fail over time, i.e. the riverbank could collapse and groynes, quays, bridge piers and pipelines could be damaged [Harris et al., 2016]. Nowadays, protective filters are used to prevent washing away of the underlying material [Schiereck, 2016].

Rijkswaterstaat started the program 'Stroomlijn', in which trees (logs) are cut from the floodplains and are initially used to test whether the logs increase the flora and fauna when placing them in a sheltered zone of the river. After some years, the logs will be fully saturated and could be used for other purposes as well. Since the logs are cut at the flood planes nearby the erosion zones and these zones have to be regulated, the logs could be re-used as bottom protection. This kind of bottom protection is formed by placing multiple logs next to each other, which together form a log carpet, and placing multiple log carpets on top of each other. Multiple log carpets on top of each other are called a log filter.

Until now, no research has been carried out in the use of logs as bottom protection. The main function of a log filter is to reduce the hydraulic load so that the erosive capacity of the grains on the bottom will not be reached. The question arises whether a log filter behaves the same way as current solutions.

Currently, two main types of filters are used to stop the erosion process [Schiereck, 2016]:

1. Permeable geotextile which is made from artificial fibers. Geotextile prevents the erosion process by passing the water, but retaining the soil particles;

2. Granular filter which is made from natural rock. A granular filter prevents the erosion process by one or more layers of grains of varying diameter which reduce the hydraulic load.

A log filter cannot be compared with geotextile, since the main function differs: logs are not able to pass the water and retaining the soil particles. Logs are open structures. However, granular filters could be compared with a filter consisting of logs. Two types of granular filters exist [Schiereck, 2016]:

1. Geometrically closed filters, in which the grains of the base layer cannot pass through the pores of the grains in the filter layer;

2. Geometrically open filters, in which the grains of the base layer can pass the pores of the grains in the filter layer, but the main function is to reduce the hydraulic load such that the erosive capacity will not be reached.

The most commonly used granular filter is the geometrically closed filter, which has many design rules derived from Terzaghi. This is proven to be a sufficient technology to prevent bottom erosion [Schiereck, 2016]. Since the grains of the base layer cannot pass through the pores in the filter layer, a closed filter goes hand in hand with multiple filter layers. In general, logs differ in size and length. Since logs have a relatively large diameter, the rules by Terzaghi cannot be applied. Therefore, logs as bottom protection cannot be defined as a geometrically closed filter.

In contrast to geometrically closed filters, geometrically open filters are not constructed of multiple layers. In practice, these filters have the advantage that only one grading of filter material may be applied, depending on the loading, the thickness and gradation of the filter material. Since a log filter has the same main function as a geometrically open filter, the question arises whether the hydraulic load reduction of a log filter could be described by the current theory of granular open filters.

The last decades, research has been done in developing a formula for geometrically open filters [CUR, 2010]. Although none of the design equations are adopted in the field of hydraulic engineering, different models exist that describe the distribution of the hydraulic load inside a granular open filter [CUR, 2010].

1.2 Problem description

Until now, no research has been carried out on the use of logs as bottom protection. Models which describe the hydraulic load reduction as a function of depth are lacking. An elementary insight into the hydraulic load reduction of a log filter is needed in order to know whether this is a feasible alternative for bottom protection. Since this information is lacking, no relation could be made whether it is possible to describe the load reduction in a log filter by the current theory and models of granular open filters.

Generally, in a geometrically open filter, the hydraulic load reduces when going deeper inside the filter layer. Likewise, it is expected that the hydraulic load reduces over depth in the filter layer of a filter consisting of logs. How this declination would be is yet unknown.

1.3 Research objective

The main objective of this research is to look whether it is feasible to use logs as bottom protection to prevent the formation of scour holes. Therefore, this research provides an insight of the hydraulic load reduction as a function of depth in the filter layer which consist of multiple log carpets. Subsequently, the effect of the filter on the underlying soil will be regarded. Thereafter, the results will be compared with the theory of granular open filters and will be concluded whether the theory of granular open filter can also be used in case of logs as bottom protection. This will be done by executing scale experiments in a flume in the laboratory at the faculty of Civil Engineering, which reproduces a river. An insight into the hydraulic load above, inside and under the filter structure, consisting of log carpets, will be obtained. Moreover, the erosion process underneath the filter layer will be regarded.

The main research question is defined as follows:

How does the hydraulic load as a function of depth in the filter layer, consisting of logs, behave and what is the influence on the underlying soil?

With the following sub-questions:

1. What is the minimum required thickness, i.e. the number of layers, of the filter layer in order to ensure the stability of the base layer to prevent erosion of the underlying soil?
2. What type of erosion is a log filter inducing on the base layer?
3. What are the differences between the hydraulic load reduction in a log filter and a granular open filter?
4. Which parameters and variables are important for describing the load reduction?

2 Theoretical background

Since we are going to compare our results with the available theory of granular filters, this chapter provides the theory and design rules of granular filters. First, Section 2.1 presents the possible failure mechanisms of granular filters. Additionally, the hydraulic load caused by flow and the stability of elements in combination with winnowing, which cause the failure mechanism of bed transport, are discussed in Section 2.2 and 2.3. Thereafter, Section 2.4 provides the current theory about the reduction of the hydraulic load over depth in a granular open filter. Since this research makes use of a scale model, the theory about scale effects is regarded as well (Section 2.5). Finally, Section 2.6 provides a conclusion of the theoretical background and gives an overview of what should be regarded in order to provide an answer to the research questions.

2.1 Failure mechanisms

In this research, a two dimensional parallel flow, i.e. in x- and z- direction, over the filter layer is considered. In granular filters, three main failure mechanisms are possible (Figure 2.1) [van de Sande, 2013]:

1. Shear failure;
2. Combination of bed transport and winnowing;
3. Edge failure.

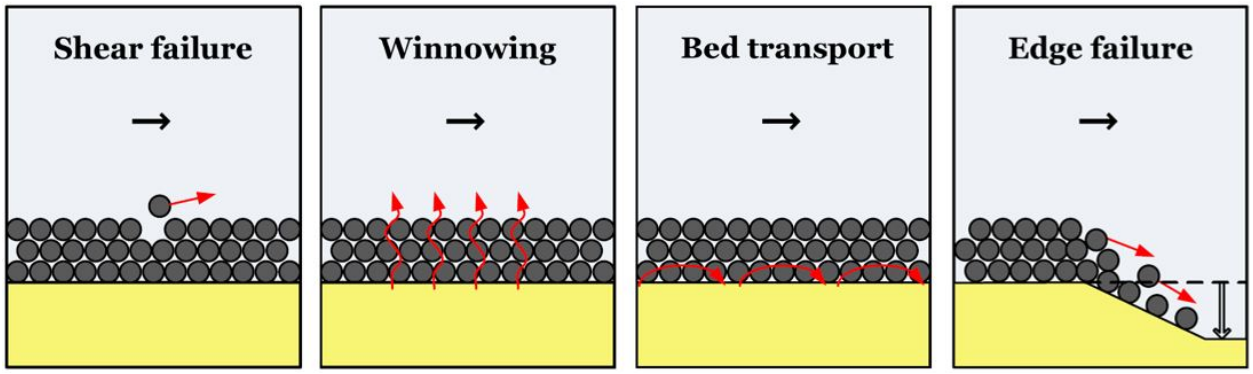

Figure 2.1: Failure mechanisms of granular open filter with parallel flow [van de Sande, 2013].

2.1.1 Shear failure

Shear failure is present when the acting force (shear stress) is higher than the resistance (critical shear stress) of the considered element. In that case, the element starts to move. At the TU Delft, two studies described the critical velocity of wooden logs [Haage and Çete, 2016] [van Leeuwen et al., 2016].

From these studies, it followed that logs which were placed aligned with the flow reached higher critical velocities than the logs which were placed perpendicular to the flow. Shear failure of the filter layer will not be considered in this research.

2.1.2 Combination of bed transport and winnowing

Bed transport occurs when the base layer starts to move due to shear failure. For that reason, the properties of the base layer should be regarded. The hydraulic load of the flow and the stability of sand grains are elaborated in Section 2.2 and Section 2.3, respectively. In general, the filter layer reduces the hydraulic load in such a way that the stability of the base layer is ensured. However, if the hydraulic load reduction is limited, the hydraulic forces might be larger than the resistant forces of the bed. In that case, bed transport will occur.

Winnowing describes the passage of grains of the underlying grains through the pores of the filter layer. This mechanism is only possible in a geometrically open filter. In geometrical closed filters, the filter is designed by the laws of Terzaghi: the grains of the underlying layer cannot pass through the pores of the filter layer. Winnowing occurs when the filter layer does not sufficiently reduce the hydraulic load to ensure the stability the grains of the base layer. In that case, the hydraulic forces are able to bring the grain particles into movement and will wash out the base layer through the pores of the filter layer.

The combination of bed transport and winnowing failure is considered in this research. When winnowing and bed transport are present, the reduction of hydraulic load in the filter is not sufficient enough in order to ensure the stability of the base layer. Both bed transport and winnowing depend on the hydraulic load and the stability (erosive capacity) of grains. The hydraulic load, caused by the flow, is elaborated in Section 2.2 and the stability is considered in Section 2.3. Finally, the hydraulic load reduction inside a filter layer is elaborated in Section 2.4.

2.1.3 Edge failure

Usually, downstream a granular bed protection, erosion occurs due to the limited sediment transport above the bed protection. If a significant amount of erosion occurs, the bed protection may slide into the scour hole and fails in its main function. Edge failure is not considered in this research.

2.2 Hydraulic load

This section considers the hydraulic load which is caused by the flow. It focuses on the turbulent properties of the flow and the shear stresses on the bed caused by the flow. The basics of current and fluid mechanics are not introduced in this chapter. This information is presented in Appendix A. Moreover, the following literature is recommended: "Vloeistofmechanica" by Battjes (2002) and "Principles of Sediment Transport in Rivers, Estuaries and Coastal Seas" by van Rijn (1993).

2.2.1 Turbulence

Turbulence is defined as irregular motions which deviate from the average fluid motion and can be described by laws of probability, see Figure 2.2. If the smallest scales of motion are in the order of a few millimetres, it is impossible to resolve the fluctuations on all scales in a model. Therefore, Reynolds decomposition is used, in which the velocity and pressure are written as an average part, given by a bar, and a fluctuation part, given by a ' [Schiereck, 2016]:

$$u = \bar{u} + u' \quad v = \bar{v} + v' \quad w = \bar{w} + w' \quad p = \bar{p} + p \tag{2.1}$$

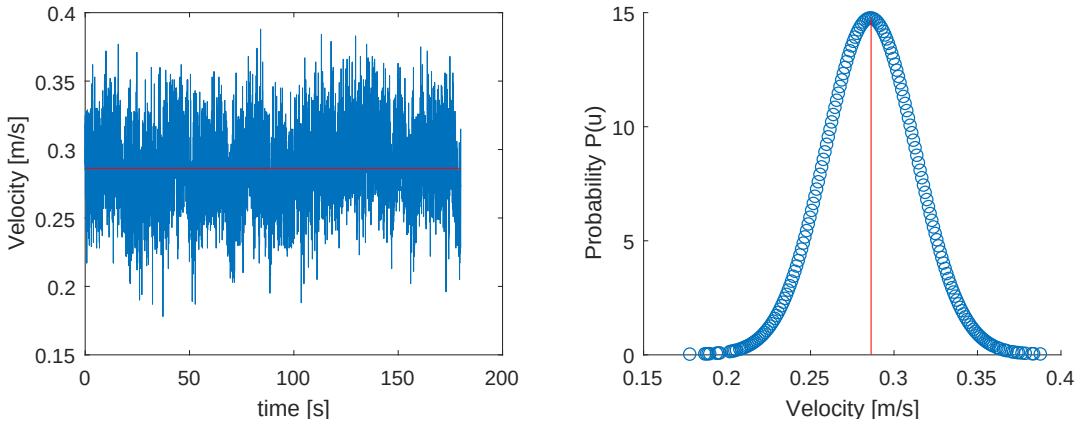

(a) Time series (b) Probability density function

Figure 2.2: Velocity measurement time series (a) and the probability density function of the time series (b), which follows a normal distribution, with the average velocity in red.

One way to express turbulence is:

$$k = \frac{1}{2}(\overline{u'^2} + \overline{v'^2} + \overline{w'^2}), \quad r_u = \frac{\sqrt{\overline{u'^2}}}{\overline{\overline{u}}}, \quad r_v = \frac{\sqrt{\overline{v'^2}}}{\overline{\overline{u}}}, \quad r_w = \frac{\sqrt{\overline{w'^2}}}{\overline{\overline{u}}} \tag{2.2}$$

in which:

u', v', w'	flow velocity of fluctuations in x,y and z-direction [m/s];
$\bar{u}, \bar{v}, \bar{w}$	average flow velocity in x, y and z-direction [m/s];
r_u, r_v, r_w	relative fluctuation intensities of u, v and w compared to the main flow component [-];
k	total kinetic energy in a turbulent flow [m^2/s^2].

Describing the flow by laws of probability, the fluctuation component of velocity is characterised by the variance:

$$Var_u = \sigma_u^2 = \overline{(u - \overline{u})^2} \tag{2.3}$$

The variance represents the kinetic energy in the turbulent fluctuation. The intensity, which is the square root of the variance, is called the intensity. With μ representing the average velocity, Equation 2.2 can be rewritten as follows:

$$k = \frac{1}{2}(Var_u + Var_v + Var_w), \quad r_u = \frac{\sigma_u}{\mu_u}, \quad r_v = \frac{\sigma_v}{\mu_v}, \quad r_w = \frac{\sigma_w}{\mu_w} \tag{2.4}$$

Klar (2005) assumed that the turbulence in the pores of granular filter is approximately uniform in all directions [Hoffmans, 2012]. In that case, the turbulent kinetic energy in the filter (k_f) is:

$$r_u = r_v = r_w \quad \Rightarrow \frac{\sqrt{\overline{u'^2}}}{\overline{\overline{u}}} = \frac{\sqrt{\overline{v'^2}}}{\overline{\overline{u}}} = \frac{\sqrt{\overline{w'^2}}}{\overline{\overline{u}}} \quad \Rightarrow \quad k_f = \frac{3}{2}\overline{u'^2} \tag{2.5}$$

The local relative turbulence intensity in the filter layer (r_f) is defined as [Hoffmans, 2012]:

$$r_f(z) = \frac{\sqrt{k_f(z)}}{\overline{u_p(z)}} \tag{2.6}$$

2.2.2 Shear stress

The equations that govern the evolution of a fluid are called the Navier-Stokes equations, see Appendix A.4. When using Reynolds decomposition in combination with the continuity equation the Reynolds averaged Navier-Stokes (RANS) are found, see Appendix A.5. In a two-(x,z) dimensional situation, the RANS (also called Reynolds) equations becomes as follows:

$$\underbrace{\rho(\frac{\partial \bar{u}}{\partial t} + \bar{u}\frac{\partial \bar{u}}{\partial x} + \bar{w}\frac{\partial \bar{u}}{\partial z})}_{\text{inertia}} = \underbrace{-\frac{\partial \bar{p}}{\partial x}}_{\text{pressure forces}} + \underbrace{\mu\frac{\partial^2 \bar{u}}{\partial z^2}}_{\text{viscous forces}} - \underbrace{\rho(\frac{\partial \overline{u'^2}}{\partial x} + \frac{\partial \overline{u'w'}}{\partial z})}_{\text{Reynolds stresses}} \tag{2.7}$$

mean values (inertia, pressure forces, viscous forces) | turbulent fluctuations (Reynolds stresses)

According to this procedure, the shear stress in a turbulent flow at height z in a steady uniform flow can be described as [van Rijn, 1993]:

$$\tau_z = \underbrace{\rho\nu\frac{du}{dz}}_{\tau_\nu} - \underbrace{\rho\overline{u'w'}}_{\tau_t} \tag{2.8}$$

In case of turbulent flow, i.e. $Re > 2000$ (Appendix A.1.2), the second part of this equation becomes dominant. The first part of this equation becomes dominant when the turbulent fluctuations, u' and w' respectively, are low. This occurs close to the bottom, see Figure 2.3. The part near the bottom is called the viscous sublayer (δ_v). On top of this layer, the logarithmic sublayer is present. More information about the logarithmic sublayer is given in Appendix A.2. In between the viscous and logarithmic sublayer, a transition sublayer is present [van Rijn, 1993], see Figure 2.4. In case of a rough bottom, e.g. the experiments in this research, the viscous part is not important and therefore:

$$\tau_z = -\rho\overline{u'w'} \tag{2.9}$$

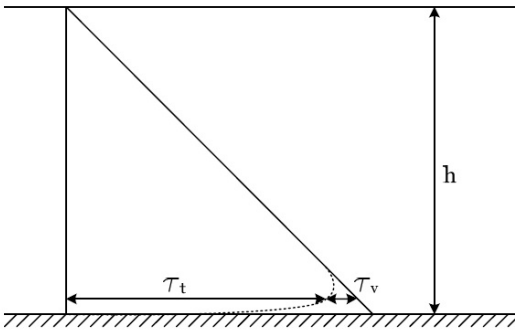

Figure 2.3: Shear stress over depth consisting of turbulent and viscous part [van Rijn, 1993].

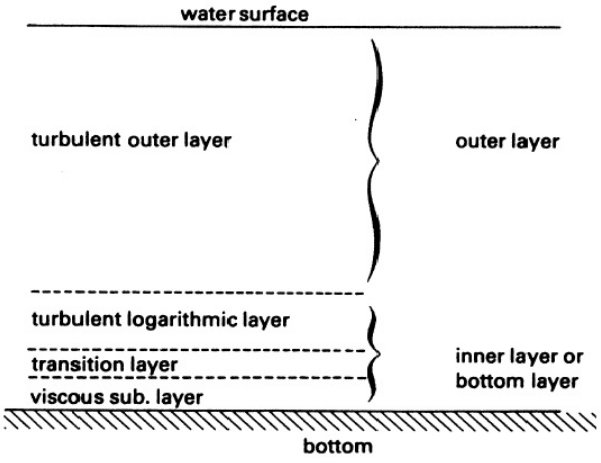

Figure 2.4: Boundary, transition and turbulent logarithmic layer [van Rijn, 1993].

In order to provide a relation between the resistance of the bed (bed shear stress) and the average flow velocity $\overline{\bar{u}}$, the following formula is used [Schiereck, 2016] (appendix A.2):

$$\tau_b = \rho g h i_b = c_f \rho \overline{\bar{u}}^2 = \rho u_*^2 \tag{2.10}$$

2.3 Stability

The stability of the grains depends on the grain characteristics, e.g. size, grain size distribution and density. This section describes the forces regarding the stability of a particle. Additionally, two methods which describe the stability of a particle or bed are given. In this research, only loose non-cohesive materials and parallel flow will be considered.

2.3.1 Threshold of motion

A situation in which water flows over a grain is depicted in Figure 2.5. Some forces are driving forces, i.e. drag and shear forces, and others are resisting forces, i.e weight. The driving forces are also called hydraulic forces.

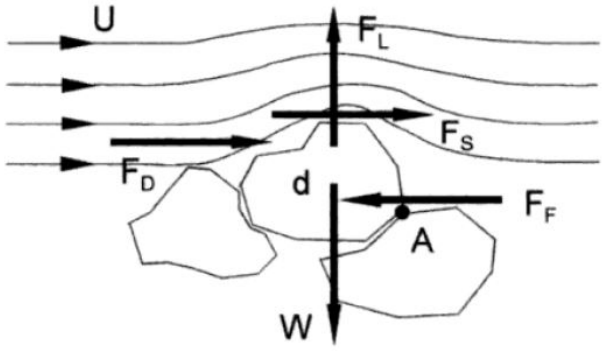

Figure 2.5: Forces on a grain, consist of a driving forces, i.e. drag, shear and lift force, and resisting forces i.e. gravitational force [Schiereck, 2016].

The various forces on the grain can be expressed as follows:

$$F_{\text{all}} \propto \rho u^2 d^2 = \begin{cases} \text{Drag force :} & F_D = \frac{1}{2} C_D \rho u^2 A_D \\ \text{Shear force :} & F_S = \frac{1}{2} C_F \rho u^2 A_S \\ \text{Lift force :} & F_L = \frac{1}{2} C_L \rho u^2 A_L \end{cases} \tag{2.11}$$

in which:

C_i	coefficients of force i [-];
A_i	exposed surface [m^2].

An equilibrium in moment, horizontal and vertical forces results in an equation which defines the critical velocity (u_c):

$$\begin{gathered} \sum H = 0 : F_{D,S} = F_F \\ \sum V = 0 : F_L = F_G \\ \sum M = 0 : F_{D,S} * O(d) = F_G * O(d) \\ \Downarrow \\ \rho u_c^2 d^2 \propto (\rho_s - \rho) g d^3 \\ \Downarrow \\ \rho u_c^2 \propto (\rho_s - \rho) g d \end{gathered} \tag{2.12}$$

in which u_c is the critical flow velocity when particles start to move.

2.3.2 Stability approaches

The stability of loose grains can be approached by means of two approaches: Izbash and Shields [Schiereck, 2016].

Izbash

The Izbash approach considers individual grains only and assumes a balance of all the forces acting on the grain. Following this assumption, Equation 2.12 can be written in a dimensionless relation between load and strength:

$$u_c^2 \propto (\frac{\rho_s - \rho}{\rho})gd = \Delta gd \tag{2.13}$$

From experiments Izbash expressed the critical velocity as follows [Schiereck, 2016]:

$$u_c = 1.2\sqrt{2\Delta gd} \quad \text{or} \quad \frac{u_c}{\sqrt{\Delta gd}} = 1.7 \quad \text{or} \quad \Delta d = 0.7\frac{u_c^2}{2g} \quad \text{with:} \quad \Delta = \frac{\rho_s - \rho}{\rho} \tag{2.14}$$

During his experiments, Izbash used relative big stones in shallow water to understand the stability of loose grains. However, the location of the acting forces and the diameter of the stone is not well defined. Therefore, the Izbash formula should only be used in case of non-uniform flow or in conditions in which the velocity does not depend on an equilibrium situation between flow and bed friction.

Shields

Shields considered the friction force caused by the water flow on the entire bed. Instead considering individual grains, he considered the average shear stress on the bed. The critical bed shear stress (τ_b) is defined as follows [Schiereck, 2016]:

$$\tau_{b,c} = \rho u_{*,c}^2 \tag{2.15}$$

In which u_* is the shear velocity parameter which cannot be measured. When the acting bottom shear stress is greater than the critical bottom shear stress, initiation of motion will occur.

Shields performed experiments on a flat bed and defined the critical bed shear stress with the Shields parameter (ψ_c) [Schiereck, 2016]:

$$\psi_c = \frac{\tau_{b,c}}{(\rho_s - \rho)gd_{50}} = \frac{u_{*c}^2}{\Delta gd_{50}} \tag{2.16}$$

Shields found that the Shields parameter is a weak function of the particle Reynolds number (Re_*). The particle Reynolds number expresses the hydraulic conditions near the bed ($Re_* = \frac{u_* d}{\nu}$). Shields produced a curve that relates the Shields parameter with the particle Reynolds number. However, the Shields curve is not practical since it needs an iteration of ψ_c and Re_*. Van Rijn expressed the critical shields parameter with the dimensionless particle number (D_*, see Appendix A.3). The Shields parameter related to the particle number is given in Figure 2.6.

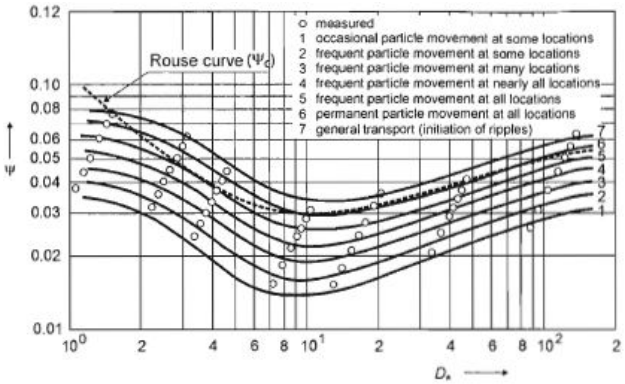

Figure 2.6: Shields diagram: the Shields parameter (ψ) related to to the particle number (D_*) [van Rijn, 1993].

2.4 Granular filters

This section focuses on the different types of granular filter structures: a geometrically open and geometrically closed filter. From this, it follows that a filter consisting of logs could only be compared with geometrically open filter. Currently, available theory which describes the flow conditions inside a geometrically open filter layer is shown. Therefore, the flow and shear stress distribution are elaborated. Also, the turbulent kinetic energy and damping coefficient is shown. At last, an insight of the current assumptions and consideration of current design equations of granular open filters are elaborated.

2.4.1 Type granular filter

The main function of a granular filter is to prevent erosion of the underlying material. Nowadays two types of granular filters can be distinguished, see Figure 2.7:

- Geometrically closed filters, in which the grains of the base layer cannot pass through the pores of the grains in the filter layer;
- Geometrically open filters, in which the grains of the base layer can pass through the pores of the grains in the filter layer, but the main function is to reduce the hydraulic load in such a way that underlying layer is stable.

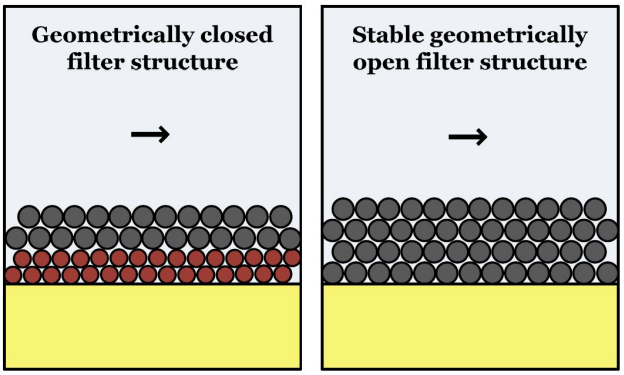

Figure 2.7: Two types of granular filters: a geometrically closed filter (left) and a geometrically open filter (right) [van de Sande, 2013].

The main characteristic of geometrically closed filters is that the grains of the base layer are not able to pass through the pores of the grain of the filter layer. The pore area of the filter layer is simply too small for the underlying material to pass. This is a relatively conservative design approach because no critical gradient is present between the two layers. As long as the upper filter is able to withstand the hydraulic load, the critical velocity or critical bed shear stress of the base layer does not play a role. In order to design a geometrically closed filter, Terzaghi derived three conditions which have to be ensured [Schiereck, 2016]:

- the stability between the filter layer and the base layer should be designed such that the larger grains of the base layer cannot penetrate through the pores of the smaller grains of the filter layer;
- the internal stability of both layers has to be ensured. The range of the grain diameters should be low enough to ensure that larger grains blocks of the smaller grains;
- the permeability between the filter layer and the base layer must be high enough to prevent pressure build-up.

The three conditions are given in Equation 2.17 in which d_x is the grain diameter where $x\%$ of the grain mass is finer. The filter and base layer are given as f and b respectively.

$$\text{Stability: } \frac{d_{15f}}{d_{85b}} < 5 \quad \text{Internal stability: } \frac{d_{60}}{d_{10}} < 10 \quad \text{Permeability: } \frac{d_{15f}}{d_{15b}} > 5 \tag{2.17}$$

The main characteristic of a geometrically open filter is that the grains of the base layer could pass through the pores of the filter. Furthermore, the hydraulic load is reduced in such a way that the base material will not start to move. In this case, the filter layer has to reduce the hydraulic load to make sure that the critical load, in which the grains of the base layer start to move, will not be exceeded. In other words: the baser layer of a geometrically open filter is stable when the critical gradient is always larger than the acting gradient in the structure.

Since logs have relatively large diameters, the rules by Terzaghi cannot be applied. Therefore, logs as bottom protection cannot be defined as a geometrically closed filter. However, it might be possible that a filter consisting of logs behaves the same way as granular geometrically open filters.

Two main directions of the water flow could be considered in a granular open filter: perpendicular and parallel flow. In case of bottom protection in rivers, only parallel flow is considered. This also holds for this research. In granular filters, the flow through porous media is called porous flows. The flow above a granular filter will induce a flow in the filter layer and may cause erosion at the underlying soil at the interface between the filter layer and the base layer. The hydraulic load has two important aspects: the pressure and the flow velocity [Schiereck, 2016]. This will be elaborated in the next paragraphs.

2.4.2 Porous flow

Porous flow in a granular filter could be laminar or turbulent, depending on the bed characteristics. Laminar flow goes hand in hand with a relative smooth bed, i.e. clay or sand. In that case, a linear relation between the pressure and velocity is present. In case of turbulent flow, which is caused by a bed consisting of coarse material, e.g. rock, the pressure and velocity are not linear and empirical

relations have to be used.

Considering a two-dimensional channel (x,z), the porous flow velocity in each pore could be determined theoretically by using the RANS equation (Equation 2.7). However, this is practically not feasible. Therefore, the pore velocity is obtained by means of the filter velocity using an averaging procedure [Schiereck, 2016]:

$$u_f = \frac{1}{A_f} \int \int_{A_p} u_p dA_p = n \cdot u_p \quad \text{with} \quad n = \frac{V_p}{V_t} \tag{2.18}$$

in which:

u_f	filter velocity [m/s];
A_f	total surface filter layer [m^2];
A_p	pore surface filter layer [m^2];
u_p	pore velocity [m/s];
n	porosity [-];
V_p	pore volume [m^3];
V_t	total volume [m^3].

Note that the filter velocity (u_f) is not the acting velocity. It describes the discharge through the entire filter layer divided by the filter area. The real acting velocity inside the filter is called the pore velocity (u_p).

The filter Reynolds number is a dimensionless number that is a measure of the type of flow through a porous medium. Three basic types are present: laminar $Re_f \leq 10$, transitional $10 < Re_f < 1000$ and turbulent $Re_f > 1000$. The filter Reynolds number is defined as [Hoffmans, 2012]:

$$Re_f = \frac{d_{f50} \overline{u_p}}{\nu} \tag{2.19}$$

in which:

d_{f50}	median diameter of filter [m];
$\overline{u_p}$	time-averaged local pore velocity [m/s].

The drag coefficient (C_D) of groundwater flow in filters is given in Figure 2.8. If the regarded flow has a filter Reynolds number (Re_f) lying in the range of 10^3 to 10^5, the drag coefficient for the coarse material is constant. This varies from 0.5 to 1.5, depending on the properties of the particles [Hoffmans, 2012].

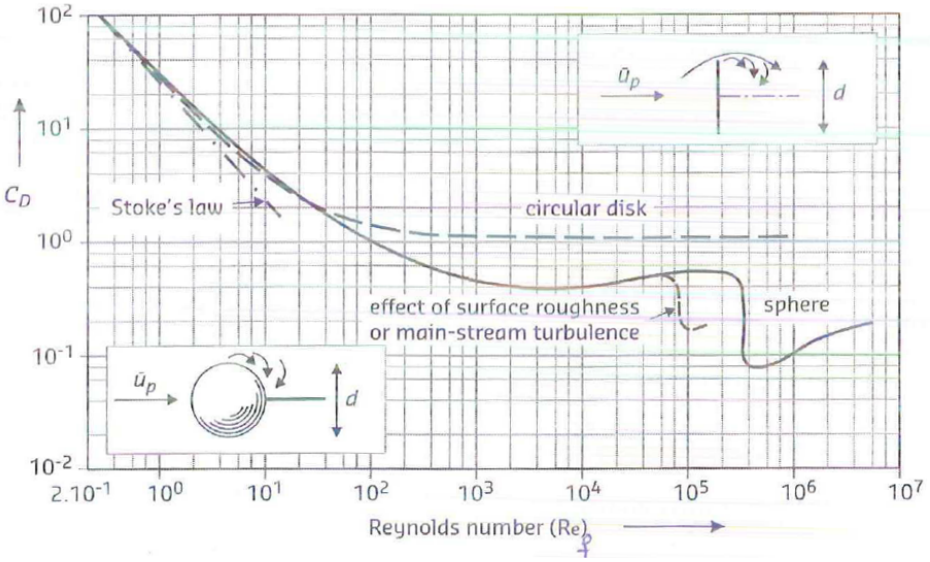

Figure 2.8: Drag coefficient versus filter Reynolds number [Hoffmans, 2012].

2.4.3 Flow and shear stress distribution

Normally, the flow and shear stress distribution in a two dimensional uniform parallel flow in a granular open filter acts like in Figure 2.9. The water flow in uniform flow decreases logarithm from the water surface towards the transition between the free flow and filter layer, while the shear stress linearly increases. A maximum shear stress is reached at the transition between the upper grains of the filter layer and the free flow since the flow velocity inside the filter layer is much lower than the flow velocity above the filter layer. Inside the filter layer, the flow velocity does not vary much over depth and therefore the shear stress may become zero. At the transition between the filter layer and the base layer, the shear stress increases again due to the difference in flow velocity in the filter layer and the base layer [Verheij et al., 2012].

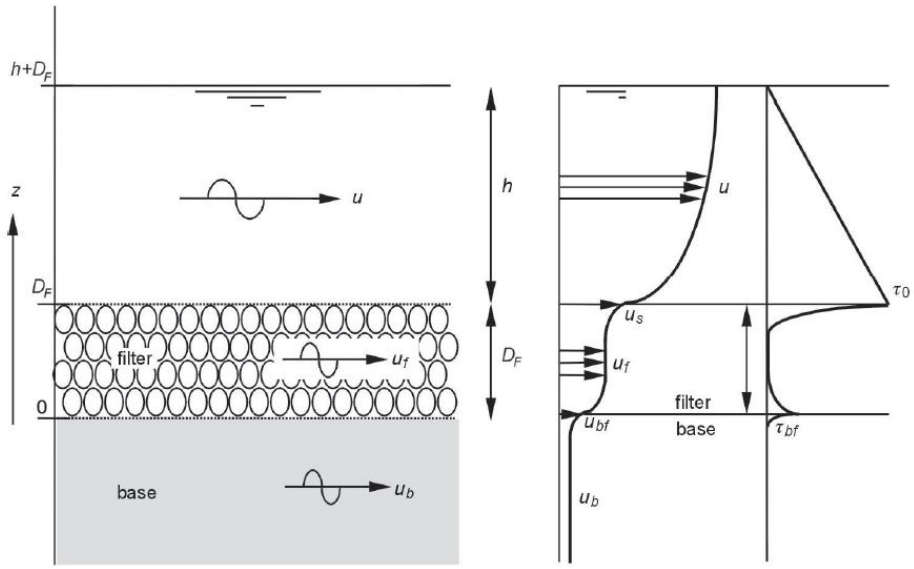

Figure 2.9: Flow and shear stress distribution over depth in case of a parallel flow in a granular open filter [Verheij et al., 2012].

The distribution of the pore flow velocity over depth inside the filter layer is showed in detail in Figure 2.10. The total pore flow velocity is caused by two factors [van Os, 1998]:

1. the influence of the energy slope ($\overline{u_{p,S}}$). When water flows in a river, a pressure gradient, i.e. an energy slope, over the bed is present which drives a flow over and through the filter. Regardless of how thick the filter layer is, the flow caused by the energy slope is constant and always present. In a uniform two-dimensional channel, the energy slope is equal to the gradient of the water level;
2. the influence of the flow over the structure. The pore velocity caused by this influence decreases exponentially over depth. Current theory relates this to the damping length (see Section 2.4.5).

Hoffmans described the decrease of the time-averaged horizontal pore velocity ($\overline{u_p}$) inside the filter layer by the assumption of a one-layer filter (no base layer) [Hoffmans, 2012]:

$$\overline{u_p}^2(z) = \underbrace{\overline{u_{p,S}}^2}_{1} + \underbrace{(\overline{u_p}^2(0) - \overline{u_{p,S}}^2)\exp(\frac{z}{L_d})}_{2} \quad \text{with} \tag{2.20}$$

$$L_d = \alpha_d d_{f15} \tag{2.21}$$

in which:

$\overline{u_{p,S}}$	time-averaged pore velocity caused by the mean energy slope [m/s];
L_d	the damping length [m], see Section 2.4.5;
α_d	damping coefficient [-], see Section 2.4.5.

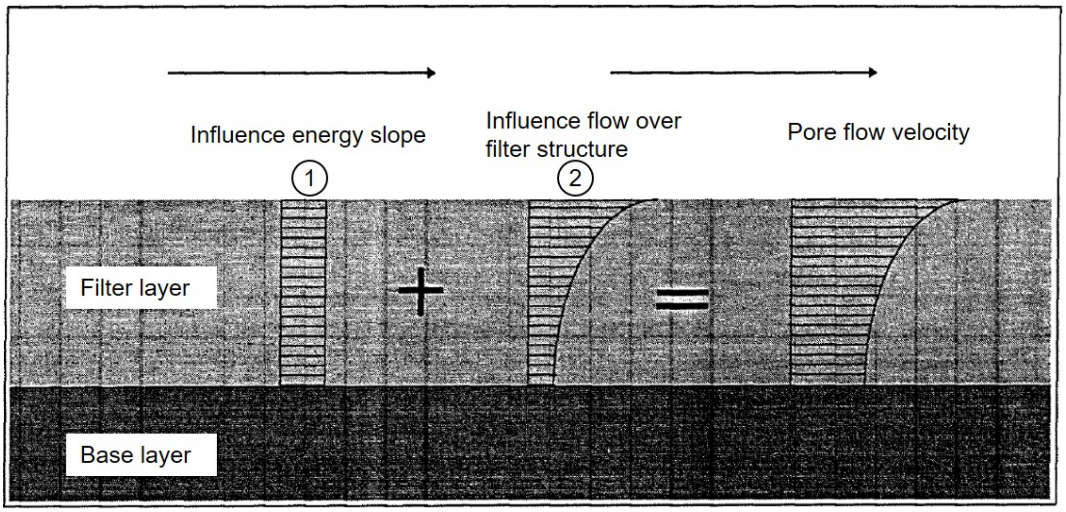

Figure 2.10: In granular open filter the total pore flow velocity depends on the mean energy slope (1) and the flow velocity above the filter (2) [van Os, 1998].

The pathway for the pore flow velocity, caused by the energy slope, is equal at each depth. The pore flow velocity caused by the energy slope is derived by Hoffmans (2012) as [Hoffmans, 2012]:

$$\overline{u_{p,S}} = \sqrt{2gd_{f15}S_e/C_D} \tag{2.22}$$

in which:

d_{f15}	the diameter of the filter in which 15 percent is finer. Since the logs have the same diameter [m];
S_e	the mean energy slope, which is equal to the gradient (i) of the water level [-];
C_D	drag coefficient [-].

Hoffmans also derived a formula which describes the decrease of the shear stress (τ_f) in a two-layered filter (filter and base layer) [Hoffmans, 2012]:

$$\tau_f(z) \approx \tau_0 \exp\left(\frac{z}{L_d}\right) + \tau_{b,f} \exp\left(-\frac{|z + D_f|}{L_d}\right) \tag{2.23}$$

in which:

τ_0	shear stress at the transition between free flow and filter [N/m^2];
$\tau_{b,f}$	bed shear stress at the transition between the filter layer and the base layer [N/m^2];
D_f	filter layer thickness [m].

Klar (2005) showed that the shear stress decreases significantly with depth. Hence, in granular open filters, the shear stress is negligible inside the filter layer [Hoffmans, 2012] [Klar, 2005].

2.4.4 Turbulent kinetic energy distribution

Based on the experiments of Klar (2005), the decrease of the local turbulent kinetic energy in the filter (k_f) over depth relative to the friction velocity is showed in Figure 2.11 [Hoffmans, 2012]. This figure shows that the turbulent kinetic energy becomes constant at approximately 5 to 6 times the average diameter of the grains inside the filter layer.

The total turbulent kinetic energy in the filter layer is caused by the same two factors as the pore flow velocity (Section 4.3.1: the influence of the energy slope and the influence of the flow over the filter structure, see Figure 2.12 [van de Sande et al., 2014]. The influence of the energy slope is always present, regardless of how thick the filter layer is. The damping of the turbulent kinetic energy caused by the flow over the filter structure decreases exponentially over depth.

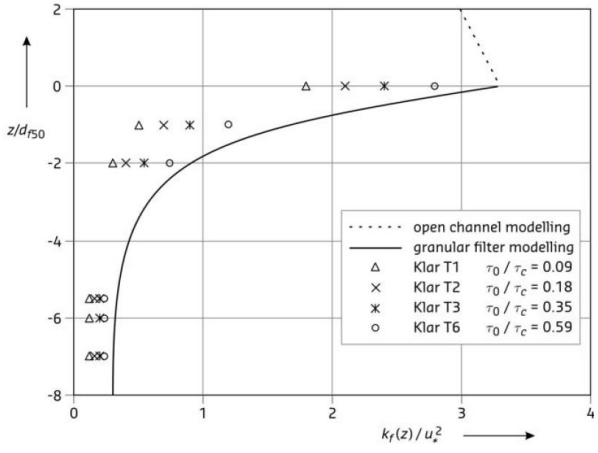

Figure 2.11: Experimental data of Klar which shows the decrease of the filter turbulence over depth [Hoffmans, 2012].

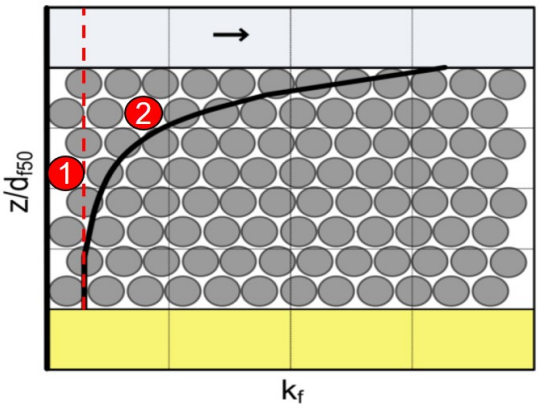

Figure 2.12: The turbulent kinetic energy depends on the influence of the energy slope (1) and the flow over the filter structure (2).

Based on Klar's uniform flow tests, Hoffmans (2012) derived a formula which describes the local turbulence energy by an exponential function [Hoffmans, 2012] [CUR, 2010]:

$$k_f(z) = \underbrace{k_{f,S}}_{1} + \underbrace{(k_f(0) - k_{f,S}) \exp\left(\frac{z}{L_d}\right)}_{2} \tag{2.24}$$

in which:

$k_{f,S}$	the turbulence energy due to the mean energy slope [m^2/s^2];
α_{ref}	a coefficient [-];
L_d	the damping length [m].

For a filter Reynolds number (Re_f) ranging from 10^3 to 10^5, the turbulent kinetic energy caused by the energy slope is derived by Hoffmans (2012) [Hoffmans, 2012]:

$$k_{f,S} = \frac{2 g r_f^2 S_e d_{f15}}{C_D} \tag{2.25}$$

The local relative turbulence intensity in the filter layer (r_f) and relative turbulence intensity ($r_{f,0}$) averaged over the filter thickness are defined as [Hoffmans, 2012]:

$$r_f(z) = \frac{\sqrt{k_f(z)}}{\overline{u_p}(z)} \tag{2.26}$$

$$r_{f,0} = \sqrt{k_{f,0}}/u_f \tag{2.27}$$

Hoffmans (2012) described that the local relative turbulent intensity inside the filter layer is constant over depth when the the filter Reynolds number (Re_f) ranges from 10^3 to 10^5 [Hoffmans, 2012]:

$$\overline{u_p}^2(z) = \frac{k(z)}{r_f^2} \quad \Rightarrow \quad r_f = \frac{\sqrt{k(z)}}{\overline{u_p}} \tag{2.28}$$

The derivation of the turbulent kinetic energy caused by the energy slope and the (local) relative turbulence intensity can be found in the book "The Influence of Turbulence on Soil Erosion" by Hoffmans (2012).

2.4.5 Damping coefficient and damping length

The damping of the pore flow velocity and turbulent kinetic energy depends on the damping coefficient α_d [Hoffmans, 2012]:

$$\alpha_d = \sqrt{\alpha_v / C_D} \tag{2.29}$$

in which α_v is a constant [-]. Hoffmans derived this parameter with the assumption that the filter Reynolds number (Re_f) ranges from 10^3 to 10^5 in which the drag coefficient is constant (see Figure 2.8):

$$\alpha_v = \frac{4}{C_D} \left(\frac{r_f^2}{\chi_k}\right)^2 \tag{2.30}$$

in which χ_k is the turbulence parameter. In a hydraulic rough regime ($k^+ > 70$) $\chi_k = 3.3$. In the viscous sub layer ($k^+ < 5$) χ_k reach values up to 5.6 [Hoffmans, 2012]. Combining Equation 2.29 and Equation 2.30 results in:

$$\alpha_d = \frac{2r_f^2}{C_D \chi_k} \tag{2.31}$$

In the experiments of Klar, r_f is about 1, resulting in very high relative turbulence intensities in the filter layer [Hoffmans, 2012]. Hoffmans proposed to use a damping coefficient (α_d) of 1.5.

2.4.6 Dynamic bed-pressure fluctuation

Erosion of the bed layer does not only depends on the hydraulic load due to the flow velocity, but also on local bed-pressure fluctuations over time caused by rotating eddies. These vortices are generated close to the bed in an open channel flow and generated by the flow through the filter layer. In granular filters, the water flows through open spaces and when the flow reattaches, small mixing layers occur which generate turbulence and high frequently flow fluctuations. These high frequently pressure fluctuations are able to lift the upper grains of the base layer, but the period is too short to transport the grains vertical towards the main flow. However, the low frequent flow fluctuations caused by turbulence vortexes in the flow above the filter layer, are able to lift the grains in the base layer. Due to the dynamic bed-pressures, the bed particles under the filter layer can be lifted and transported by the mean flow, i.e. during a sweep in which the local lift force becomes greater than the weight [Hoffmans, 2012].

Vortices can cause stress levels which are 10 to 20 times higher than the average stress level, but they only exist limited time. The largest eddies at macro and micro scale (defined by wave number ($k_w = 2\pi f/\overline{\overline{u}}$)) contribute more to the transport than the smallest eddies considered at Kolmogorov microscales, since these eddies contain more energy [Hoffmans, 2012]. When the length scale of the eddy is smaller than the particle size ($L < d$), the energy of the eddy is simply too low to move the particles.

For Fr < 0.5 and Fr > 2 the fluctuating pressure, i.e. standard deviation, on the bed is found to be:

$$\sigma_p \approx 3\tau_b \tag{2.32}$$

The maximum pressure fluctuations (p_m) could reach values up to 6 times the fluctuation pressure. With these estimates, the maximum pressure can be defined as follows:

$$p_m = \alpha_\tau \tau_b \quad \text{with} \quad \alpha_\tau \approx 18$$

At the transition from sub- to super-critical flow σ_p/τ_b reaches an evident maximum. Hence, α_τ has no universal value. Combining Equation 2.33, A.25 and 2.15, results in:

$$p_m = \alpha_\tau \alpha_0^{-2} \rho(\overline{\overline{r}} * \overline{\overline{u}}) \tag{2.33}$$

$$p_m = 12.6\rho(\overline{\overline{r}} * \overline{\overline{u}}) \tag{2.34}$$

The decrease of maximum pressure fluctuation ($p_{m,f}$) in the filter layer is derived by Hoffmans as [Hoffmans, 2012]:

$$p_{m,f}(z) = p_{f,S} + (p_m - p_{f,S}) \exp\left(\frac{z}{L_d}\right) \tag{2.35}$$

in which $p_{f,S}$ is the pressure due to the mean energy slope and is proportional to $k_{f,s}$ [kPa].

Bezuijen and Köhler (1996) derived a similar equation for defining the decrease of the pressure fluctuation [Bezuijen and Köhler, 1996]:

$$p_{m,f}(z) = p_{f,S} + (p_m - p_{f,S}) \exp\left(\frac{z\sqrt{\pi}}{L_{es}}\right) \quad \text{with} \quad L_{es} = \sqrt{c_v T_p} \tag{2.36}$$

in which c_v is the consolidation coefficient ($=k/(\rho g n \beta')$ [m^2/s] which is usually 10^{-3} m^2/s, β' is the compressibility of the pore water [1/Pa]. T_p is the pressure period. For uniform and turbulent flow conditions, T_p varies from 0.1 s to 1 s. This period defines the macro scale eddies [Hoffmans, 2012]. Combining Equation 2.35 and 2.36 gives:

$$L_d = \frac{L_{es}}{\sqrt{\pi}} = \sqrt{\frac{c_v T_p}{\pi}} \tag{2.37}$$

2.4.7 Design equations

In the past, multiple design equations for granular open filters were made. An optimal design is based on simultaneous erosion of the base and filter material [van de Sande et al., 2014]. This means that the failure mechanisms shear failure and winnowing occur at the same hydraulic load conditions (see Section 2.1). Most of the current design equations are based on this principle of optimal design.

In Appendix A.9 the current open filter design equations are elaborated. In this paragraph, a concise overview of all design equations is given in Table 2.1. All design equations are based on the relation between the properties of the filter and base material. The hydraulic load is not directly taken into account. At first, the hydraulic load on top of the filter layer is determined. The size of the grains of the filter layer is designed in such a way that the resistance forces are greater than the hydraulic forces (by means of Shields). Thereafter, the thickness of the filter layer is determined by using one of the equations.

Table 2.1: Current design equation for geometrically open filters.

Name	Formula	Layer thickness
Bakker-Konter [a]	$\frac{1}{d_{15f}} = \frac{C_0 e^2}{2.20} \frac{d_{50f}}{d_{50b} R} \frac{\psi_{c,f}}{\psi_{c,b}} \frac{\Delta_f}{\Delta_b}$	$\frac{1}{d_{15f}}$
Wörman [a]	$\frac{D_f}{d_{50f}} = 0.16 \frac{n_f}{1-n_f} \frac{d_{85f}}{d_{85b}} \frac{\Delta_f}{\Delta_b}$	$\frac{D_f}{d_{50f}}$
Hoffmans [b]	$\frac{D_f}{d_{15f}} = \alpha_d \ln\left(\frac{d_{50f}}{d_{50B}} \frac{\Delta_f}{\Delta_b} \frac{\Psi_{c,f}}{\Psi_{c,b}} \frac{1-\gamma V_f}{1-\gamma V_b}\right)$	$\frac{D_f}{d_{15f}}$
Van de Sande [c]	$\frac{D_f}{d_{50f}} = \alpha_d \ln\left(\frac{d_{50f}}{d_{50b}} \frac{\Delta_f}{\Delta_b} \frac{\Psi_{c,f}}{\Psi_{c,b}} \frac{1-\gamma V_f}{1-\gamma V_b}\right)$	$\frac{D_f}{d_{50f}}$

[a] [CUR, 2010]
[b] [Hoffmans, 2012]
[c] [van de Sande et al., 2014]

The Bakker-Konter formula is less suitable for the design of open filter since the formula does not take the filter thickness as a parameter into account. The main difference between the design formula of Hoffmans and Wörman is the relation between the layer thickness and the material properties. Wörman described this as a linear relationship, whereas Hoffmans described this as a logarithmic relationship, see Figure 2.13. Hoffmans formula is a theoretical equation. Van de

Sande validated this equation and concluded that this equation could be used for the design of a granular open filter. However, he also showed that two adjustments of the formula would lead to better representative outcomes [van de Sande et al., 2014].

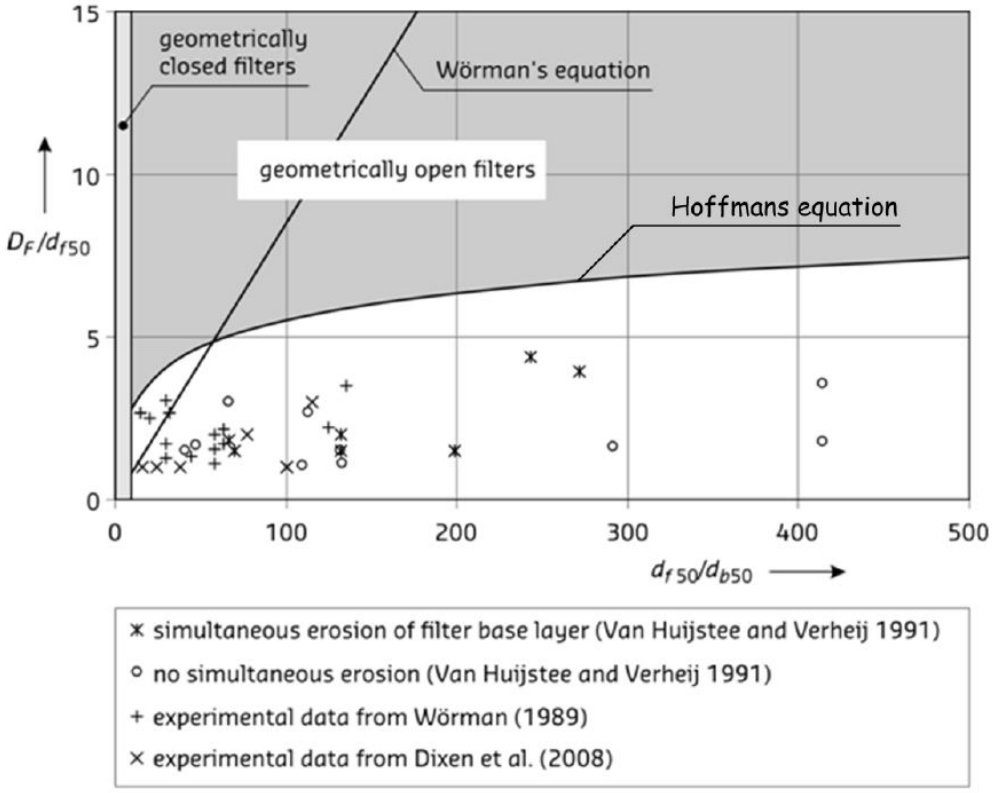

Figure 2.13: The relative filter thickness versus the relative size of the filter grains of all equations. The relation is linear in the equation of Wörman and logarithmic in the equation of Hoffmans [Hoffmans, 2012].

2.5 Scale effects

The main purpose of a scale model is to achieve a complete similitude of all force ratios as the prototype. The forces which are present during open water flow are given in Equation 2.38.

$$\text{Acting forces} = \begin{cases} \hat{F}_i = & \text{mass} \cdot \text{acceleration} = (\rho L^3 (V^2/L) = \rho L^2 V^2 \\ \hat{F}_g = & \text{mass} \cdot \text{gravitational acceleration} = \rho L^3 g \\ \hat{F}_\mu = & \text{viscosity} \cdot \frac{\text{velocity}}{\text{distance}} \cdot \text{area} = \mu (V/L) L^2 = \mu V L \\ \hat{F}_\sigma = & \text{unit surface tension} \cdot \text{length} = \sigma L \\ \hat{F}_e = & \text{modulus of elasticity} \cdot \text{area} = E L^2 \\ \hat{F}_{pr} = & \text{unit pressure} \cdot \text{area} = \rho L^2 \end{cases} \tag{2.38}$$

Similar ratios for all force ratios is impossible and a discrimination has to be made which ratios are crucial for the physical model. The scale (n) is defined as the ratio between the prototype value and the model value [Vries, 1982]:

$$n_y = \frac{y_p}{y_m} \tag{2.39}$$

in which:

n_y	scale factor [-];
y_p	quantity prototype;
y_m	quantity model.

Some forces become negligible in the prototype, but could have an influence on the model. In that case, the scale model will not have the same results as the prototype. This phenomenon is called a scale effect, e.g. when the surface tension and surface roughness have negligible consequences in the prototype, but have large influences in the model.

The Froude number (Fr) and Reynolds number (Re) are the two most important dimensionless numbers for describing the hydrodynamics. If we scale both dimensionless numbers, we get:

$$Fr = \sqrt{\frac{\text{inertial force}}{\text{gravity force}}} = \sqrt{\frac{\rho L^2 V^2}{\rho L^3 g}} = \frac{v}{\sqrt{gL}} \tag{2.40}$$

$$n_{Fr} = 1 \quad \Rightarrow \quad \frac{n_v}{\sqrt{n_g n_L}} = 1 \quad \Rightarrow \quad n_v = \sqrt{n_g n_L} \quad \Rightarrow n_v = \sqrt{n_L} \tag{2.41}$$

$$Re = \frac{\text{inertial force}}{\text{viscous force}} = \frac{\rho L^2 v^2}{\mu v L} = \frac{\rho L v}{\mu} = \frac{L v}{\nu} \tag{2.42}$$

$$n_{Re} = 1 \quad \Rightarrow \quad \frac{n_L n_V}{n_\nu} = 1 \quad \Rightarrow \quad n_\nu = n_L n_v \tag{2.43}$$

In a free surface flow, the gravity force predominates. Therefore, most hydraulic models are designed by the Froude criterion. However, the scale effects on the Reynolds criterion should be as low as possible, i.e. when the viscous effects deviate, too much scale effects occur and the model will not be representative for the prototype. For harbour models, a minimal Reynolds number of $1 \cdot 10^4$ is allowed to diminish the viscous effects of the Reynolds criterion. For pores flow in a breakwater, at least a Reynolds number of $3 \cdot 10^4$ is required to neglect the Reynolds criterion scale effects [Hughes, 1993].

In order to define the moment of erosion, a similitude of the sediment transport has to be ensured. This can be done by taking the scale of the mobility parameter Shields (Section 2.3) and the Reynolds particle number equal to one:

$$\psi_c = \frac{\rho_w u_{*,c}^2}{(\rho_s - \rho_w) g d_{50}} \quad \Rightarrow \quad n_{\psi_c} = \frac{n_i n_h}{n_{\rho_s - \rho_w} n_d} = 1 \quad \Rightarrow \quad n_{\psi_c} = \frac{n_{c_f} n_{\overline{u}}^2}{n_{\rho_s - \rho_w} n_{d_{50}}} \tag{2.44}$$

$$Re_* = \frac{u_* d}{\nu} \quad \Rightarrow \quad n_{Re_*} = n_{u_*} n_d = n_\tau^{\frac{1}{2}} n_d = n_i^{\frac{1}{2}} n_h^{\frac{1}{2}} n_d = 1 \tag{2.45}$$

2.6 Conclusion theoretical background

In general, three different type of failure mechanisms are present in granular filters: shear failure, a combination of bed transport and winnowing, and edge failure, see Section 2.1. In this research, only the failure mechanism which concerns the combination of bed transport and winnowing is considered. Since logs have relatively large diameters, the rules by Terzaghi cannot be applied. Therefore, logs as bottom protection cannot be defined as a geometrically closed filter. However, it might be possible that a log filter behaves the same way as granular geometrically open filters,

see Section 2.4.1.

The failure mechanism considering bed transport and winnowing depends on the hydraulic load above and inside the filter layer. The pore flow velocity and turbulent kinetic energy inside the filter layer are present due to two influences (see Section 2.4.3 and 2.4.4):

1. the influence of the energy slope, which constant over depth;
2. the flow over the filter construction, which decreases logarithmically over depth.

Additionally, the grains of the base layer could also be transported by the dynamic bed-pressure fluctuations caused by low-frequency vortices in the free flow. Under pressure, these eddies are able to lift up the grains of the base layer, which then can be transported by the mean flow, see Section 2.4.6.

In this research, we consider a log filter. We must question ourselves whether the same failure mechanisms are present in case of a log filter. In order to provide an answer to the research questions, we should be able to (see Figure 2.14):

- provide an insight on how the pore flow velocity and turbulent kinetic energy decreases over depth inside the filter layer;
- provide an insight into how large the eddies in the filter layer are and whether the eddies are able to lift the grains of the base layer;
- provide an insight whether the same failure mechanisms are present in case of logs.

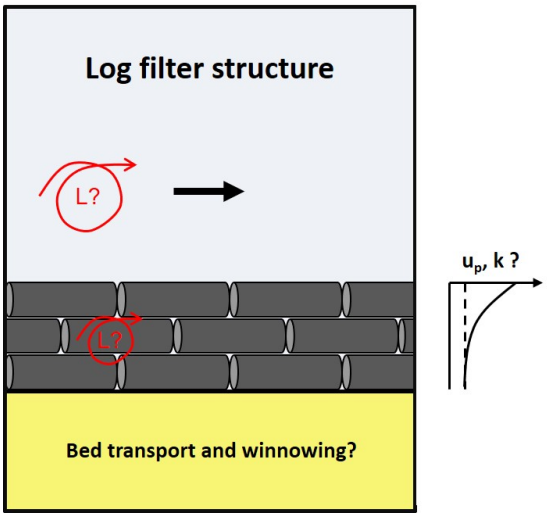

Figure 2.14: In order to answer whether logs could be used as bottom protection, the following processes should be considered: the reduction of the pore flow velocity and turbulent kinetic energy over depth, and the vortices inside the filter layer. Additionally, the way how the structure fails should be taken into account as well.

3 Experimental set-up

A physical scale model was used to provide an insight of the hydraulic load reduction in a log filter. The scale model has to show when and how the filter becomes unstable, i.e. when failing mechanisms such as winnowing and bed load transport occurs.

In this chapter, the experimental set-up, equipment and the assumptions for the research are elaborated. The experiments were done at the Fluid Mechanics Laboratory at the Delft University of Technology.

The prototype river which is modelled is a river in the Netherlands, i.e. the Maas. In this river, the water level is approximately 2 m and depth-averaged flow velocities up to 2 m/s could be reached. The average grain size of the sand on the bottom is 300 µm. In general, the Dutch rivers are in a hydraulic rough regime. If we assume the roughness height to be the average of old wood, $k_r = 1.5 \cdot 10^{-3}$ (Table A.1), the theoretical prototype Chezy value becomes 57.8 $m^{1/2}/s$. See Appendix A.2 for more information about the determination of the Chezy value.

3.1 General

3.1.1 Overview

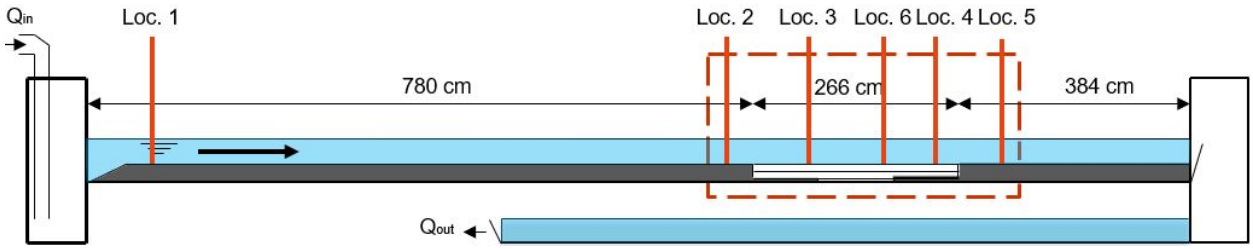

Figure 3.1: Side view of the flume.

Figure 3.1 shows a sketch of the structure in the flume. The flume was approximately 14 m long, 0.4 m wide and 0.4 m high. The maximum discharge was approximately 100 l/s and at the end of the flume, a weir was present. Both discharge and height of the weir could be changed manually. Beneath the main flume, a return flume was present which consisted of a Rehbock weir with a height of 0.25 m. The discharge in the flume was determined by means of this Rehbock weir.

A pump generated the amount of water in the flume. The length upstream the considered test area was 7.8 m in order to obtain uniform flow, see Section A.2. Due to the limited length of the flume, the minimum length was approximately 30 times the maximum water depth in the flume.

Downstream this minimum required length the test section was present, indicated by the red square. When the water passed the Rehbock weir in the return flume it flowed into a large storage basin.

3.1.2 Test section

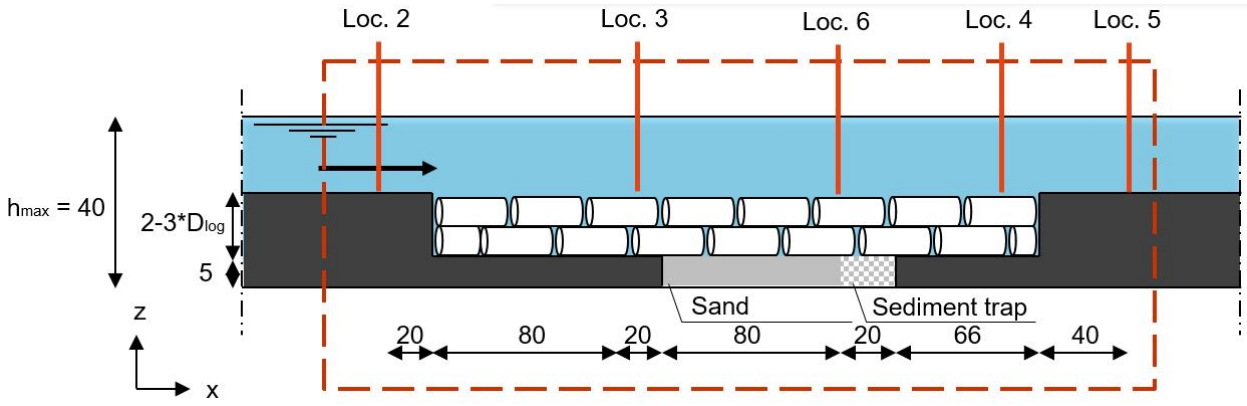

Figure 3.2: Side view of the test section in cm.

Figure 3.2 shows a sketch of the test section inside the main flume. The bed height was variable, depending on the thickness of the filter layer. Upstream the measurement area, it had to be ensured that the water flow penetrated through the entire thickness of the filter layer. For that reason, a required length of 80 cm was used. During the experiments, two types of measurements were executed: velocity measurements and the erosion measurements which will be further elaborated in Section 3.4.2 and 3.4.2, respectively.

The velocity measurements were done directly downstream from the point where the water flow has penetrated over the entire thickness of the filter layer, at location 3. The erosion measurements were performed downstream the velocity measurements by means of a sediment trap. The sediment trap is 5 cm high and 80 cm long. The eroded sediment was caught in the sediment trap.

3.2 Material characteristics

3.2.1 Base layer

For the erosion measurements sand was used. The use of sand is difficult, since sand particles lower than the 100 μm result in cohesive forces between the particles [Sutherland and Soulsby, 2010]. The used sediment class is AF100 and the grain diameter was determined by means of the average of five grading curves. The average grading curve can be found in Appendix B. The density of sand is 2650 kg/m^3. The sediment characteristics are shown in Table 3.1. The table shows the critical friction velocity and critical flow velocity.

Table 3.1: Sediment characteristics of the base layer.

Sand type	d_{10} [μm]	d_{50} [μm]	d_{90} [μm]	D_* [-]	ψ_c [-]	$u_{*,c}$ [m/s]	u_c [m/s]
AF100	108	140	172	2.93	0.025 - 0.082	0.0075 - 0.0136	0.14 - 0.25

3.2.2 Filter layer

Using real saturated wood as logs was not feasible due to the lack of time to let the wood become fully saturated, and the use of tropical wood would lead to high expenses. Therefore, in order to mimic wooden logs, PVC tubes were used which were 33 cm long and had a diameter of 3.2 cm. These logs were filled with sand and thereafter closed by PVC-caps at both sides of the tube, see Figure 3.3.

In the view of the hydraulic regime, PVC is much smoother than wood, see Table A.1. The type of hydraulic regime depends on the parameter k^+, see Equation A.13. Combining this equation with Equation A.7 and the assumption that the average flow velocities for rivers in the Netherlands reach values up to 2 m/s, results in k^+ value higher than 70. So, the logs in Dutch rivers are in a hydraulic rough regime.

Figure 3.3: Filter material: filling the PVC with sand (left), glueing roughness elements (middle) and final log (right)

Since scaling the viscosity (ν) was not possible and the shear flow velocity (u_*) was lower in a scale model, the roughness (k_r) had to be increased in order to ensure a hydraulic rough regime. Therefore, very fine gravel particles were glued to the PVC-tubes.

The log roughness and the standard deviation of the height of the logs were measured with a laser. The measurement was executed for seven different logs. Using the arithmetic average height parameter the log roughness is calculated by [Gadelmawla et al., 2002]:

$$k_{log} = \frac{1}{n}\sum_{i=1}^{n}|y_i| \tag{3.1}$$

where n is the number of data points, and y_i the distance of profile point i from the mean line. We found a roughness of 0.191 ± 0.023 cm (mean ± SD). The logs including the roughness elements have an average diameter of 4.535 ± 0.043 cm (mean ± SD). In Figure 3.4 an overview of the measured profiles is depicted.

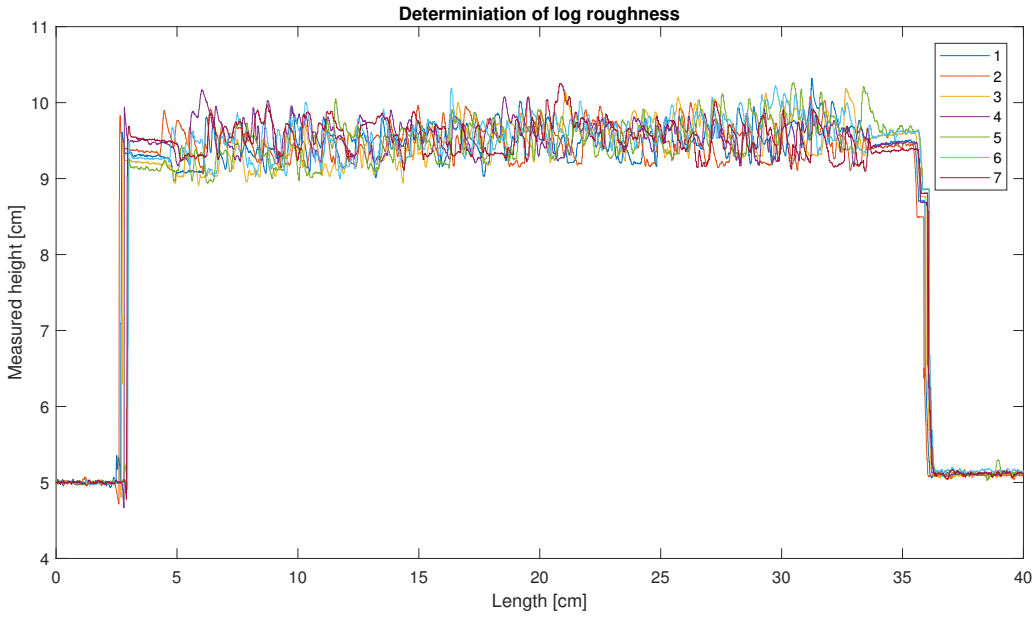

Figure 3.4: Roughness profile of seven different logs measured with the laser. The average diameter of the log is 4.54 cm and the average roughness of the logs is 0.19 cm.

3.3 Used devices

During the experiments, multiple devices are used in order to obtain data. The used devices will be discussed in this section.

3.3.1 Acoustic Doppler Velocimeter

The velocities were measured by two different Acoustic Doppler Velocimeters (ADV) made by Nortek [NortekUSA, 2012]. The transmitter in the ADV generates ultrasound pulses which are confined to a single beam. The ultrasound pulses are scattered by fine particles in the flow and received by three receivers, which register the signal from a well-defined volume. The water motion causes a Doppler shift in the ultrasound frequency proportional to the velocity. The three receivers capture the velocity in all three directions with a sampling rate up to 100 Hz. In this thesis, two different ADV's were used: ADV1+ and ADV2, see Figure 3.5.

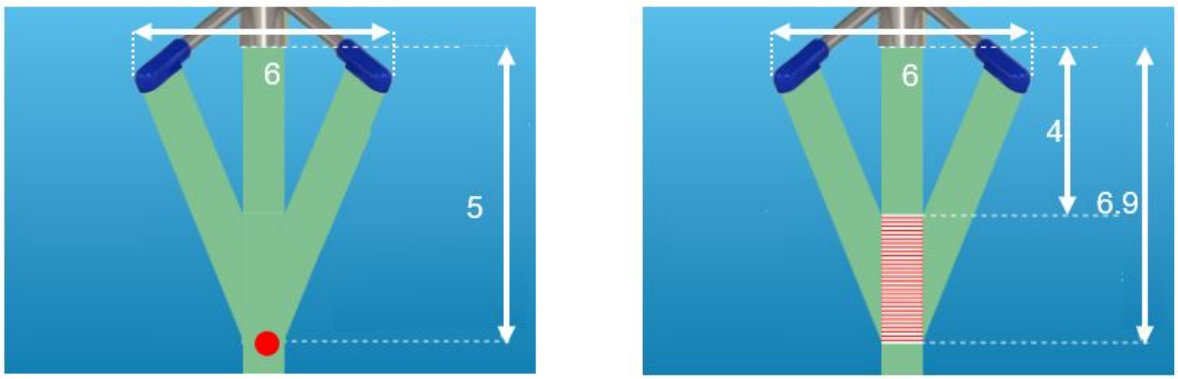

Figure 3.5: ADV1+ (left) and ADV2 (right)

ADV1+ measures the flow velocity at one single point which is located 5 cm from the probe. ADV2 measures the flow velocity in a profile, which is located 4 - 6.9 cm from the probe. However, after executing the first set of experiment, the ADV2 revealed some problems at the edge measurements of the profile, see Figure 3.15. The calibration of the ADV2 is not valid over the full range where it is measuring since it measures values which deviate too much from the theoretical velocity line. The fall off in the profiles is due to the probe geometry and transducer characteristics [NortekUSA, 2012]. Therefore, only the range in the middle of the full range should be considered. The sweet spot is between 4.5 and 5.5 cm, see Figure 3.7.

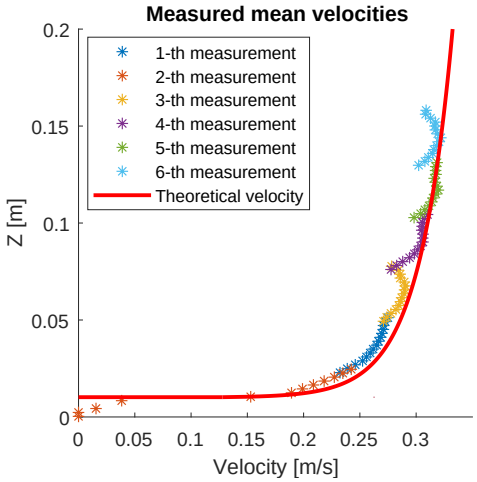

Figure 3.6: measured values (dots) and theoretical velocity profile (red line).

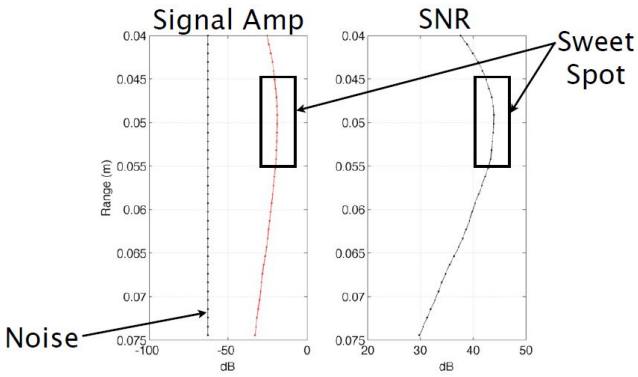

Figure 3.7: Sweet spot ADV2 between 4.5 and 5 5 cm [NortekUSA, 2012].

When the water is too clean the (sound) signal does not reflect and will not travel with the flow in the sampling volume. Whether the signal is deflected or not is given by the Signal-to-Noise Ratio (SNR). The minimum SNR value should be 15 % in order to obtain a reliable signal. When the water is too clean, the water should be seeded. One way to overcome this problem is the use of small air bubbles (0.1 mm) by means of electrolysis. The bubbles are generated just upstream of the measurement point in order to ensure reflection of the noise due to the bubbles. This is done by use of a wire mesh and a stick, see Figure 3.8. In case of measurements inside the filter layer, the bubbles were generated under the device and the log directly.

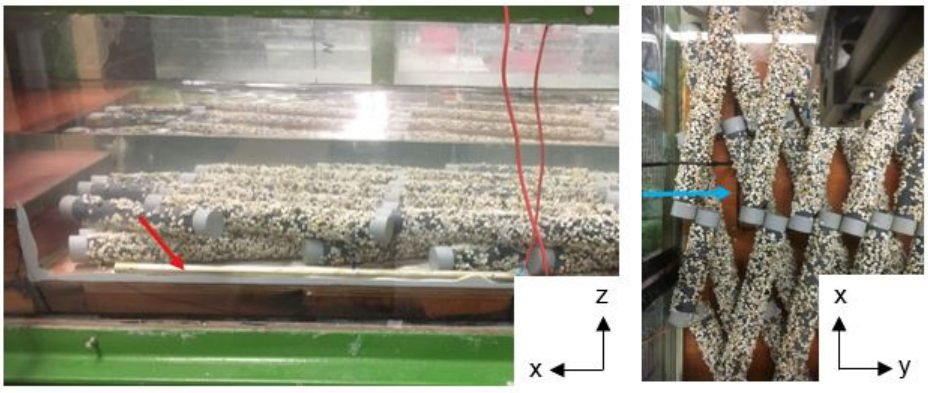

Figure 3.8: Creation of bubbles by electrolyse: stick (red arrow) and wire mesh (blue arrow).

3.3.2 Rehbock weir

The amount of water flowing through the flume, also called discharge, was measured by means of a Rehbock weir underneath the flume. The amount of discharge was obtained by measuring the water level with respect to the height of the Rehbock weir. The water level (h_k) should be measured at a distance of two times the height of the Rehbock wier ($2a$). During the experiments, the water level of the return flume was measured digitally at the side of the flume, see Figure 3.9. Knowing the width of the Rehbock flume, the discharge was calculated by the following formulas:

$$Q = q_{Rehbock} * B_{Rehbock} = m' \frac{2}{3} h_e \sqrt{\frac{2}{3} g h_e} * B_{Rehbock} \tag{3.2}$$

$$m' = 1.045 + 0.141 \frac{h_e}{a} \tag{3.3}$$

$$h_e = h_k + 1.1 \tag{3.4}$$

The discharge given by the Rehbock formula could be validated by a discharge meter at the start of the flume. However, this discharge meter fluctuated too much and therefore the Rehbock weir was preferred.

Figure 3.9: The digital water level measurement (left and middle) of the return flow and the discharge meter (right).

3.4 Model test setup

3.4.1 Placement of the logs

The placement and orientation of the logs is a crucial part of the design of the filter layer since the variables have a large influence of the load reduction on the base layer. Since logs were never used as bottom protection before, no method to place the logs was available. In the past, research has been done in the critical velocity of logs [Haage and Çete, 2016] [van Leeuwen et al., 2016]. They found that logs which were placed aligned with the flow reach higher critical velocities than when the logs are placed perpendicular to the flow.

When designing the filter layer for the scale model, the following points were considered:

- the model should reproduce a real situation: a filter layer which is perfectly aligned with the flow was not possible, since logs are not perfectly straight and it would be difficult to place the trees into the river. Therefore, the logs are probably more jumbles when used as real bottom protection.

- the model should reproduce the porosity as in a real situation: for normal geometrically, a granular open filter has a porosity between $30 - 40\%$. It was assumed that the porosity in a log filter was higher since logs are long and rigid structures. Therefore, it was assumed that the porosity was approximately 50%.
- the design of the filter layer should be practically applicable: it should easy to place the logs.
- there should be no creation of small channels. The filter layer should not consist of long small channels in the longitudinal direction. This would lead to another type of flow which is not present when looking at logs as bottom protection.

When taking the considerations into account the placement and orientation of the logs were arbitrarily chosen and is showed in Figure 3.10. The distance between the logs was one diameter (4.5 cm). When in the longitudinal direction a new set of logs start, the new logs were placed in between the set of two logs upstream in order to prevent the creation of small channels in the filter. The angle of the logs relative to the flume was 20 degrees. The layer on top of the underlayer was placed in the opposite direction of the layer beneath it (see Figure 3.10). The porosity was calculated to be 56%. Due to the wall at the side of the flume, the designed filter had higher porosity's near the walls of the flume (see Figure 3.10). This was taken into account during the erosion measurements.

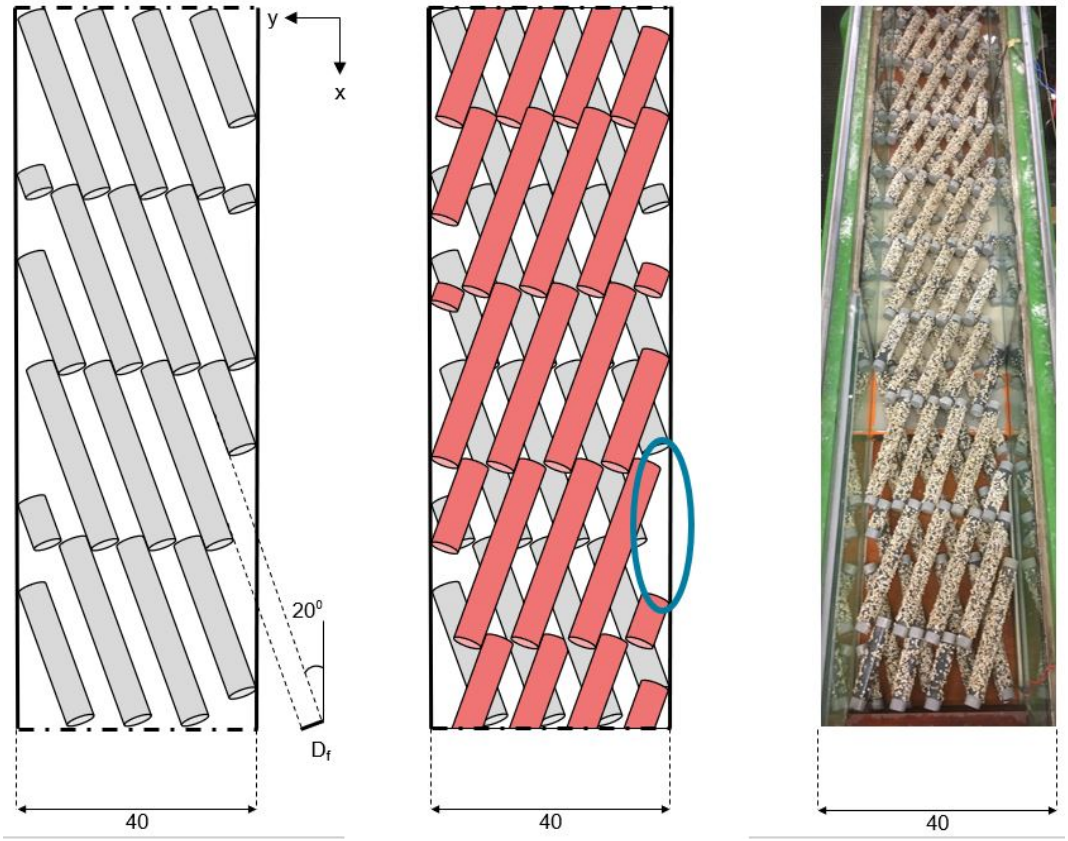

Figure 3.10: Orientation and placement of the logs. Schematised lower filter (left), second layer (middle) and real situation (right). Wall effects resulted in higher porosity's at the side of the flume (for example the region in blue circle).

3.4.2 Velocity and water level measurements

The velocity measurements were done at two different locations (see Figure 3.2):

1. inside the filter layer at location 3;
2. above the filter layer at location 6.

The flow velocity measurements at location 3 were carried out by the ADV2. The measured depth at this location depends on the type of experiment. It was not possible to measure the flow velocities above the filter layer at the same positions since the ADV2 blocked the measurement area and influenced the flow. Therefore, the flow velocities above the filter layer were measured at location 3 with the ADV1+. The water levels were measured at all the locations depicted in Figure 3.1.

3.4.3 Erosion measurements

The experiments were stopped at the moment when erosion due to bed load transport or winnowing occurred. The moment was determined by means of the sediment trap directly downstream of the sandbox. The experiment was stopped when a significant amount of sand was transported into the sediment trap and a constant supply was present.

The sediment trap consisted of stainless steel with a gap in the middle of the channel. Since the porosity of the filter layer was higher due to wall effects of the flume (Section 3.4.1), this region was not considered. The sediment trap was 30 cm long and over the full width of the flume. The gap in the middle was 10 cm wide.

Figure 3.11: Top view (left) and side view (right) of the sediment trap. The moment of erosion is depicted in the bottom right.

The amount of erosion was determined by use of a laser, see Figure 3.12. The laser measured the distance by means of a Voltage between 0-10 V and had a measuring range from 6-26 cm. Since the laser is not waterproof it was positioned in a boat with a perspex bottom in order to stay dry. During the tests, the boat and the laser were submerged in water. The boat was mounted to a cart on the flume and could vary in the longitudinal and transverse direction. Each laser measurement started at the same longitudinal point. The traveled distance from the start point was tracked by a trigger wheel. A three-dimensional bed profile was obtained by assuming linear bed profiles between measured points in longitudinal and transverse direction.

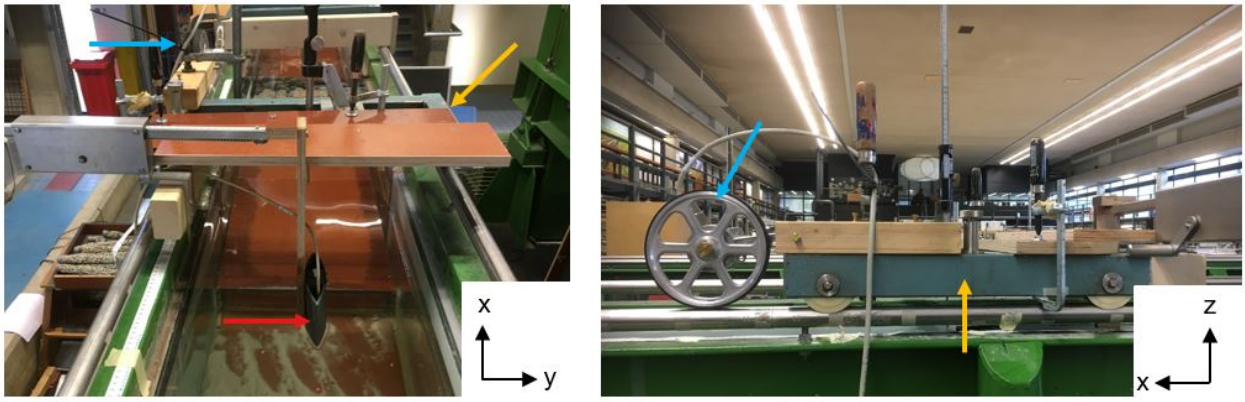

Figure 3.12: Top (left) and side (right) view of the laser in the boat (red arrow), cart (yellow arrow) and trigger wheel (blue arrow).

Figure 3.13 depicts the measured longitudinal region. In total the laser measured over 1.90 m. In the transverse direction, the laser was positioned in 13 different positions with each the same center to center distance and in total 30 cm in the middle of the channel. In total, the measured area was 0.57 m^2.

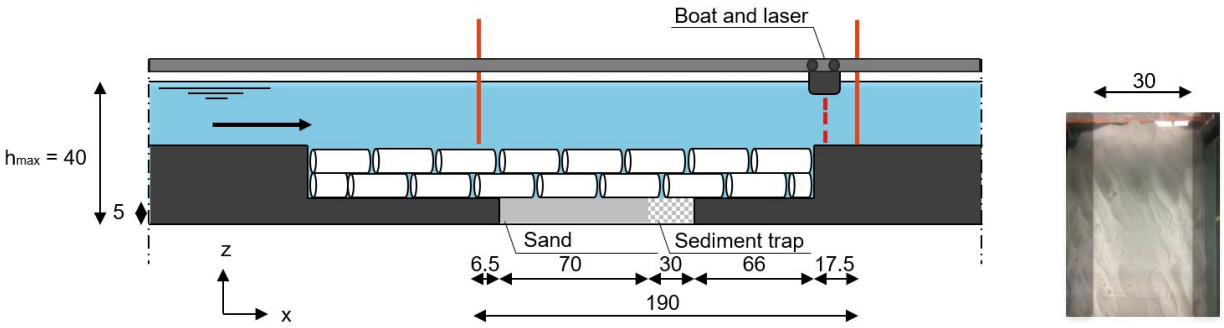

Figure 3.13: Longitudinal (left) and transverse (right) region of the laser.

3.5 Data

3.5.1 Calibration of the laser

For calibration of the laser in the submerged boat, the increasing step of the false bottom was used. The step was used in order to determine the ratio between the measured Voltage and cm. In addition, the Voltage which corresponds to the bottom of the flume was calculated. This value together with the difference in Voltage provided the height of the laser.

3.5.2 Processing

The measured velocities by the ADV's consisted spikes in the signal which could be caused by different factors. At first, when the velocity exceeds the velocity range of the instrument, aliasing can occur. Second, the spike may be caused due to obstacles such as solid particles or air bubbles which block the sound path between the emitter and the receiver. If an obstacle is located in the path of the emitter, the spike is present in all the receivers. If the spike is located in the path of a beam-dependent backscattering, this will only be visible in the concerned beam. Spikes also occur when there are not enough acoustic targets in the water resulting in a signal dropout and a low signal-to-noise ratio (SNR) in all receivers [Doroudian et al., 2010]. Spikes may also appear when

the turbulent intensities are high [Parsheh et al., 2010].

There are multiple methods for detecting spikes of an ADV signal. The most suitable for detecting spikes, but by holding the turbulent motions, is the phase-space thresholding method [Goring and Nikora, 2002]. This method is used for the obtained data in this thesis, see Figure 3.14. The spikes are replaced by a cubic polynomial interpolation of the data on either side of the spike.

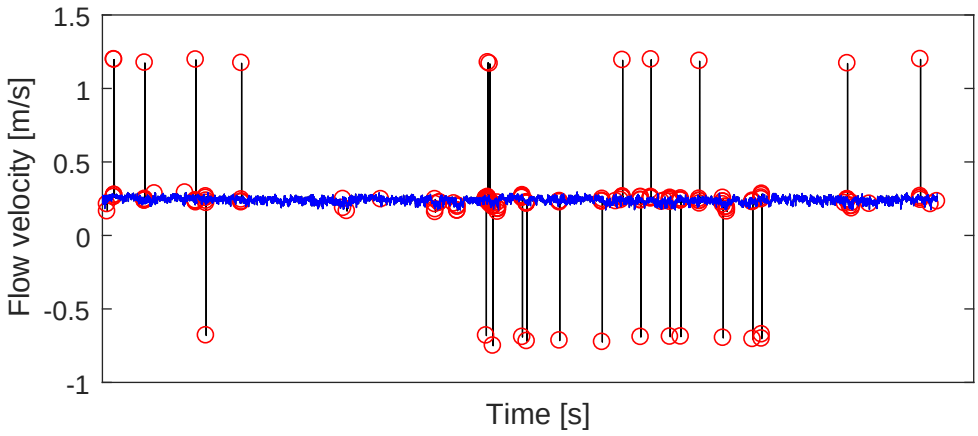

Figure 3.14: Despiking the signal by using the phase-space thresholding method. The red dots are the spikes are removed signals and replaced by a cubic polynomial interpolation.

In order to obtain reliable data, the signal had to have minimum required correlation of 70 % and signal to noise (SNR) ratio of 15 %. Therefore, signals lower than the minimum required correlation and SNR value were removed and not taken into account for the analysis of the data.

The minimum required record time of the ADV depends on the time-averaged value. The length of this period depends on two time scales: the time scale in which the mean motion varies and the characteristic time scale of turbulent motions. The measured velocities fluctuate and a minimum required time is needed in order to measure long enough in which the average velocity does not deviate anymore. In this experimental set-up, the average velocity with averaging time is plotted in Figure 3.15. As can be seen in the figure, the average value does not deviate after measuring 180 seconds. The minimum required signal time regarding mean motion variation is therefore 3 minutes. In order to obtain enough signals with correlation values higher than 70 % and SNR higher than 15 %, we measured 5 minutes. When the total amount of signals was less than 3 minutes (40 percent deleted), the measurement was not used for the analysis.

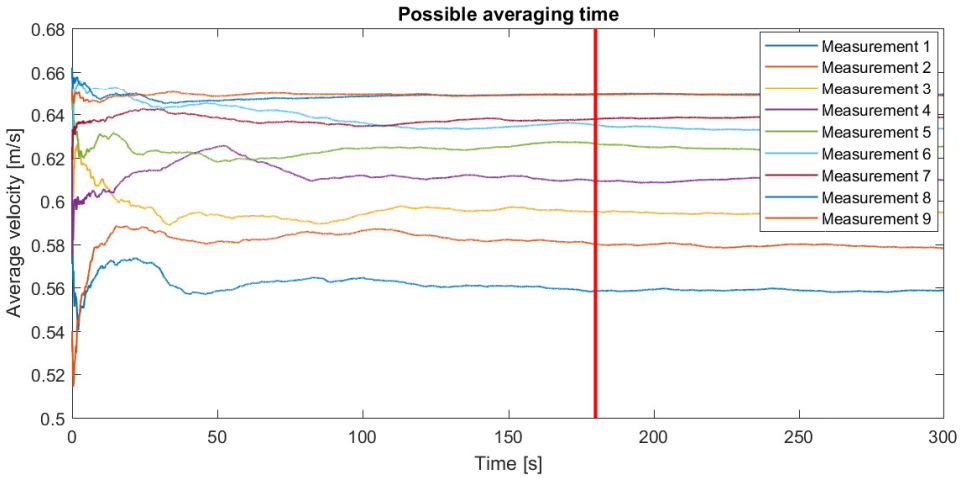

Figure 3.15: Averaging time: after 180 seconds, the average flow velocity does not vary over time.

3.6 Experiments

This paragraph provides the information which scale is used and the boundaries during the experiments. Additionally, the configuration of each experiment is elaborated. At last, the execution of each experiment is shown.

3.6.1 Scale

In this research, the Froude scale is enhanced in order to ensure the same gravitational effects as in the prototype. The length scale is set to be ($n_L =$) 10. The dimensions of the logs are reproduced in such a way that it approaches this length scale. By enhancing the Froude scale, the scale of the velocity becomes $n_v = \sqrt{n_L}$. The scaling for all parameters during the experiment are given in Table 3.2. All dimensions and material properties are elaborated in Section 3.2. The effect of the distorted trees is discussed in Section 6.2.3.

Table 3.2: The prototype dimensions, model dimensions and scales used in this research.

Parameter	Symbol	Unit	Prototype	Model	Scale		
Water depth	h	[cm]	200	20	n_h	=	10
Flow velocity	u	[m/s]	vary	vary	n_v	=	$\sqrt{n_L} = \sqrt{10}$
Grain size base material	d_{b50}	[µm]	300	140	$n_{d_{50b}}$	=	2.14
Roughness filter layer	k_{log}	[mm]	1.5	1.91	n_{log}	=	0.79
Length log	L_{log}	[cm]	500	33	$n_{L_{log}}$	=	15.15
Diameter log	D_{log}	[cm]	50	4.54	$n_{D_{log}}$	=	11.01

To ensure the sediment mobility, the critical Shields number should be equal in both prototype and model ($n_{\psi_c} = 1$). Therefore, Equation 2.44 must hold. The scale effect of the sediment mobility is discussed in Section 6.2.1.

3.6.2 Boundaries

During the experiments, boundaries were present which were provoked by the limits of the flume or due to the structure of the experimental set-up:

- the Froude number had to be lower than 0.6 to ensure sub-critical flow, see Section A.1;
- the Reynolds number had to be higher than 30,000 to neglect scale effects of the Reynolds criterion 2.5;
- the maximum reachable discharge in the flume was 100 l/s;
- the height of the flume was 0.4 m. Due to the false bottom depending on the thickness of the filter layer, the maximum water depth depended on the thickness as well.

The range of experimental conditions is given in Figure 3.16. The mean velocity had to be lower than the Froude number line and higher than the Reynolds number line. In addition, the water layer had to be lower than the limited water depth, otherwise flooding would occur.

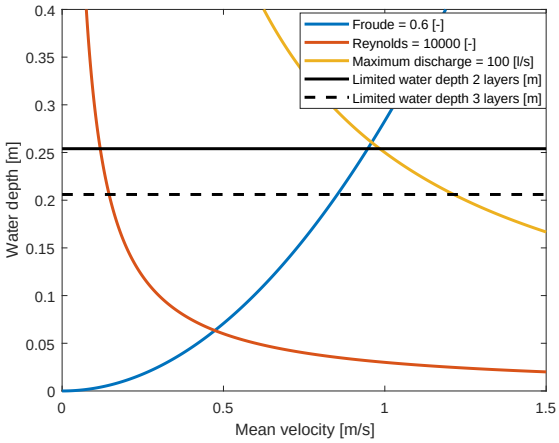

Figure 3.16: Range of conditions of the flume.

3.6.3 Experimental configurations

In total, nine experiments were carried out which were distinguished by three set of experiments, see Figure 3.17:

- First set of experiments (experiment R01, R02 and R03): the flow velocities were measured between the transition of the free flow and the transition of layer 1 and 2. These experiments were carried out with a two-layer filter;
- Second set of experiments (experiment R04, R05, and R06): the flow velocities were measured between the transition of layer 1 and 2 and the transition of layer 2 and 3. These experiments were also carried out with a two-layer filter;
- Third set of experiments (experiment R07, R08 and R09): the flow velocities were measured between the transition of layer 2 and 3 and the transition of layer 3 with the bed. These experiments were carried out with a three-layer filter.

As can be seen in Figure 3.17, the vertical component inside the filter layer is made non-dimensional (z/D_{log}), with z representing the depth inside the filter and D_{log} the average diameter of the log. This is done in order to obtain a clear view when a new layer starts. Hence, at z/D_{log} is zero, we look at the transition between the free flow and the filter layer. When going deeper in the filter layer, this non-dimensional parameter increases. In order to obtain reliable results, each region is measured by three separate experiments, hence one set of experiments.

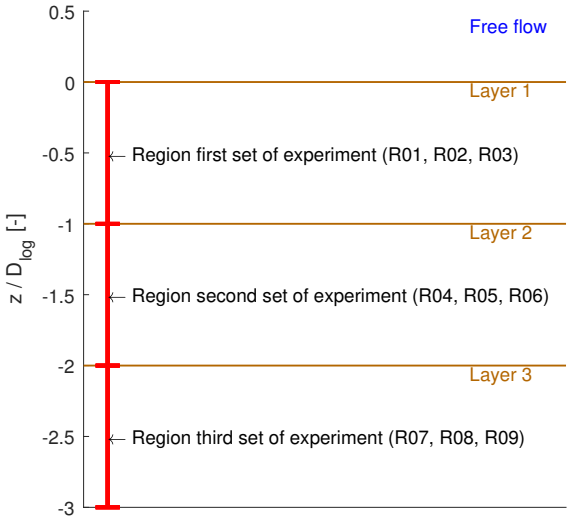

Figure 3.17: Measured regions inside the filter layer of all experiments. In the first set of experiments the water velocities in layer 1 are measured. In the second and third set of experiments the flow velocities were measured in layer 2 and 3, respectively.

Each experiment consisted of several time steps until erosion occurred. Each time step was on average 1.5 hours. At every time step, the discharge was increased. While increasing the discharge, the water level was emulated to be constant by adjusting the weir at the end of the flume. This led to an increased flow velocity in the flume during the experiment. An example is given in Table 3.3.

Table 3.3: Increasing discharge and main velocity each time step (t) of experiment R03.

t	Q [l/s]	h_{weir} [cm]	h_{loc3} [cm]	$\overline{\overline{u}}_{loc3}$ [m/s]
1	26.74	24	21.16	0.32
2	40.23	21	21.04	0.48
3	45.71	19	20.03	0.57
4	46.72	19	20.18	0.58
5	50.37	19	20.70	0.61
6	53.48	18	20.03	0.67
7	56.51	18	20.54	0.69

An separate additional experiment was carried out which described the flow conditions and the development of a new boundary layer over the length of the filter layer in x-direction. This experiment is called R10 and was carried out with the ADV1.

3.6.4 Execution of an experiment

The execution of an experiment is schematically depicted in Figure 3.18. At first, the structure was constructed, i.e. the false bottom, sediment trap, base layer, measurement equipment and filter were placed. Second, the flume was slowly filled with water and a last check was done. Thereafter the measurements started.

At every time step the discharge, water level and flow velocities were measured. At the end of each time step, the filter height was measured by the laser and was checked whether erosion occurred by looking inside the sediment trap. If no erosion occurred, a next time step was introduced in which the average velocity in the flume increased. If erosion occurred, the experiment was stopped. Subsequently, the filer layer last bed measurements were done and the next experiment was constructed.

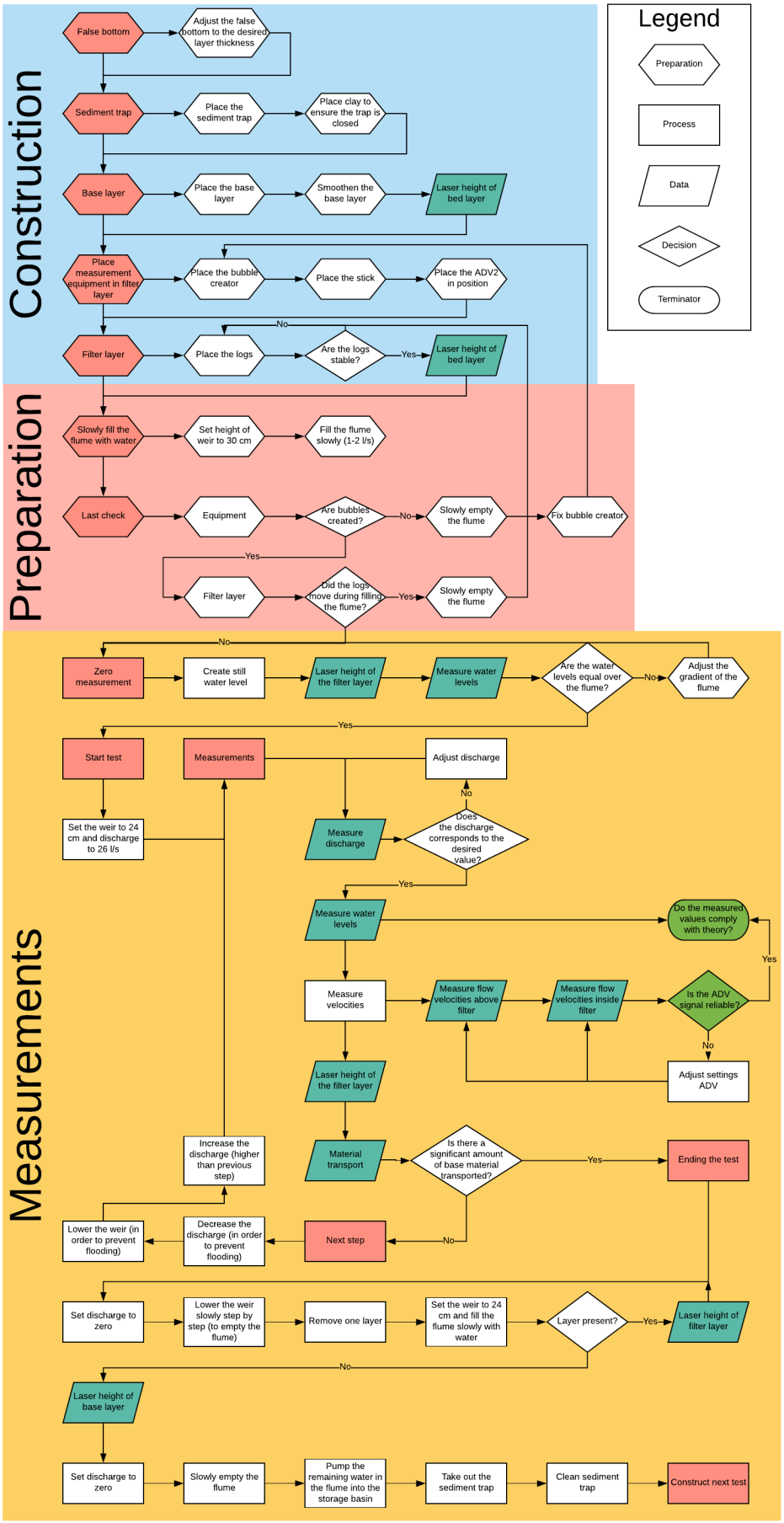

Figure 3.18: Execution of each experiment.

4 Results velocity measurements

During the experiments, flow velocities were measured at two locations: inside the filter layer at location 3 and above the filter, i.e. in the free flow, at location 6 (see Section 3.4.2). In theory, the water level was different at both locations due to the gradient caused by the discharge in the flume. In that case, the average flow velocity over the entire column differed as well. The time step characteristics per experiment are given in Appendix C.1. The calculated averaged flow velocities at both locations during the experiments are given in Table 4.1, 4.2 and 4.3 respectively. We found that the average flow velocity at both locations hardly differed, i.e. maximal 0.03 m/s. This is due to the low gradient of the water level in the flume during the experiments. So, we can conclude that the average flow velocities did not differ between both locations.
Some additional measurements were done:

- While executing experiment R02 and R03, the flow velocity over depth at location 2 were measured with the ADV2.
- During experiment R04 and R05, the flow velocities at location 3 above the filter were measured with the ADV2.

Table 4.1: Average velocities at location 3 and 6 for each time step of the first set of experiments.

Experiment	R01		R02		R03	
t	$\overline{\overline{u_{loc3}}}$ [m/s]	$\overline{\overline{u_{loc6}}}$ [m/s]	$\overline{\overline{u_{loc3}}}$ [m/s]	$\overline{\overline{u_{loc6}}}$ [m/s]	$\overline{\overline{u_{loc3}}}$ [m/s]	$\overline{\overline{u_{loc6}}}$ [m/s]
1	0.12	0.12	0.32	0.32	0.32	0.32
2	0.23	0.23	0.48	0.49	0.48	0.48
3	0.35	0.35	0.58	0.58	0.57	0.58
4	0.49	0.49	0.67	0.67	0.58	0.58
5	0.58	0.59	0.69	0.69	0.61	0.61
6	0.65	0.66	-	-	0.67	0.67
7	0.68	0.69	-	-	0.69	0.70

Table 4.2: Average velocities at location 3 and 6 for each time step of the second set of experiments.

Experiment	R01		R02		R03	
t	$\overline{\overline{u_{loc3}}}$ [m/s]	$\overline{\overline{u_{loc6}}}$ [m/s]	$\overline{\overline{u_{loc3}}}$ [m/s]	$\overline{\overline{u_{loc6}}}$ [m/s]	$\overline{\overline{u_{loc3}}}$ [m/s]	$\overline{\overline{u_{loc6}}}$ [m/s]
1	0.30	0.31	0.30	0.30	0.36	0.36
2	0.36	0.36	0.36	0.36	0.47	0.47
3	0.47	0.48	0.47	0.48	0.56	0.57
4	0.56	0.57	0.56	0.58	0.55	0.55
5	0.60	0.61	0.60	0.62	0.67	0.67
6	-	-	0.66	0.68	0.70	0.71

Table 4.3: Average velocities at location 3 and 6 for each time step of the third set of experiments.

Experiment	R01		R02		R03	
t	$\overline{\overline{u_{loc3}}}$ [m/s]	$\overline{\overline{u_{loc6}}}$ [m/s]	$\overline{\overline{u_{loc3}}}$ [m/s]	$\overline{\overline{u_{loc6}}}$ [m/s]	$\overline{\overline{u_{loc3}}}$ [m/s]	$\overline{\overline{u_{loc6}}}$ [m/s]
1	0.58	0.59	0.50	0.51	0.50	0.51
2	0.62	0.63	0.58	0.59	0.57	0.58
3	0.68	0.69	0.63	0.64	0.62	0.64
4	0.74	0.77	0.69	0.70	0.69	0.71
5	0.77	0.80	0.75	0.77	0.74	0.76
6	-	-	-	-	0.80	0.83

4.1 Assumptions

The flow process above the filter layer is described by means of the results of experiment R10. In this experiment, the flow velocity over the length of the filter layer was measured. During the experiment, the location for each measurement was increased by the length of the log (L_{log}) in the x-direction. The discharge was 50 l/s and the water level was between 20.9 and 20.0 cm, depending on the location. The flow velocity profile over depth in x-direction is depicted in Figure 4.1. In this figure, the uniform flow upstream the filter is clearly visible since the profile has a logarithmic profile over depth. When the filter starts, the flow got disrupted and a new boundary layer was formed.

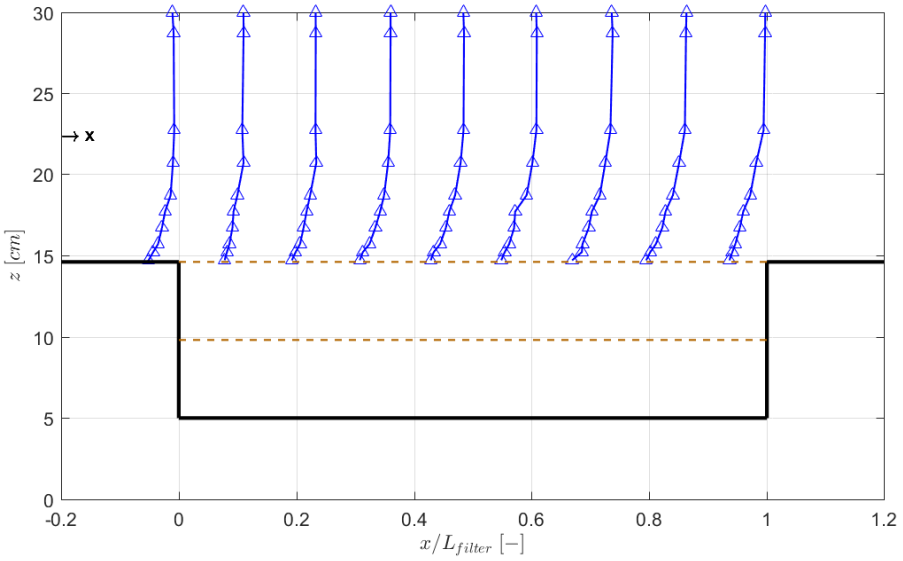

Figure 4.1: Flow velocity profile in x-direction over length of the filter.

The development of the boundary layer was found by fitting the logarithmic profile at the measured point, see Figure 4.2. Figure 4.2a shows that the flow velocity at a certain depth in which both axes is linear. In Figure 4.2b the depth in the water column (z) axis is logarithmic and the time-averaged flow velocity ($\overline{u}$) axis is linear. By fitting a log-linear line of the logarithmic portion of the profile, the characteristic roughness (y_0) and friction velocity (u_*) of each point were estimated. Note that this approach assumes a logarithmic profile of the flow velocity in the streamwise direction. In addition, each location the point near the filter (at $z = 10^{-1}$) was ignored when fitting the log-linear line, since this point did not follow the log-linear trend as the rest of the profile. We suspect that

these points lie within the laminar sub-layer. The characteristic roughness was found at the point where the log-linear fit crosses the y-axis. The friction velocity was calculated by using Equation A.14:

$$u_* = \frac{\kappa \Delta u}{\ln\left(\frac{\Delta z}{y_0}\right)} \tag{4.1}$$

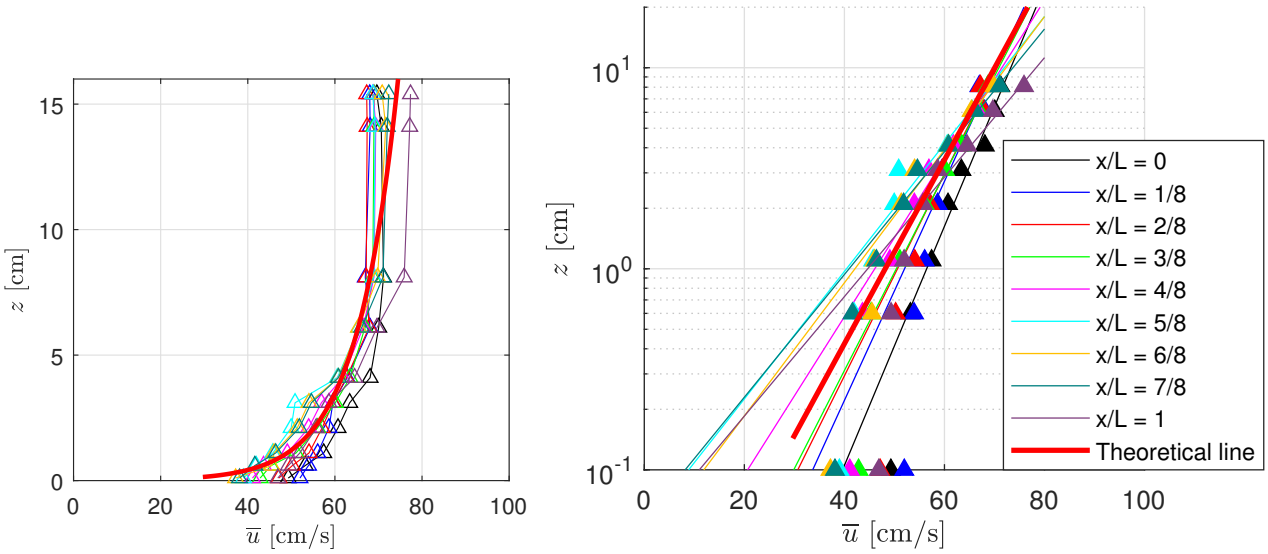

(a) Linear scale (b) Semi logarithmic scale

Figure 4.2: Time-average velocity over depth.

Table 4.4 shows the results of the development of the boundary layer. In this table, the characteristic roughness, friction velocity, k^+ parameter, shear stress and roughness height over the length of the filter are showed. As expected, the characteristic roughness and friction velocity increased over the length of the filter layer. The friction velocity was still increasing at the end of the filter, which indicates that the boundary layer caused by the filter layer was not fully developed. By knowing the friction velocity, the bed shear stress (τ_b) was calculated using Equation A.7. Due to the increasing friction velocity, the bottom shear stress over the length of the filter increased as well. In Section A.2 it was mentioned that a hydraulic rough regime is present when $k^+ > 70$. This is present from $x/L_f = 5/8$ and further downstream. Upstream this point, the flow was in the hydraulic transition regime. Since we assumed that the flow was always in a hydraulic turbulent regime, the roughness height k_r ($= y_0 * 30$) was calculated. At the end of the filter (see Table 4.4) the roughness height was not increasing anymore. This might be due to entry effects: in the begin of the filter inflow of water was present and at the end of the filter the outflow of water was present (see Figure 4.3).

Figure 4.2a also depicts the theoretical line of the velocity over depth, indicated by the red line. Here, the same hydraulic conditions which were present halfway the filter length ($x/L_{log} = 4/8$) were used. By use of Equations A.11, A.14 and A.13 the theoretical flow velocity over depth was calculated. The theoretical line represents a good fit of the measured data. We found a Chézy value of 57.8 $m^{1/2}/s$ for the theoretical line and a Chézy value of 43.5 $m^{1/2}/s$ for the measurements.

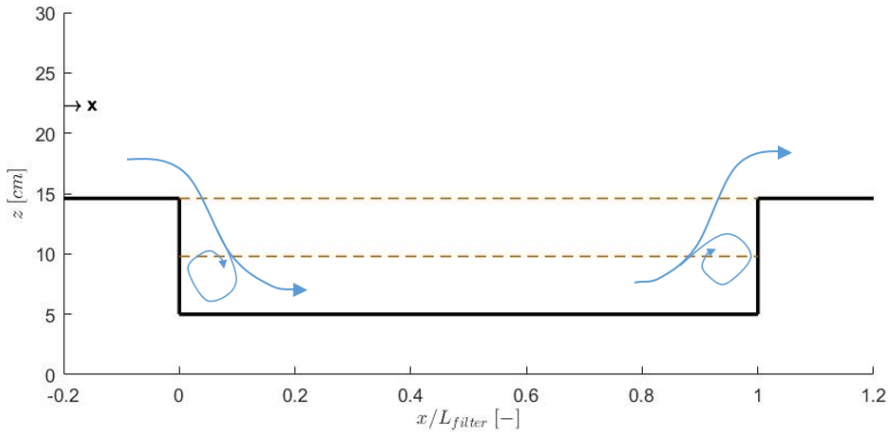

Figure 4.3: Flow velocity profile in x-direction over length of the filter, where the blue arrows depict the inflow and outflow of the water inside the filter layer.

Table 4.4: Development of h, y_0, u_* and τ_b over length of the filter layer.

$\frac{x}{L_f}$ [-]		0	1/8	2/8	3/8	4/8	5/8	6/8	7/8	1
h [cm]		20.9	20.8	20.7	20.6	20.5	20.4	20.3	20.2	20.1
y_0 [m]	$\cdot 10^{-5}$	0.4	1.5	2.9	3.5	15.4	52.3	40.4	56.3	47.1
k^+ [-]		41.94	45.79	49.71	51.15	63.40	78.74	75.39	81.79	84.03
k_r [m]	$\cdot 10^{-3}$	0.13	0.44	0.87	1.05	4.61	15.70	12.11	16.90	14.14
u_* [m/s]	$\cdot 10^{-2}$	2.92	3.19	3.46	3.56	4.41	5.48	5.25	5.70	5.85
τ_b [N/m^2]		0.85	1.01	1.19	1.27	1.95	3.01	2.76	3.24	3.42

During the experiments, the flow velocities inside the filter layer were measured at location $x/L_f = 3/8$, also called location 3. The flow velocities above the filter were measured at location $x/L_f = 5/8$, also called location 6. In order to compare the flow conditions between these locations, experiment R04 and R05 were used. In these experiments, the flow velocities in the free flow above the filter were measured at both locations. The flow conditions during both experiments are given in Table 4.5. We considered two different methods to compare the flow conditions (Reynolds stresses) of both locations:

1. We calculated the shear stress by looking at the fluctuation velocities in x and z-direction, see Equation 4.2. The results are shown in Figure 4.4, in which the shear stress at location 3 and 6 is plotted for time step one, three and four. The solid lines and dots represent the measured shear stresses at location 3 and the dashed line with triangles represent the values of location 6. As can be seen in the figure, the bed shear stresses at location 3 hardly differed from the bed shear stresses at location 6.

2. We assumed a logarithmic profile and used the log-linear assumption (Equation 4.1 and A.7) to calculate the shear stress. Figure 4.5 shows the log-linear plots. The solid lines and dots represent the measured shear stresses at location 3 and the dashed line with triangles represent the values of location 6. The results are presented in Table 4.6. We see that the shear stresses at both locations are approximately the same in experiment R04. However, in experiment R05 the bed shear stress between both locations differed significantly. The sensitivity of logarithmic fit to the measured average velocity make the derivation of the bed

shear stress less reliable. Namely, a small difference in the measured average velocity could lead to a deviation in the friction velocity.

$$\tau_b = \rho\overline{u'w'} \tag{4.2}$$

Table 4.5: Flow conditions of each time step of experiment R04 and R05.

Experiment	R04			R05		
	Q [l/s]	h_{loc3} [cm]	h_{loc6} [cm]	Q [l/s]	h_{loc3} [cm]	h_{loc6} [cm]
t1	25	21.1	20.5	25	20.72	20.60
t2	30	21.15	21.05	31	21.01	20.90
t3	40	21.3	21.11	40	21.32	21.18
t4	45	19.88	19.75	45	19.95	19.26
t5	50	20.95	20.72	50	20.80	20.23
t6	-	-	-	56	21.00	20.35

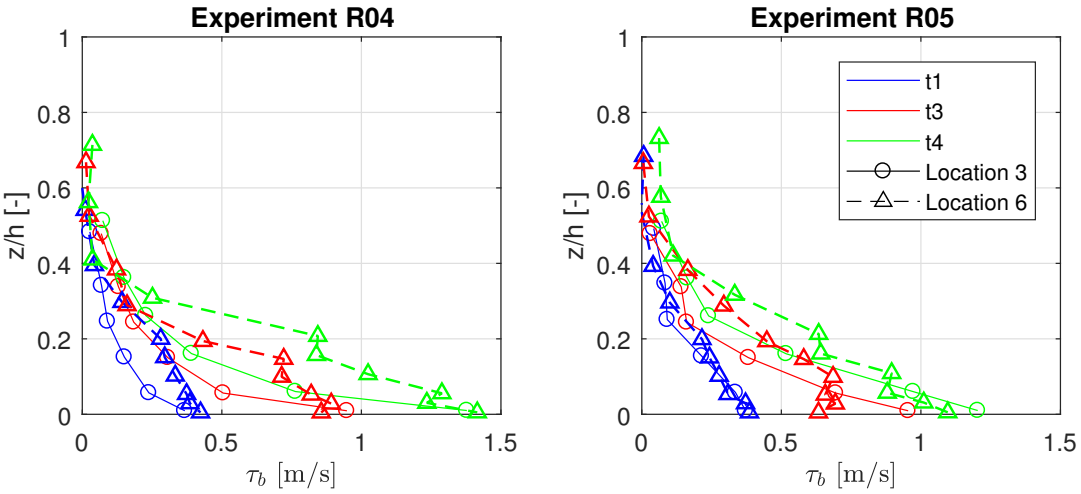

(a) Experiment R04 (b) Experiment R05

Figure 4.4: Difference in shear stress in the free flow between location 3, depicted by the open rounds and straight line, and location 6, depicted by the triangles and dashed line, during experiment R04 and R05 at three different time steps.

Table 4.6: Shear stresses at location 3 and 6 of experiment R04 and R05 using Equation 4.1.

Experiment	R04			R05		
	Q [l/s]	$\tau_{b,loc3}$ [N/m^2]	$\tau_{b,loc6}$ [N/m^2]	Q [l/s]	$\tau_{b,loc3}$ [N/m^2]	$\tau_{b,loc6}$ [N/m^2]
t1	25	0.40	0.42	25	0.42	0.28
t2	30	0.50	0.48	30	0.48	0.69
t3	40	0.58	0.89	40	0.94	0.75
t4	45	1.10	1.07	45	0.95	1.68
t5	50	1.16	1.43	50	1.17	2.58
t6	-	-	-	55	1.27	2.12

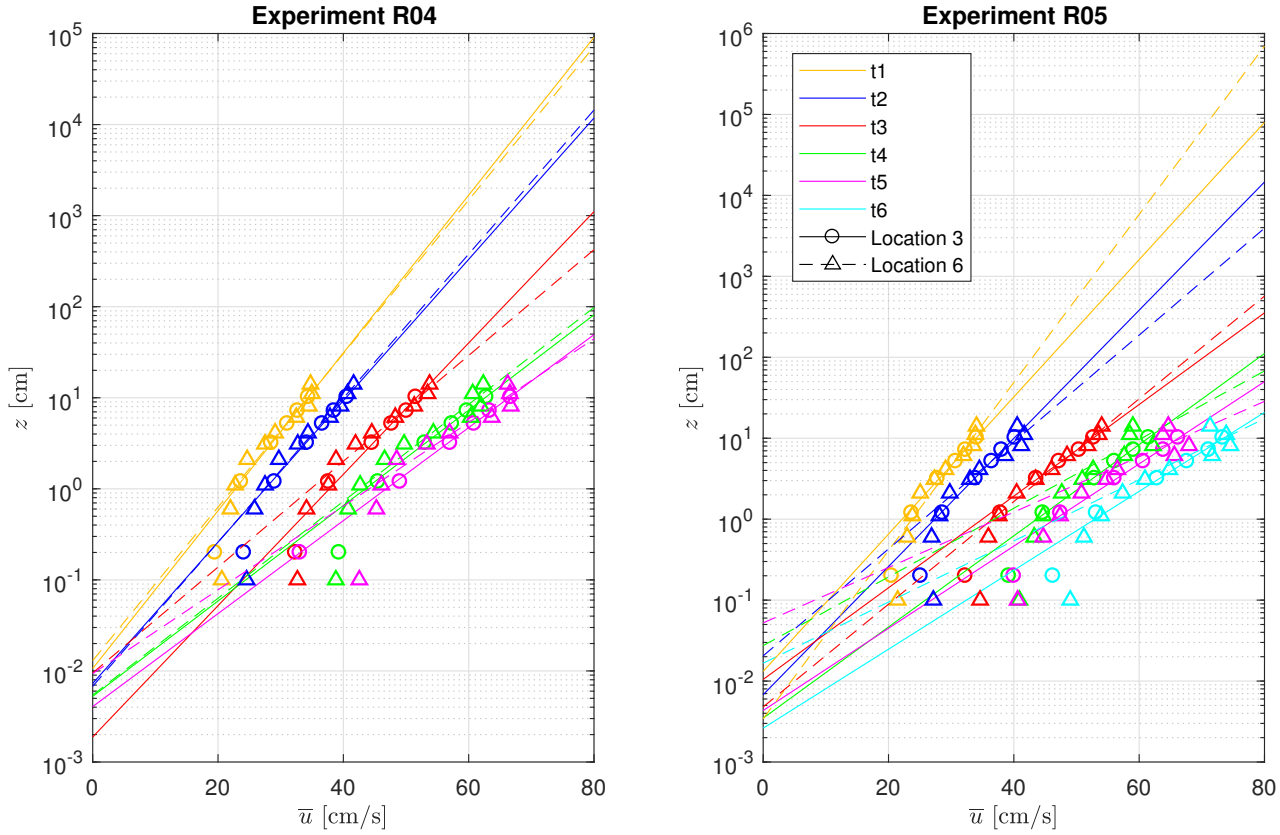

(a) Experiment R04 (b) Experiment R05

Figure 4.5: Difference in shear stress in the free flow between location 3, depicted by the open rounds and straight line, and location 6, depicted by the triangles and dashed line, during experiment R04 and R05 at six different time steps.

By comparing both methods we can conclude the following: the bed shear stress calculated by looking at the fluctuation velocities in x and z-direction gives a similar bed shear stresses at both locations. When using the log-linear assumption approach, the bed shear could differ significantly and is sensitive to the fit. Outliers, i.e. points that deviate from the log-linear fit, have a large influence on the log-linear fit. In addition, it is questionable whether the logarithmic profile over depth assumption could be made at all since we saw, in Table 4.4, that the flow is developing over length.

So, the approach by looking at the fluctuation velocities is preferred over the log-linear approach when analysing the differences between both locations. From this approach, we concluded that the bed shear stresses at both locations (location 3 and 6 respectively) are similar. This is an important conclusion when comparing the flow velocities in the free flow with the flow velocities inside the filter layer. The measured flow velocities in location 6 are also representative for the flow velocities at location 3. Subsequently, it is assumed that the flow in the filter layer is homogeneous: the flow in the filter layer is the same at every location.

4.2 Flow velocities above the filter

During the experiments, the flow velocities above the filter are measured at location 6 (see Figure 3.2). At first, it was assumed to use all measurements for performing the analysis. However, after analysing the measured velocities, we decided to neglect some measured points in some experiments:

- R01 and R03: Measurement 3 was neglected during each time step. Since the average velocity was much lower than in the theory should be, see Appendix C.3.1. In addition, the lowest 4 measurements were not considered as well. Since these values were measured inside the filter layer, i.e. lower than at the transition between the free flow and the logs. In time step 3, measurement 5 is not taken into account, since this gave a non-reliable output signal in the y-direction.
- R02: In this experiment, the lowest 4 measurements were also neglected because the measured location was lower than the transition between the free flow and the logs.
- Measurements in which more than 40% of the signal was deleted due to low correlations ($<$ 70%) and SNR- values ($<$ 30%) were not taken into account, see Figure 4.6. These measurements did not meet the minimal averaging time, see Section 3.5.2. For that reason, these were neglected in the analysis of the flow above the filter.

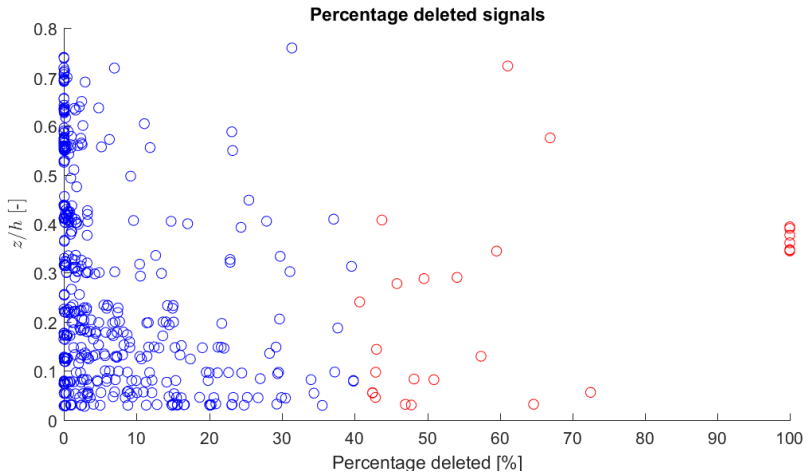

Figure 4.6: Percentage deleted of each measurements due to low correlations ($<$ 70%) and low SNR-values ($<$ 15%). The deleted percentage for each experiments is given. Measurements in which more than 40%, depicted by the red dots, are not considered for the analysis of the flow above the filter.

When neglecting the measurement as mentioned above, we continued with the remained considered measurements. These are depicted in Figure 4.7. In this figure, the measured time-average flow velocity ($\overline{u}$) over depth (h) of each measurement is depicted in blue. Both depths in the water column and flow velocity in x-direction were made non-dimensional in order to combine all measurements. The flow velocity over depth behaves like a logarithmic profile. We conclude that the flow is uniform. When we fit a line through the measurements in the log-linear axis, we obtain the characteristic roughness relative to the water depth ($y_0/h =$) $1.17 \cdot 10^{-3}$. During the experiment, the aim was to keep the average water level of 20 cm. In that case $y_0 = 0.234 \cdot 10^{-3}$ m and the roughness height becomes ($k_r = 30y_0 =$) 7.02 $\cdot 10^{-3}$ m. The same order of magnitude is found in

Experiment R10 (Table 4.4). The corresponding Chezy value is (C=) 53.75 $m^{1/2}/s$. If we compare that with the theoretical Chezy value in the prototype (C = 57.77 $m^{1/2}/s$), this is approximately equal.

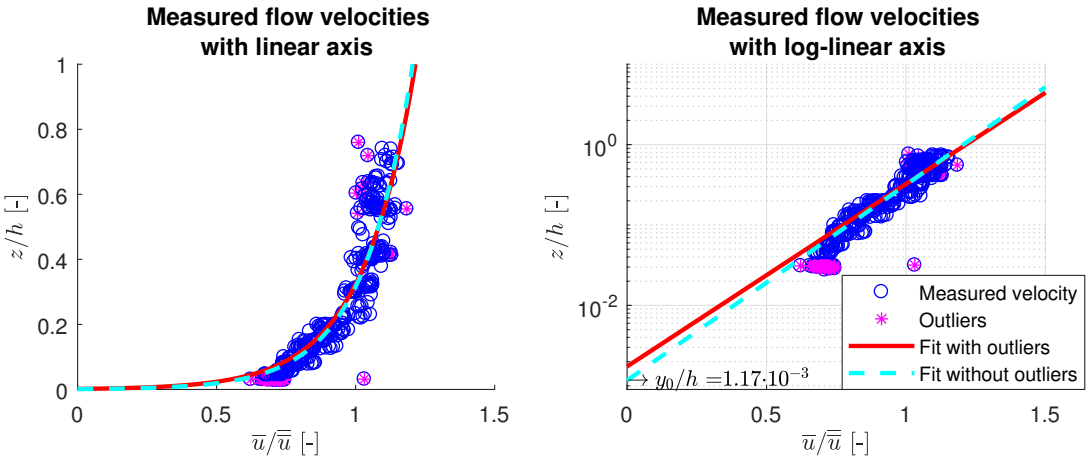

Figure 4.7: Flow velocity over depth relative to the depth-averaged velocity of all measurements in location 6 in x-direction with linear axis (left) and log-linear axis (right).

Appendix C.4 shows the measured average velocities and fluctuation velocities of all experiments. Here, we only considered the relative turbulence. The relative turbulence in all directions over depth is given in Figure 4.8. The relative turbulence increased towards the bed and was almost zero at the surface. The relative turbulence in x- and y-direction behaved similarly and was approximately 0.2 at the transition between the free flow and the filter. The relative turbulence in z-direction was approximately half of the relative turbulence in x and y-direction, i.e. 0.1 at the transition between the free flow and the filter. The relative turbulent kinetic energy was found by combining the three fluctuation velocities of all directions, see Equation 2.2.

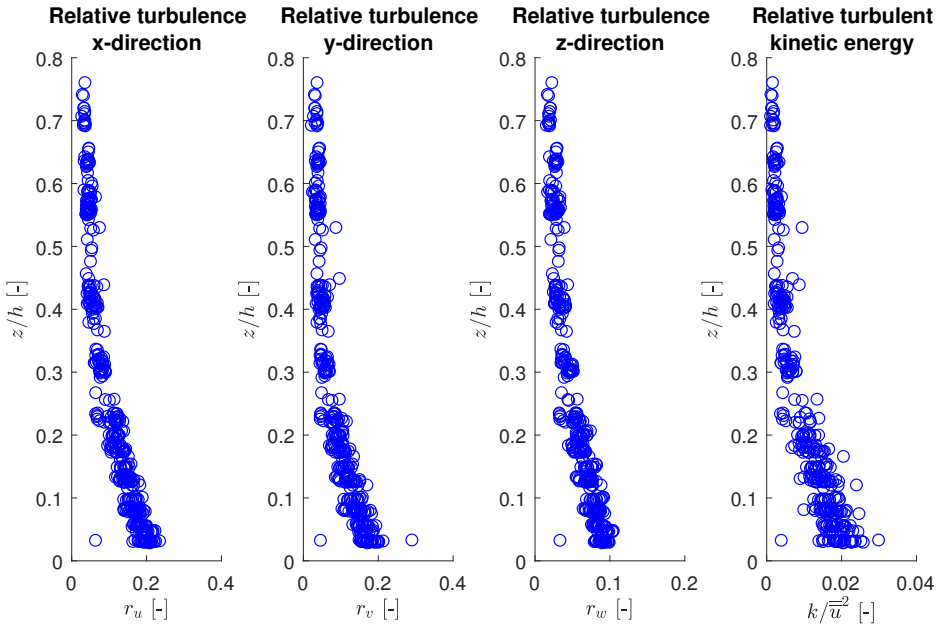

Figure 4.8: Relative turbulence in all directions of all measurement above the filter layer.

In current open filter layer theory, the damping of the turbulence kinetic energy inside the filter layer was determined by a turbulent energy at a reference level. This reference level is located at the transition between the free flow and the first layer. In order to determine this reference turbulent kinetic energy, the relative turbulent kinetic energy was looked into detail in Figure 4.9. Again, the relative turbulent kinetic energy is plotted against the depth in the free flow. The transition between the free and the first filter layer is at $z/h = 0$. In order to determine the turbulent kinetic energy at this level, we only considered the measurements between $z/h = 0$ and $z/h = 0.5$. The measurements above this region were irrelevant for determining the turbulent kinetic energy at the reference point. A linear relation between the level and the turbulent kinetic energy was made in order to determine the average turbulent kinetic energy at the transition between the free flow and the first layer. In this linear assumption, the outliers (extremes) are not taken into account, because the signals are not physical. When looking at the measurement signals, it provides a non-reliable output. The outliers are defined as points at a distance greater than 0.5 standard deviations from the original fit line. Thereafter a new fit of the remaining points is made. By extrapolating this fit to $z/h = 0$ we concluded that the relative turbulent kinetic at the transition between the free flow and the first layer is ($k_{ref}/\overline{u}^2 =$) 0.022.

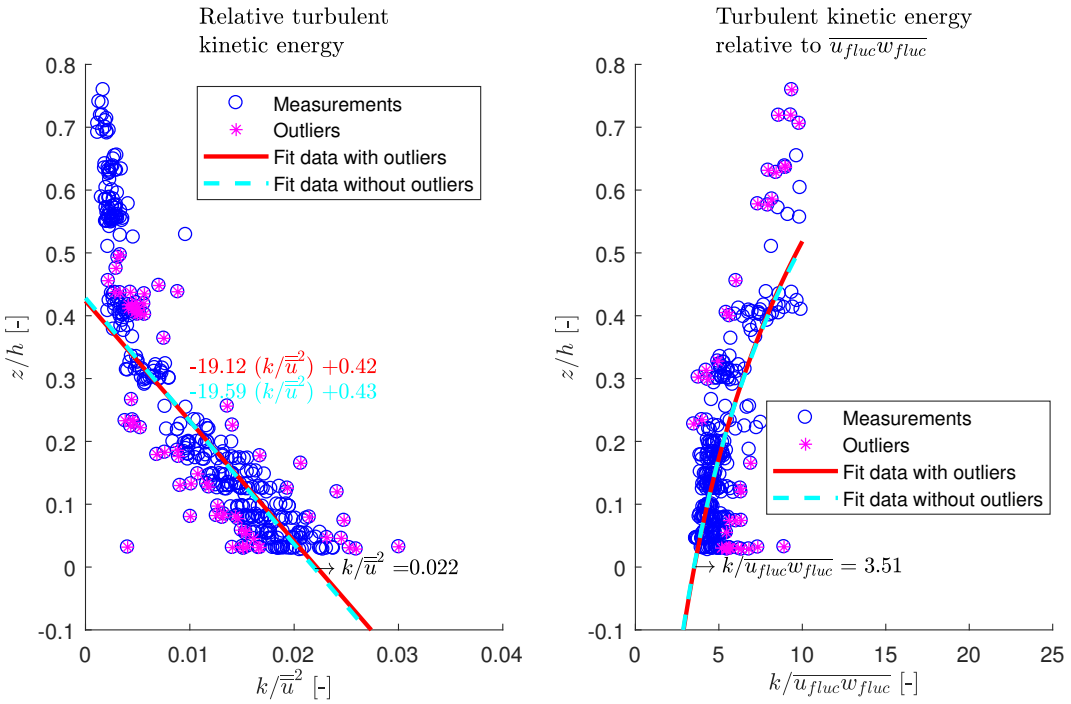

Figure 4.9: Turbulent kinetic energy relative to the depth-averaged flow velocity (left) and relative to $\overline{u_{fluc}w_{fluc}}$ (right). When extrapolating to zero, the outliers are not taken into account.

In order to determine the relation between the turbulent kinetic energy (k_{ref}) and the friction velocity (u_*) at the transition between the free flow and the first layer of logs, the turbulent kinetic energy relative to the average velocity of fluctuation in x and z-direction ($\overline{u'w'}$), also called shear stress, is depicted in Figure 4.9. By fitting a logarithmic line through the measurements, neglecting the outliers, and extrapolating this line, it followed that $k_{ref}/\overline{u'w'} = 3.51$ at the transition between the free flow and the filter.

The friction velocity (u_*) was obtained by combining the results from Figure 4.9:

$$\frac{k}{\overline{\overline{u}}^2} = 0.022 \quad \text{and} \quad \frac{k}{\overline{\overline{u'w'}}} = \frac{k}{u_*^2} = 3.51 \tag{4.3}$$

$$\frac{u_*^2}{\overline{\overline{u}}^2} = \frac{0.022}{3.51} \quad \Rightarrow \quad \frac{u_*}{\overline{\overline{u}}} = 0.079 \tag{4.4}$$

Validation of the relative friction velocity equation ($u_*/\overline{\overline{u}}$) was done by means of experiment R10: $\overline{\overline{u}} = 0.62$ m/s at location 6 ($x/L_{filter} = 5/8$). Combining this with Equation 4.4 leads to $u_* = 4.91 \cdot 10^{-2}$ m/s. Comparing this to the friction velocity determined in Table 4.4 ($u_* = 5.48 \cdot 10^{-2}$ m/s), we see that this is in the same order and the difference is not significant. The difference between the calculated friction velocities can be explained by the fact that the friction velocity in experiment R10 was determined by only 9 measurements. Therefore, the friction velocity was very sensitive to each measurement. Whereas the friction velocity in this section was determined by 242 measurements, excluding the outliers.

4.3 Flow inside filter layer

4.3.1 Decline porous flow velocity over filter thickness

The current theory describes the flow inside the filter layer by means of filter velocity (u_f). Since it was not feasible to measure the filter velocity, the pore velocity (u_p) was measured. The pore velocity was calculated by combining the measured horizontal velocities, in x and y-direction:

$$u_p^2 = u^2 + v^2 \tag{4.5}$$

Normally, a granular open filter consists of rock and the direction of the flow is not considered. In the case of logs, the direction of the flow is of major importance, since it influences the flow characteristics. The flow direction (θ) was calculated by the following equation:

$$\theta = \arctan(\frac{v}{u}) \tag{4.6}$$

In each set of experiments, the average pore velocities were measured at different depths inside the filter layer. The average pore velocities are given in Figure 4.10, 4.11 and 4.12 respectively. Here, the pore velocities are plotted against the depth inside the filter layer. This is the depth in the filter relative to the diameter of the log. It is important to note that:

- The first set of experiments (Experiment R01, R02 and R03) considered the region in the first layer;
- The second set of experiments (Experiment R04, R05 and R06) considered a region in the first layer and second layer;
- The third set of experiment (Experiment R07, R08 and R09) considered the region in the third layer;
- The lowest measurement of each experiment was neglected and not plotted in these figures since these measurements were affected by boundaries, i.e. the bed or the log of the next layer. See Appendix C.3.3 for an example.

By looking at the figures we found that increasing the average velocity above the filter leads to an increase in pore velocity. The effect of increasing the velocity is significant at layer 1 and 2. However, going deeper into layer 3, increasing the average velocity above the filter will not have a significant influence on the increase of pore velocity.

The distribution of the pore velocity over depth can be described as follows:

- in layer 1, the pore velocity is decreasing over depth;
- from the transition between to halfway layer 2, the pore velocity increases;
- from halfway layer 2 to the transition of layer 2 and layer 3, the pore velocity decreases again;
- in layer 3 the pore velocity becomes constant. This does not hold for experiment R09, in which a small increase is present until halfway layer 3.

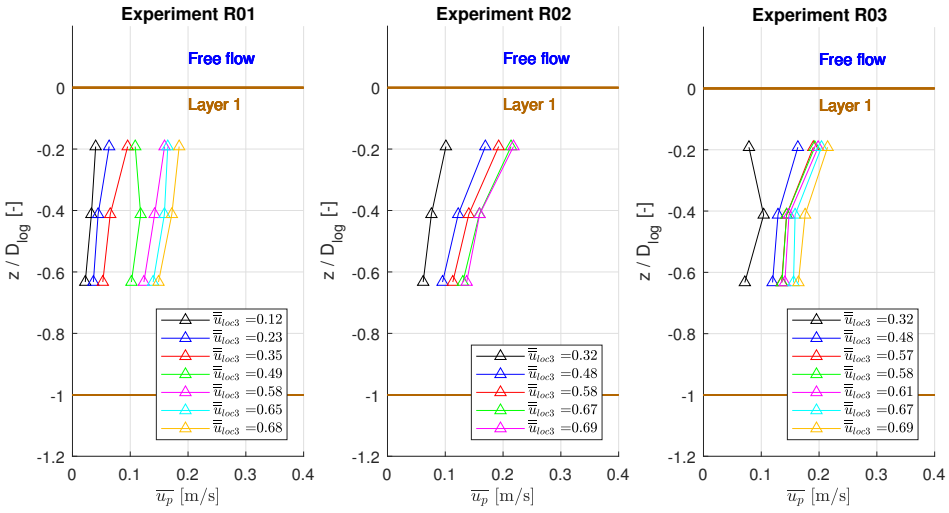

Figure 4.10: Decrease of time-averaged pore velocity over depth inside the filter layer of the first set of experiments. The measured pore velocities with acting depth-averaged flow velocity above the filter are given by the triangles.

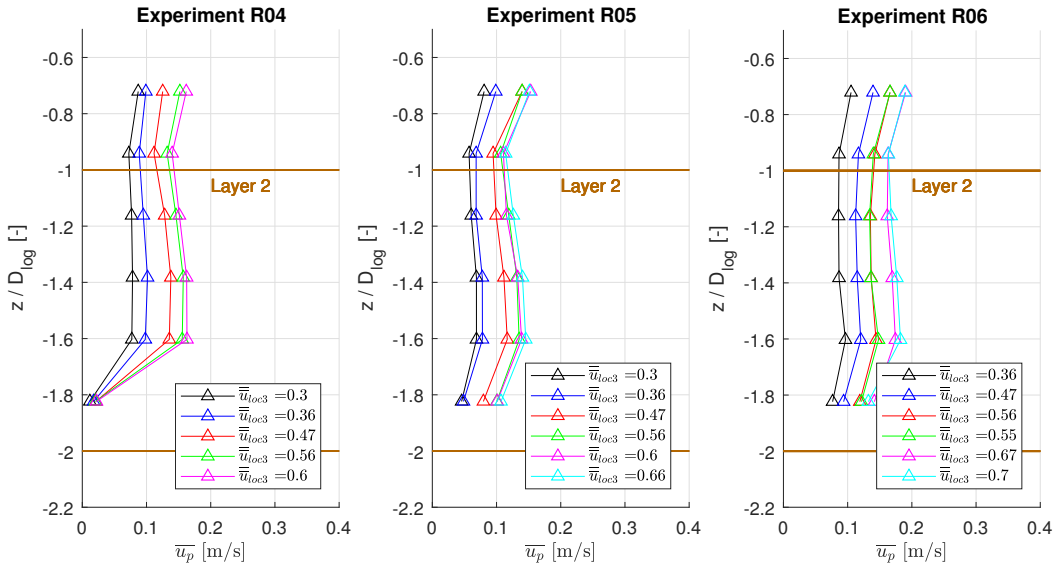

Figure 4.11: Decrease of time-averaged pore velocity over depth inside the filter layer of second set of experiments. The measured pore velocities with acting depth-averaged flow velocity above the filter is given by the triangles

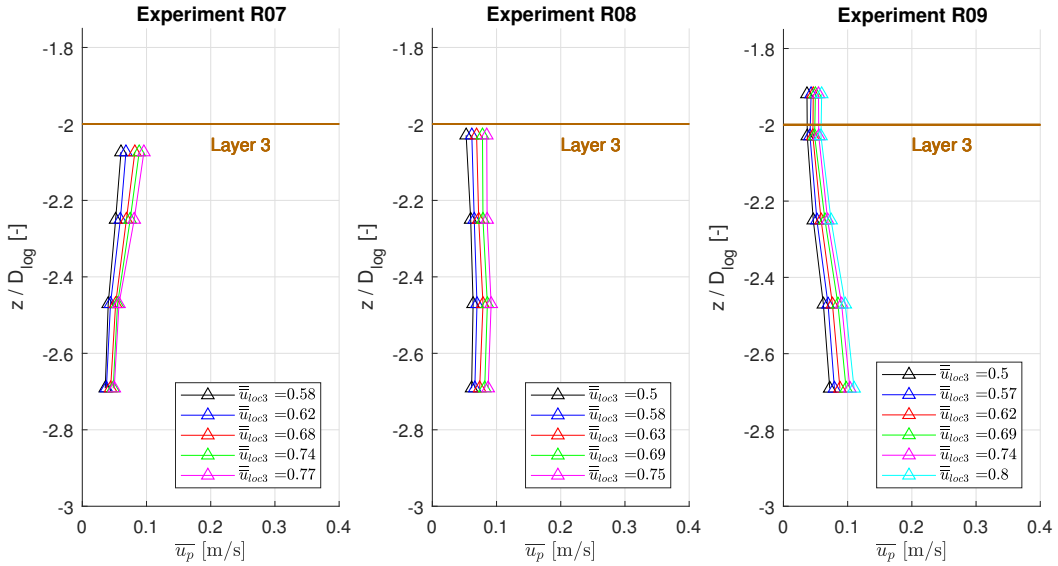

Figure 4.12: Decrease of time-averaged pore velocity over depth inside the filter layer of the third set of experiments. The measured pore velocities with acting depth-averaged flow velocity above the filter are given by the triangles.

The results of all experiments are combined in Figure 4.13. The figure describes the direction (Figure 4.13a), the relative pore flow (Figure 4.13b) and relative vertical flow velocity (Figure 4.13c) over depth inside the filter layer. The absolute relative vertical flow is also given (Figure 4.13d). In each plot, the colours indicate the type experiment and the triangles represent the measured locations.

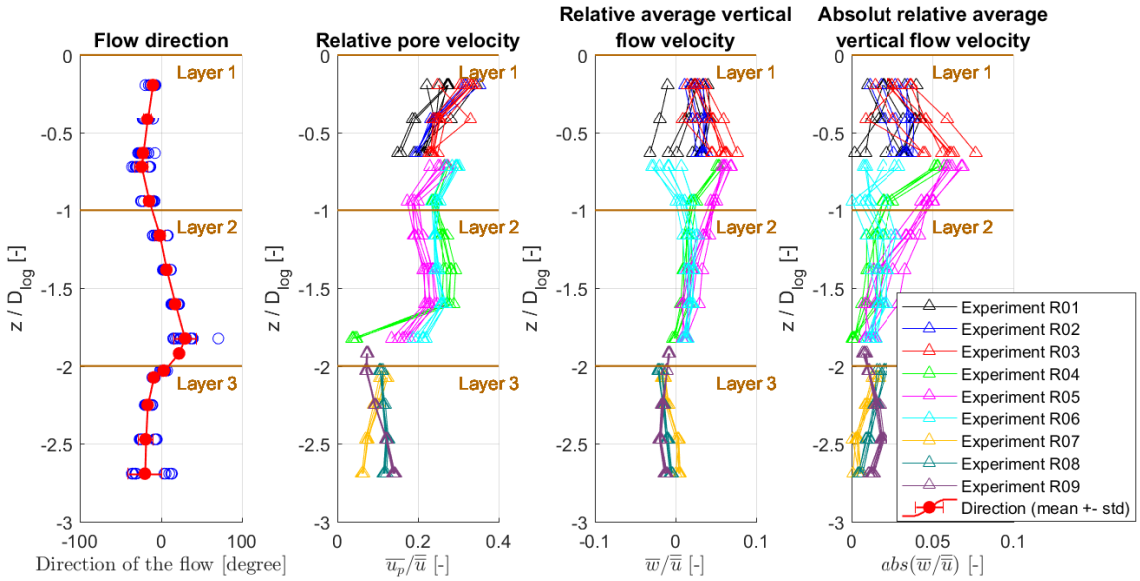

(a) Flow direction

(b) Relative pore velocity

(c) Relative average vertical flow velocity

(d) Absolute relative vertical flow velocity

Figure 4.13: Overview of all experiments over depth of the filter layer: the direction of the flow, relative pore velocity and (absolute) relative vertical flow velocity.

Figure 4.13 shows that:

- the direction of the flow changes at the transition of two layers (see Figure 4.13a). This is caused by the way how the logs are placed, see Section 3.4.1;
- pore velocity (see Figure 4.13b):
  - in layer one, the pore flow velocity decreases over depth;
  - a significant decrease of pore velocity is present slightly above the transition of layer 1 and layer 2;
  - in layer two, the pore velocity is maximum halfway the layer;
  - in layer three, the pore velocity is constant and no decrease of the pore velocity is present;
  - a significant decrease (strong gradient) of the pore flow velocity is present slightly above the transition between layer 2 and 3;
- vertical velocity (see Figures 4.13c and 4.13d):
  - whether the flow is upward or downward depends on the experiment;
  - the maximum vertical flow velocities are found halfway through the first layer. From this point, the vertical flow velocity decreases when going deeper into the filter layer;
  - in layer 3, the vertical velocity is constant.

So, we conclude that:

- the direction of the flow is influenced by the orientation of the logs: when changing the orientation per layer, the direction of the flow also changes;

- at least two layers are needed in order to ensure a significant decrease of the pore velocity;
- the pore flow velocity is not decreasing exponentially over depth;
- a third layer does not lead to a decrease of the pore velocity. Adding more layers will not lead to further reduction of the pore velocities.

From Section 2.4.3 it followed the following: in granular open filters, the pore flow velocity is dominantly caused by the influence of the energy slope at a certain depth inside the filter. The pore flow velocity caused by the energy slope is defined by Equation 2.22:

$$\overline{u_{p,S}} = \sqrt{2gd_{f15}S_e/C_D} \tag{2.22}$$

The calculated pore flow velocities caused by the mean energy slope using this equation are given in Table 4.7. An increase in the gradient of the water flow above the filter resulted in an increase of the pore velocity due to the energy slope ($\overline{u_{p,S}}$). Relative to the average flow velocity, the pore flow velocity does not vary in each time step. We compare this with the deepest measured pore velocity ($\overline{u_{p,dm}}$), i.e. the measured pore velocity at $z/D_{log} = -2.7$ (in Figure 4.13). The velocities at this point are only measured in the third set of experiments, experiment R07, R08 and R09. As can be seen in the table, the relative pore velocities caused by the energy slope is approximately equal to the measured pore velocity in experiment R08 and R09. Since the measured pore flow velocity is constant in layer 3 (from $z/D_{log} = -2.0$ and deeper, see Figure 4.13), we conclude that Equation 2.22 is valid for a filter consisting of logs. In addition, we conclude that the pore velocity in layer 3 is dominantly caused by the influence of the energy slope. Experiment R07 is not considered in this analysis since the gradient is not representative. In this experiment, the measured water levels were inaccurate due to round-off errors resulting in non-representative gradients over the filter.

Table 4.7: The gradient, calculated relative pore velocity caused by the mean energy slope $\overline{u_{p,S}}$ and the relative measured pore velocity of the deepest point $\overline{u_{p,dm}}$. Experiment R07 provide a significant difference. This is caused by roundoff errors of the water level measurements.

Exper-	R07*			R08			R09		
iment	i [‰]	$\frac{\overline{u_{p,S}}}{\overline{u}}$ [-]	$\frac{\overline{u_{p,dm}}}{\overline{u}}$ [-]	i [‰]	$\frac{\overline{u_{p,S}}}{\overline{u}}$ [-]	$\frac{\overline{u_{p,dm}}}{\overline{u}}$ [-]	i [‰]	$\frac{\overline{u_{p,S}}}{\overline{u}}$ [-]	$\frac{\overline{u_{p,dm}}}{\overline{u}}$ [-]
t1	4.7	0.11	0.06	3.0	0.10	0.12	3.0	0.10	0.14
t2	4.0	0.10	0.06	4.2	0.11	0.11	3.8	0.10	0.14
t3	4.1	0.09	0.06	5.6	0.11	0.12	5.6	0.11	0.14
t4	7.4	0.11	0.06	5.0	0.10	0.12	6.0	0.11	0.14
t5	8.5	0.11	0.06	5.9	0.09	0.12	6.8	0.11	0.14
t6	-	-	-	-	-	-	8.2	0.11	0.14

Since we concluded that the pore flow velocity in layer 3 is dominantly caused by the influence of the energy slope, the pore flow velocity caused by the flow over the filter structure should decrease to zero from $z/D_{log} = 0$ to $z/D_{log} = -2.0$. Normally, this pore flow velocity caused by the flow over the filter depends on mean pore flow velocity at the transition between free flow and the filter layer and by the damping coefficient and damping length, see Equation 2.20. From Figure 4.13 we concluded that the pore flow velocity does not decrease exponentially over depth. Therefore, the pore velocity which is caused by the influence of the flow over the filter structure could not be described by Equation 2.20. Although it is difficult to derive a physical formula which quantifies

the decay of the pore flow velocity over depth, the distribution of the pore flow velocity over depth is schematically given in Figure 4.14. In layer 1, the pore flow decreases over depth. From the transition between layer 1 and layer 2, the pore velocity increases until halfway layer 2. From that point, it decreases again. At the transition between layer 2 and layer 3 and deeper, the pore velocity is constant and dominantly depends on the influence of the energy slope.

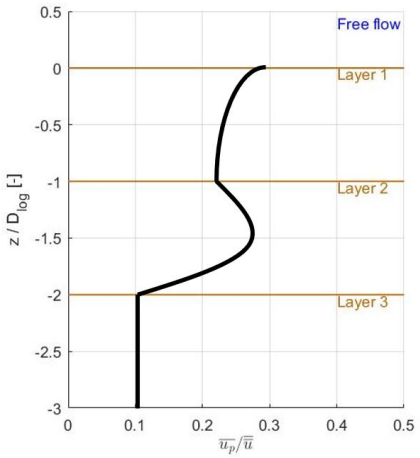

Figure 4.14: Schematically distribution of the pore velocity over depth inside the filter layer.

4.3.2 Decrease of turbulence energy over filter thickness

In current granular open filter theory, the turbulent kinetic energy is determined by the following assumption of Klar (2005): the turbulence in the pores is approximately uniform in all directions [Hoffmans, 2012], see Equation 2.5. At first, it is checked whether this assumption could also be made in the case of logs as bottom protection. Therefore, the relative turbulence per direction is calculated by dividing the root-mean-square velocity by the mean flow velocity above the filter, see Equation 2.2. The average velocity and average fluctuation velocities over depth in all direction of all experiment are given in Appendix C.5.1 and C.5.2 respectively. The relative turbulence over depth in each direction is given in Figure 4.15.

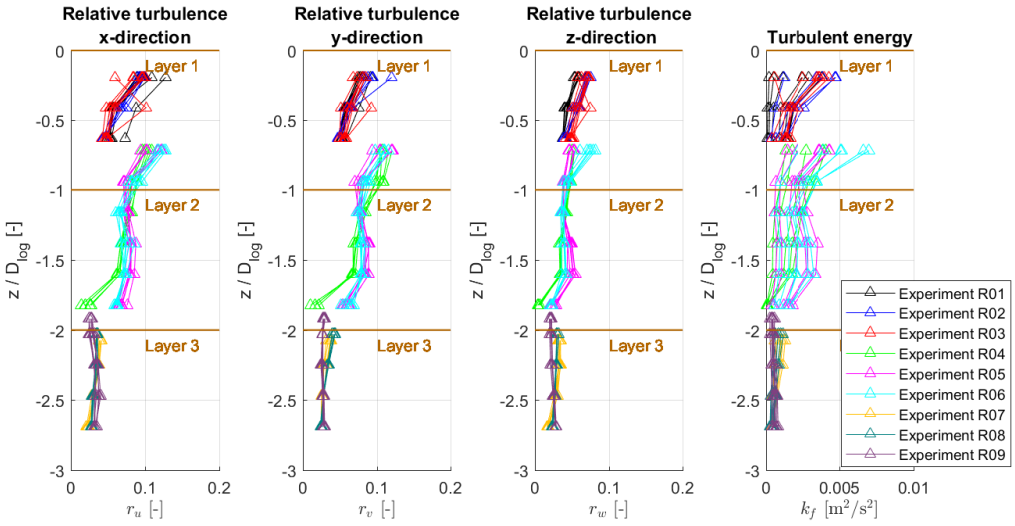

Figure 4.15: Relative turbulence over depth in all direction of all experiments and the turbulent kinetic energy over depth of all experiments.

Figure 4.15 shows the following:

- the relative turbulence in x- and y-direction are similar (r_u and r_v). However, the relative turbulence in the z-direction is approximately 0.5 times the relative turbulence in x- and y-direction. This is caused by the shape of the pores. In granular open filters, the pores are circular, resulting in the same conditions of flow over depth inside the filter layer. In a log filter, this is not the case because the flow is very anisotropic. The shape of the pores deviates from the granular open filter, resulting in deviating flow conditions over depth. This also depends on the way how the logs are structured. See Section 5.1 for further information;
- in layer 1, the relative turbulence decreases over depth. The turbulent kinetic energy decreases exponentially until approximately halfway the layer. From that point, the turbulent energy increases;
- in layer 2, the relative turbulence and turbulent kinetic energy is increasing from the transition between layer 1 and 2 until halfway layer 2. From this point, the relative turbulence and turbulent kinetic energy is decreasing again;
- in layer 1, the highest measurements of the second set of experiments (R04, R05 and R06) are significantly higher than the lowest measurement of the first set of experiments (R01, R02, R03). The turbulence of these points was caused by the way how the logs were placed and how the ADV2 was located. Therefore, the highest measurements of the second set of experiments are neglected;
- in layer 3, the relative turbulent and turbulent kinetic energy is constant over depth;
- a significant decrease (strong gradient) of the turbulent kinetic energy is present slightly above the transition between layer 2 and 3.

From these observations we conclude the following:

- the assumption of Klar, which stated that the relative turbulence in the pores is approximately uniform in all direction, is not valid in case of a log filter. Equation 2.2 should be used to calculate the turbulent kinetic energy;
- at least two layers are needed in order to ensure a significant decrease of the turbulent kinetic energy;
- the turbulent kinetic energy is not decreasing exponentially over depth;
- a third layer does not lead to a decrease of the pore velocity. Adding more layers will not lead to further reduction of the pore velocities;
- in case of a log filter, the turbulent kinetic energy is constant at $z/D_{log} = -2$, whereas in granular filters, following the curve of Klar (2005), this is at $z/d_{f50} = -5$. Moreover, the decrease does not follow an exponential decline as in the curve of Klar for granular open filters.

From Section 2.4.4 it followed the following: in granular open filters, the turbulent kinetic energy is dominantly caused by the influence of the energy slope at a certain depth inside the filter layer. If the filter Reynolds number (Re_f) ranges from 10^3 to 10^5, the local turbulent kinetic energy caused by the energy slope ($k_{f,S}$) can be calculated by Equation 2.25 [Hoffmans, 2012]:

$$k_{f,S} = \frac{2gr_f^2 S_e d_{f15}}{C_D} \tag{2.25}$$

In Section 4.3.3 it is elaborated that the filter Reynolds number in case of logs ranges from 10^3 to 10^5. Therefore, in granular open filters, this equation is valid to use. The calculated turbulent kinetic filter energy caused by the mean energy slope is given in Table 4.8. An increase in the gradient of the flow above the filter (i) leads to an increase of the turbulent kinetic filter energy ($\overline{k_{f,S}}$). We compare the relative turbulent kinetic filter energy caused by the energy slope with the deepest measured turbulent kinetic energy ($\overline{k_{f,dm}}$), i.e. the measured pore velocity at z/D_{log} = -2.7 (in Figure 4.13). The velocities at this point are only measured in the third set of experiments, experiment R07, R08 and R09. Only experiment R08 and R09 are considered in Table 4.8, since we saw that the water levels measured at experiment R07 were not accurate due to round off errors, see Table 4.7. Table 4.8 shows that the calculated turbulent kinetic filter energy caused by the energy slope is approximately equal to the measured turbulent kinetic filter energy in experiment R08 and R09.

Since the turbulent kinetic filter energy in layer 3 is constant (from $z/D_{log} = -2.0$ and deeper, see Figure 4.15), we conclude that Equation 2.25 is valid for a log filter. In addition, we conclude that the turbulent kinetic energy in layer 3 is dominantly caused by the influence of the energy slope.

Table 4.8: The gradient, calculated turbulent kinetic energy caused by the mean energy slope $\overline{k_{f,S}}$ and the measured turbulent kinetic energy of the deepest point $\overline{k_{f,dm}}$.

Experiment	R08			R09		
$\cdot 10^{-4}$	i [-]	$\overline{k_{f,S}}$ [m^2/s^2]	$\overline{k_{f,dm}}$ [m^2/s^2]	i [-]	$\overline{k_{f,S}}$ [m^2/s^2]	$\overline{k_{f,dm}}$ [m^2/s^2]
t1	30	3.39	2.61	30	3.35	3.66
t2	42	4.75	3.05	38	4.24	4.45
t3	56	6.32	3.61	56	6.35	5.23
t4	50	5.60	4.72	60	6.78	6.48
t5	59	6.66	5.54	68	7.72	6.97
t6	-	-	-	82	9.24	8.00

The turbulent kinetic energy caused by the flow over depth in granular filters depends on the turbulent energy at the transition between free flow and the filter layer and by the damping coefficient. In granular open filters, the turbulent kinetic energy decreases exponentially over depth inside the filter layer. In Figure 4.15 we found that the turbulent kinetic energy does not decrease exponentially over depth. Hence, the filter turbulent kinetic energy over depth could not be described by Equation 2.24. Although it is difficult to derive a physical formula describing the decay of the filter turbulent kinetic energy over depth, the distribution of filter turbulent kinetic energy over depth is schematically given in Figure 4.16. At the transition between the free flow and the first layer, $k_f/\overline{u} = 0.022$, see Section 4.2 and Figure 4.9. In layer one, the turbulent kinetic energy decreases exponentially up to approximately halfway the layer. From that point the turbulent kinetic energy increases until halfway layer 2. When going deeper in layer 2 it decreases again. At the transition between layer 2 and layer 3, the turbulent kinetic energy has reached its value where it dominantly depends on the energy slope. Therefore, the turbulent kinetic energy is constant in layer 3.

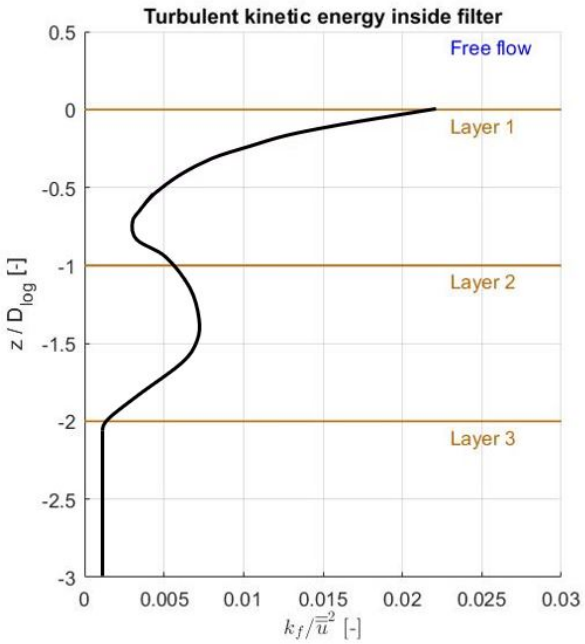

Figure 4.16: Schematically distribution of the filter turbulent kinetic energy over depth inside the filter layer into detail.

4.3.3 Damping coefficient and damping length

In granular open filters, the damping of the pore flow velocity and turbulent energy depends on the damping coefficient (α_d), see Section 2.4.3 and 2.4.4. This damping coefficient depends on a constant α_d, see Equation 2.29. When the filter Reynolds number (Re_f) ranges from 10^3 to 10^5, the drag coefficient is constant, see Figure 2.8. In that case, Equation 2.30 could be used to determine the damping coefficient and the relative filter turbulence is constant over depth (see Equation 2.28).

The filter Reynolds number of all measurements is showed in Figure 4.17 and calculated by using Equation 2.19. This figure shows that the filter Reynolds number ranges from $0.5 \cdot 10^5$ to $7 \cdot 10^5$. Hence, the flow in the filter is turbulent. Therefore, the drag coefficient is constant and Equation 2.30 is valid in case of logs as bottom protection. So, the relative filter turbulence should be constant over depth and Equation 2.31 is used to calculate the damping coefficient:

$$\alpha_d = \frac{2r_f^2}{C_D \chi_k} \tag{2.31}$$

The local relative filter turbulence intensity is also depicted in Figure 4.17 and was calculated by using Equation 2.26. As can be seen in the figure, the local relative filter turbulence intensity does not vary over depth and is constant. We conclude that Equation 2.28 could be used to determine the relative filter turbulence (r_f). The relative filter turbulence constant is found to be $r_f = 0.356 \pm 0.068$ (mean $\pm$ std). The averaged value for the relative filter turbulence combined with Equation 2.31 and the assumption that the flow is in an hydraulic rough regime ($\chi_k = 3.3$) and $C_D = 1$, results in a damping coefficient (α_d) of 0.079. The damping length becomes ($L_d = \alpha_d * D_{log} =$) 0.0035 m.

In granular open filter, we know that the relative filter turbulence is around ($r_{f,normal} \approx$) 1. If we compare this with the relative filter turbulence found in this research ($r_{f,log} =$) 0.36, we conclude

that the relative filter turbulence in case of logs is significantly lower than granular open filters. This influences the damping coefficient and damping length as well.

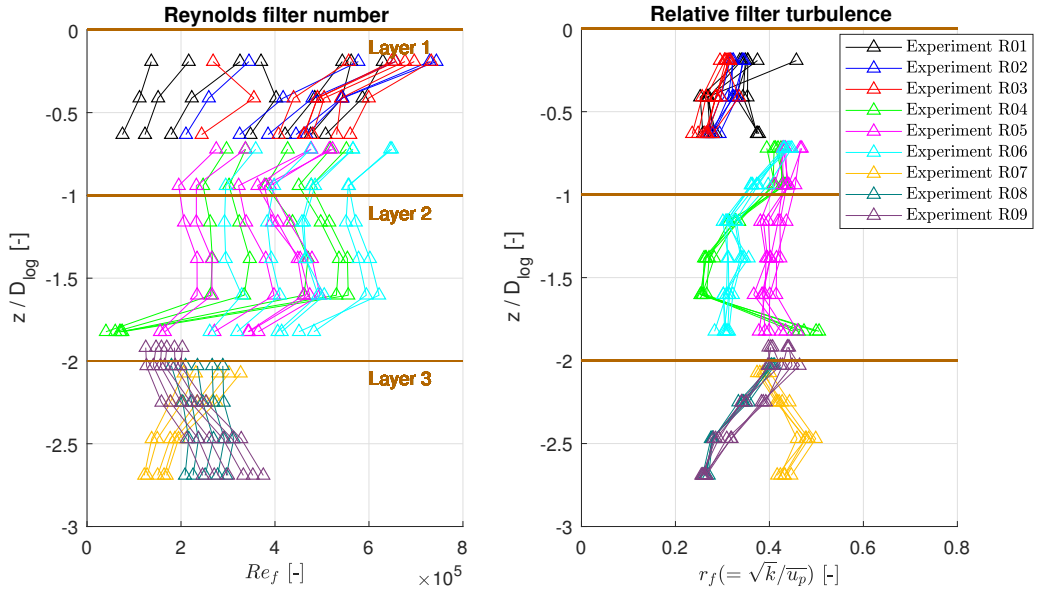

Figure 4.17: Filter Reynolds number (left) and relative turbulent filter energy (right) over depth inside the filter layer.

From this section we conclude the following:

- the flow in the filter consisting of logs is always turbulent;
- Equation 2.30 and Equation 2.31 are valid to use for the calculation of the damping parameter, since the filter Reynolds number ranges from 10^3 to 10^5;
- the relative filter turbulence over depth ($r_{f,log} = 0.356$) in case of logs is constant and much lower than granular open filter ($r_{f,normal} \approx$) 1, resulting in a lower damping length as well.

4.4 Vortices

The characteristic time scale of the vortices (T_{char}) is calculated by means of an autocorrelation function of the vertical flow velocity signal, see Section A.10. An example of the autocorrelation function of one measurement in the free flow and on measurement inside the filter layer is given in Figure 4.18. At $\tau = 0$ the autocorrelation is fully correlated and therefore equal to one. At the end of the record time, the cumulative autocorrelation function approaches zero. The area of interest is the area from $\tau = 0$ to the point where the autocorrelation function approaches values of zero. In this figure, this is one second. Higher lag times are not relevant since these values are completely uncorrelated.

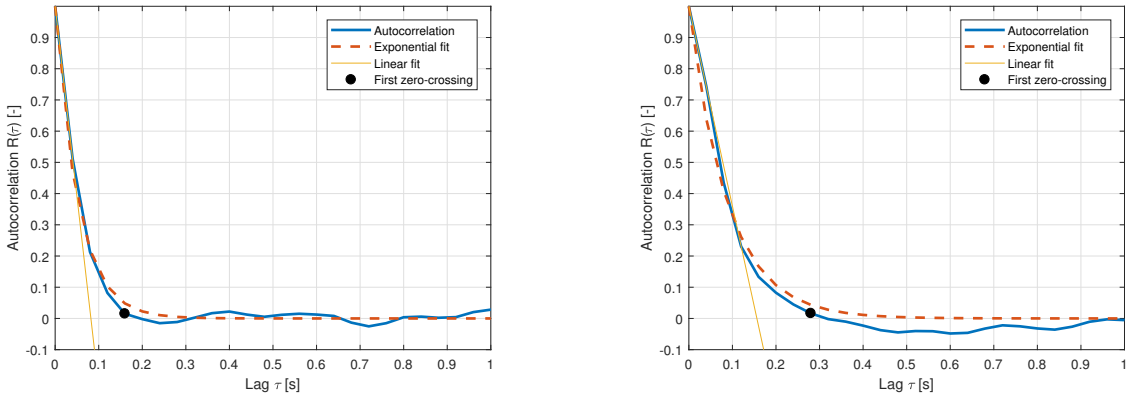

(a) Experiment R05: time step 3 measurement 8 (b) Experiment R05: time step 3 measurement 2.

Figure 4.18: Autocorrelation function of experiment R05 time step 3 in the free flow and inside the filter layer (blue line). An exponential fit (orange dashed line) is made of the data between $\tau = 0$ and the point where the autocorrelation function reaches zero. Also a linear fit between the first two data point is depicted (yellow line).

The Macro timescale is approached by means of an exponential fit from the start of the autocorrelation function ($\tau = 0$) to the point when it crosses zero for the first time, see the orange dashed line in Figure 4.18. The Macro timescale is calculated by taking the integral of this exponential function, see Equation A.69. Figure 4.18 shows that the autocorrelation function in the filter layer reaches zero (Figure 4.18b) at a higher lag time than in the autocorrelation function in the free flow (Figure 4.18a). This indicates that the characteristic Macro timescale, also called characteristic time (T_{char}), is higher in the filter layer than in the free flow. The Macro length scale (L_{char}) is determined by using the frozen turbulence approximation: multiply the Macro timescale with the local average pore velocity, see Equation A.71. Normally, the Taylor micro timescale is determined by the double gradient through the first two point of the autocorrelation function (Equation A.70). The Taylor micro timescale will not be further considered in this research.

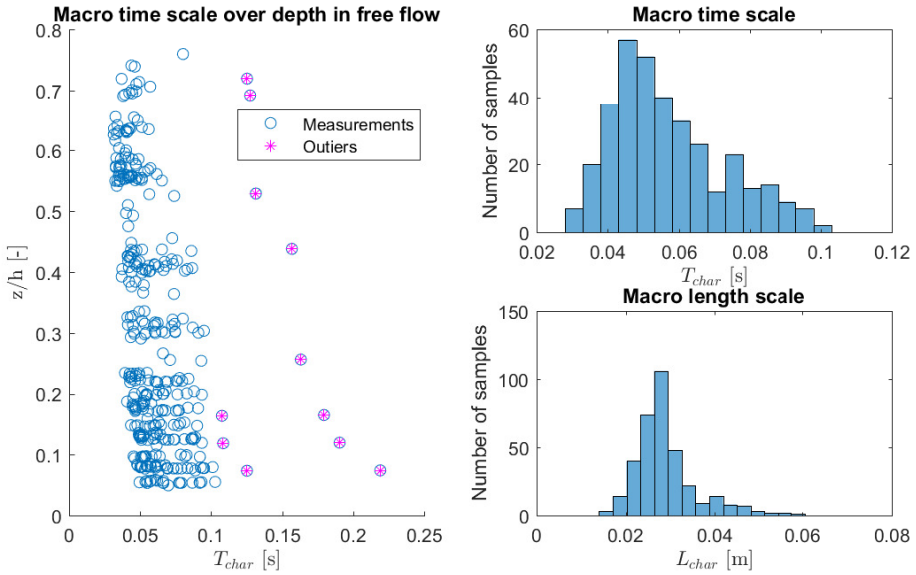

Figure 4.19: Characteristic time and length scale of the vortices above filter.

Figure 4.18 shows only one autocorrelation function of the free flow above the filter. This procedure is done for all measurements in the free flow, resulting in calculated characteristic time over depth, see Figure 4.19. The outliers, values which deviate more than 2 times the standard deviation from the mean, are excluded and histograms of the characteristic time and length scale of the remained measurements are made. From these histograms, we see that the majority of the measurement shows a timescale of 0.05 s and length scale of 0.028 m. The highest time and length scales are 0.11 s and 0.06 m respectively. Note that Figure 4.19 shows the average size of an eddy in a measurement. So, in each measurement, higher and lower eddies were present. Hence, during the measurements, larger eddies than 0.06 m were present, but these eddies could not be calculated separately. In addition, the histograms consist of measurements with different hydraulic conditions: the histograms do not make a discrimination between the flow measurement in lower and higher time steps in an experiment.

The characteristic parameters of the eddies over depth inside the filter layer are given in Figure 4.20. Again, the outliers were excluded and histograms of the characteristic time and length scale of the remained measurements are made. In this figure, we see that the timescale of the vortices do not decrease over depth and is widely spread. On average, the timescale is 0.11 s, which is higher than the average timescale of the vortices in the free flow. This is due to the lower (pore) velocities inside the filter layer. When multiplied by the time-average pore velocities, we see smaller lengths of the eddies compared to eddies in the free flow. This indicates that the vortices are smaller inside the filter layer. The maximum length scale is 0.02 m. Again, it is important to note these histograms shows the average eddy size of all experiments. In each measurement, also larger and smaller eddies were present, but could not be calculated separately. Subsequently, the histograms do not make a discrimination between the flow measurement in lower and higher time steps in an experiment, in which the flow conditions differed.

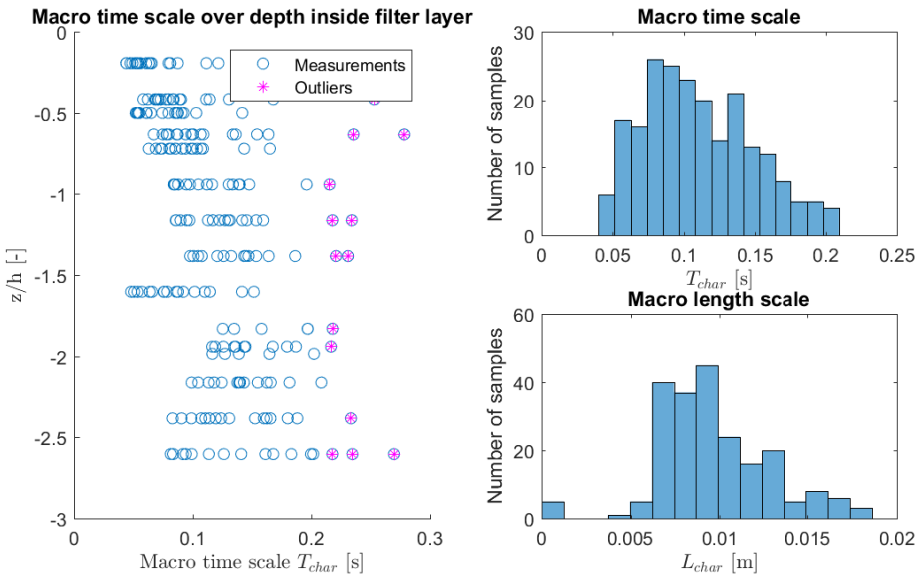

Figure 4.20: Characteristic time and length scale of the vortices in the filter.

In a granular filter, the low frequently flow fluctuations caused by the turbulence vortexes in the flow above the filter layer are able to lift the grains in the base layer. Due to the dynamic bed-pressures, the bed particles under the filter layer can be lifted under pressure and transported by

the mean flow (winnowing). In granular open filters, the energy of the eddy is simply too low to move the particles when the eddy is smaller than the particle size (Section 2.4.6).

We saw that the length scale of the vortices is in an order of a few centimetres. This is in the order of the diameter of the log. So, if you have grains of the order of a few centimetres, the fluctuating pressure gradient over the pores could lead to winnowing. In this study, this is less relevant, since we have long voids (in the order of the length of a log). The void of the logs in the filter layer is per unit length longer than the grain size. The void size in the cross-section (x,z-direction) is in the same order of the log. However, the void size in the longitudinal direction is much more, resulting in different flow types in the void. Additionally, in Section 5, it is emphasised that erosion is predominantly caused due to stagnation and plane jet scour at the front of the log. Therefore, the effect of dynamic bed-pressure and fluctuation is of minor importance and not further considered in this research.

5 Results erosion measurements

In this chapter, the results of the erosion measurements are provided. This is based on visual observations (5.1) and data obtained by the laser (5.2). Moreover, the moment of erosion is regarded (5.3).

5.1 Visual observations

During the experiments, visual observations were done by looking through the glass at the side of the flume and from above the filter in the water column. Before showing the results, it should be noted that at the side of the flume wall effects occur. The porosity of the filter layer near the wall is higher than in the middle of the channel (see Section 3.4.1). Due to a higher porosity near the wall, erosion will take place at lower velocities than in the middle of the channel. In addition, on should be aware that the erosion process which occurs at the side of the flume may not be present in the middle of the channel, since a lower porosity might lead to different flow characteristics and erosion processes.

To describe the erosion process, the flow properties during low flow velocities and high flow velocities will be described. In this section, the visual observations of experiment R05 are used to describe the process. The other experiments showed similar results.

Figure 5.1 and 5.2 shows the filter layer and sand bed from both sides of the flume. The lower flow velocities in the filter layer with respect to the free flow above the filter is clearly visible by means of a dye. Figure 5.1 shows the flow behind (downstream) the logs of layer 1 and Figure 5.2 shows the flow in front (upstream) the logs of layer 1. In both figures, the second layer of logs it is the opposite.

The penetration of the flow into the filter layer differs in both figures. Behind the log, the water penetrates gradually inside the filter layer (Figure 5.1). However, in front of a log, the flow penetrates faster into the filter (Figure 5.2).

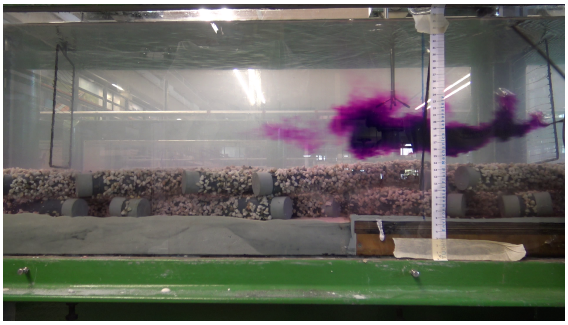

(a) $t = t_0$

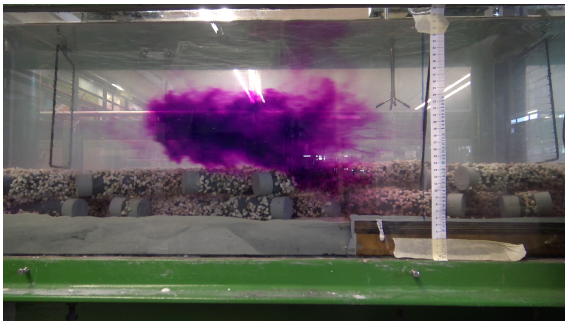

(b) $t = t_0 + \Delta t$

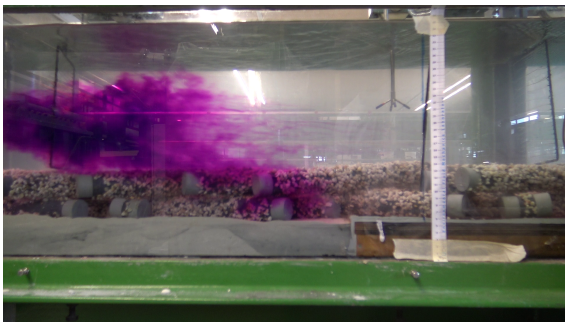

(c) $t = t_0 + 2\Delta t$

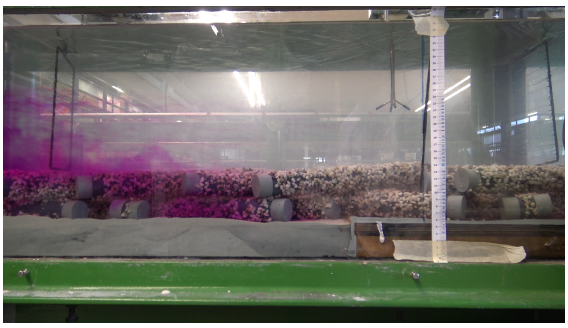

(d) $t = t_0 + 3\Delta t$

Figure 5.1: Left side view flow process of the flow development in the filter layer.

(a) $t = t_0$

(b) $t = t_0 + \Delta t$

(c) $t = t_0 + 2\Delta t$

(d) $t = t_0 + 3\Delta t$

Figure 5.2: Right side view flow process of the flow development in the filter layer.

The flow process in front of a log is presented in detail in Figure 5.3 by means of dye. This is a continuous flow and is forced by the geometry of the logs. The dye approaches the front of a log (Figure 5.3a). Due to the presence of the log, stagnation is present in front of the log. Stagnation in front of the causes a hydraulic pressure in front of the log, see Figure 5.4. This hydraulic

pressure induces a flow to the edge of the log. This results in a downward flow in front of the log, which acts more or less as a vertical jet flow (Figure 5.3b) [Schiereck, 2016]. This jet flow initiates erosion. When the erosion hole has appeared, the circulating current can also be found in the scour hole (Figure 5.3c). This vortex is carried along with the flow and transport the sediment further downstream. Downstream this process the flow velocity reduces and sedimentation occurs (Figure 5.3d). If the velocities in the filter are low, sedimentation also occurs upstream the front of the log, since the jet flow is stronger than the main flow velocity. Note that the scour caused by stagnation is only possible when no log is present under the front of the considered log. If a log of the layer below is present, the vertical jet flow is blocked by the log in the layer below. The vertical jet flow is able to lift some particles in such a way that the grains go into suspension. This also occurs when the sedimentation dune downstream the vertical jet flow becomes too large. The top of the dune may reach the depth in the filter where the critical velocity of the sand is present. In that case, the sand grains go into suspension.

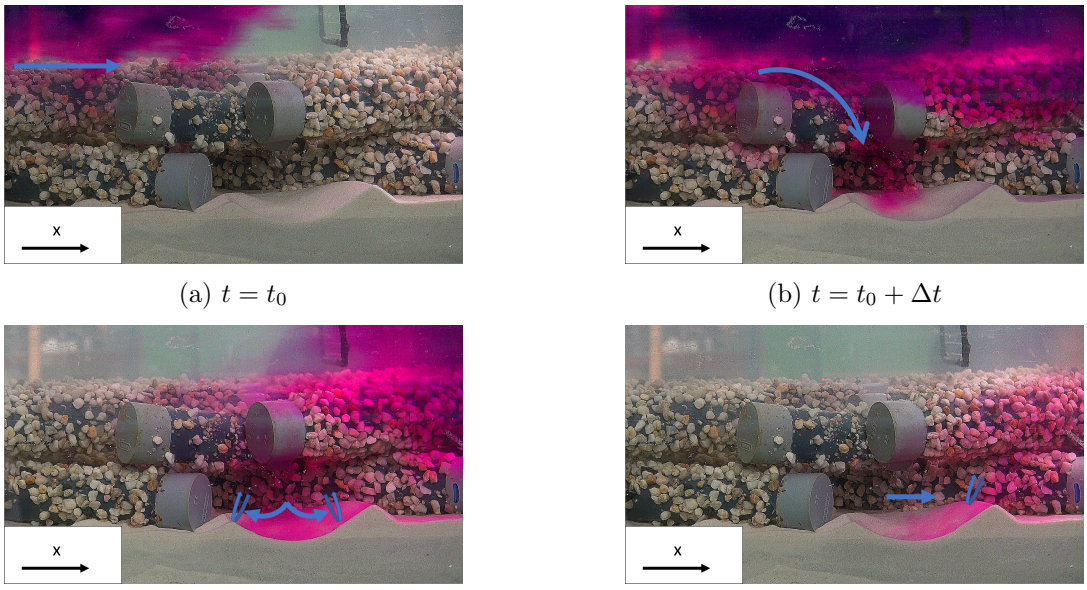

(a) $t = t_0$ (b) $t = t_0 + \Delta t$

(c) $t = t_0 + 2 * \Delta t$ (d) $t = t_0 + 3 * \Delta t$

Figure 5.3: Detail of the vertical jet flow caused by the stagnation in front of the log.

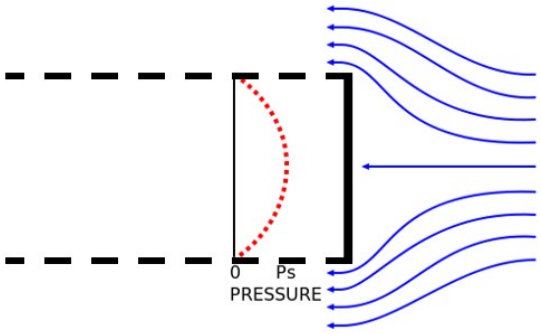

Figure 5.4: Hydraulic pressure caused by stagnation of the flow in front of a log.

When increasing the flow velocity, the pier scour effect increases. This means that the scour hole depth caused by the vertical jet flow increases as well. At a certain (pore) velocity, the second layer of logs introduces a pier scour effect as well, see Figure 5.5.

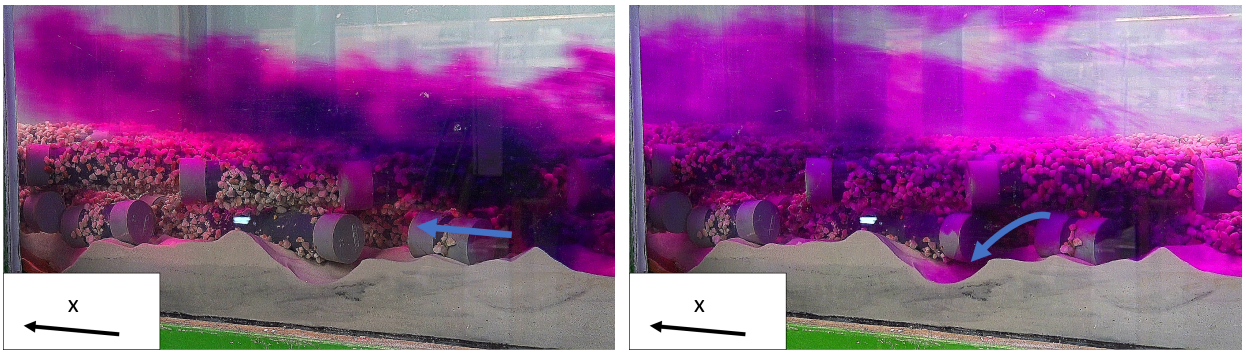

Figure 5.5: The vertical jet flow caused by stagnation of the log in the second layer.

When looking from above, it is clearly visible that the flow inside the filter layer follows the direction of the logs. Figure 5.6 shows the flow inside the filter layer. The dye was injected at the right side of the flume. The logs 'pushed' the water to the left side of the flume over the x-direction, due to the orientation of the logs. At the end of this small created channel, the vertical jet flow is present. The water flowing into this small channel is also present in the second layer. However, the scour caused by stagnation in the second layer of logs is not present in this figure, because of the reduced flow speed over depth in the filter layer.

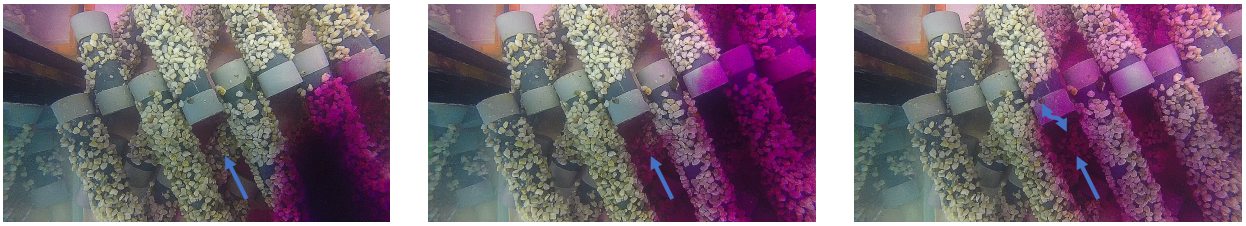

Figure 5.6: Direction of water flow in filter layer.

Behind (downstream) a log, the flow speeds are very low due to the presence of the log. Above the log higher flow velocities are present, which causes an eddy behind the log. Figure 5.7 shows the eddy behind the logs by means of dye over time. Over time, the dye is still present behind the log, whereas at other locations inside the filter layer the dye is transported further downstream. This indicates that a vertical vortex is present behind a log.

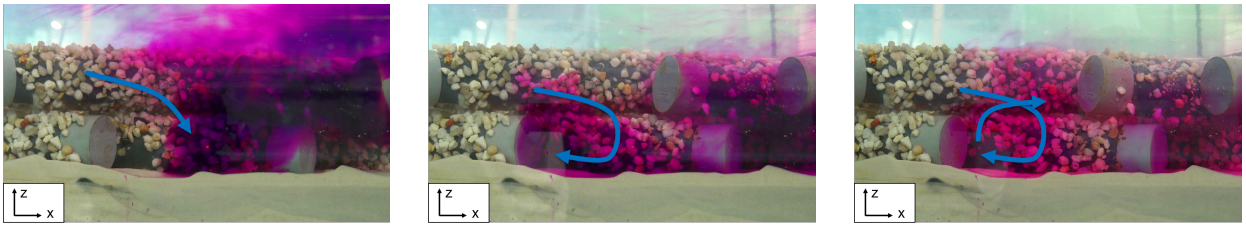

Figure 5.7: Vortex behind (downstream) a log caused by higher flow velocity above the log than behind the log

5.2 Laser

The visual observation of the flow in the previous section describes the flow inside the filter layer. Note that these visualisations were done at the side of the flume and from above the filter. It might be possible that the erosion processes in the middle of the channel differ. Therefore, a laser is used, which measures the bed profile and filter layer, see Section 3.4.3.

The measured bed is given in Figure 5.8. In total a region of 190 by 30 cm, in x- and y-direction respectively, is measured with respect to the bottom of the flume, see Section 3.4.3. For all figures considered in this section, the applied flow is from left to right. The sand bed is present in between $x = 100$ cm and $x = 180$ cm. At the start of the experiment, the sand bed is in general 5 cm. During an experiment, the level of this region changes. At $x = 265$ cm the filter stops and the false bottom increases, see Figure 3.2. The increase of the false bottom is depicted in yellow in Figure 5.8. The sediment trap is visible as well, depicted as a square in the middle of the channel and reach values down to the bottom of the flume (0 cm). For the erosion analysis, the region between 100 cm and 190 cm in the x-direction and between 5 cm and 35 cm in the y-direction is considered.

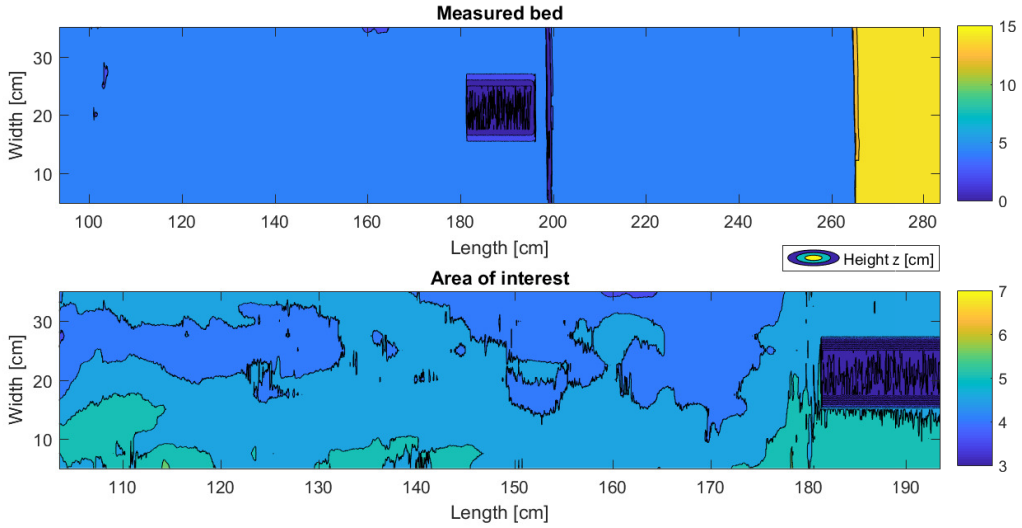

Figure 5.8: Measured area (above) and area of interest for erosion measurements (below) of all experiments. This measured bed is at the start of experiment R05. The sand bed is position between $x = 100$ and $x = 180$ cm. In y-direction, only the region between $y = 5$ and $y = 35$ cm is measured.

In each experiment the bed profile was measured before the logs were placed and after the experiment has been executed. In addition, the levels of the logs in layer 1, layer 2 and layer 3 were measured before and after each experiment. All experiments showed similar results. Therefore, only one experiment is highlighted in this section, experiment R06. The bed profile before and after the experiment is depicted in figure 5.9. Subsequently, the difference between the measured bed at the begin and end of the experiment is depicted. The blue dark spots indicate erosion regions of the bed. The yellow regions indicate sedimentation regions.

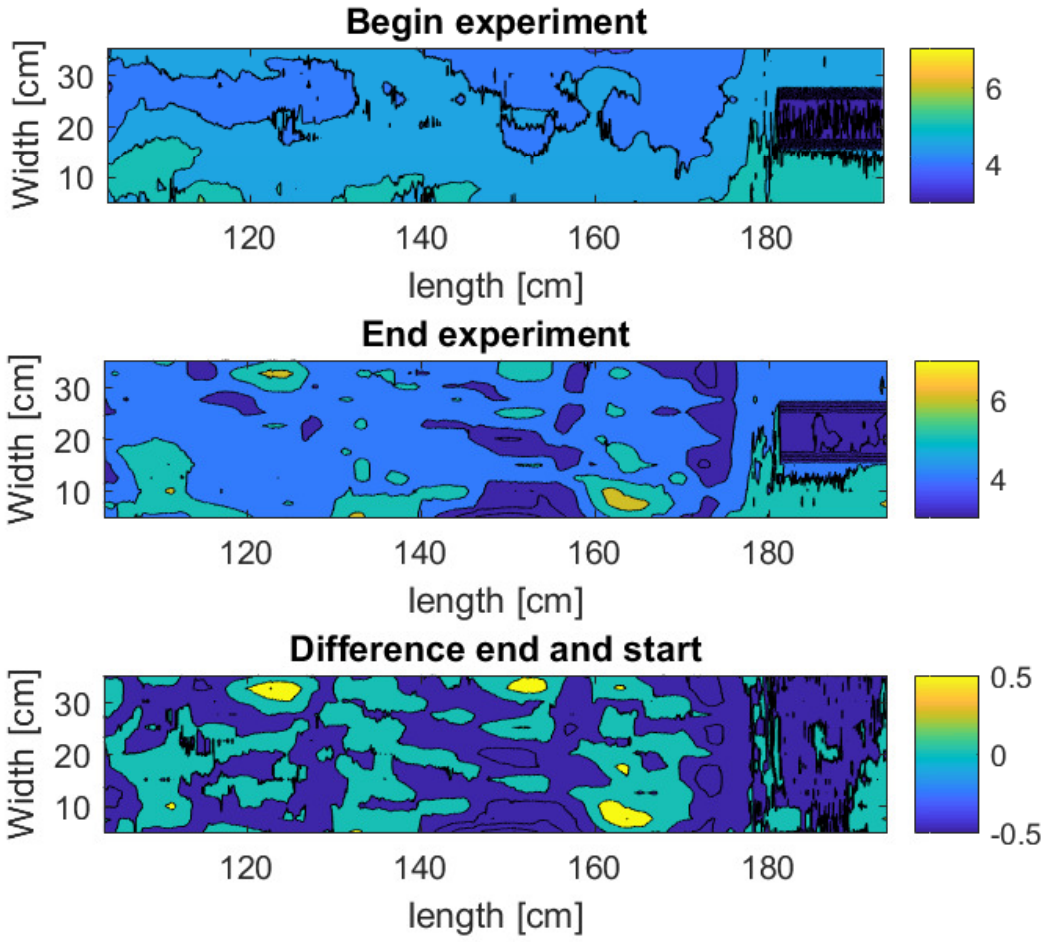

Figure 5.9: Measured bed before experiment R06 (up), after experiment (middle) and the difference between the bed levels before and after the experiment (down). The blue dark regions indicate lower bed levels, caused by erosion. Lighter (yellow) regions indicate sedimentation.

A threshold value of 0.5 cm is used to indicate which erosion regions erodes or sediments more than others. This is depicted in Figure 5.10. Regions which eroded more than 0.5 cm are depicted in blue. Regions which aggregates more than 0.5 cm are depicted in yellow. The blue regions are used to analyse the relationship between the eroded regions and the position of the logs.

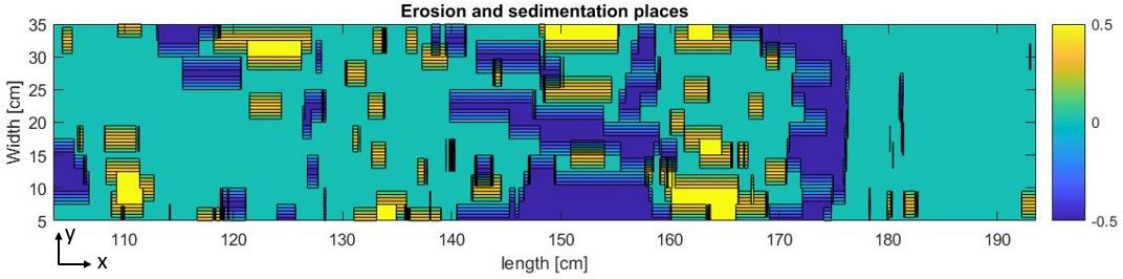

Figure 5.10: Erosion and sedimentation regions of experiment R06 which are higher than 0.5 cm. Blue regions indicate erosion and yellow regions indicate sedimentation.

The relation between the regions of signification erosion and the position of the logs of layer 1 and layer 2 are given in Figure 5.11 and Figure 5.12 respectively. In these figures, the located logs of the layer are transparently depicted in relation to the erosion and sedimentation regions of the difference between the start and the end of experiment R06 (Figure 5.10).

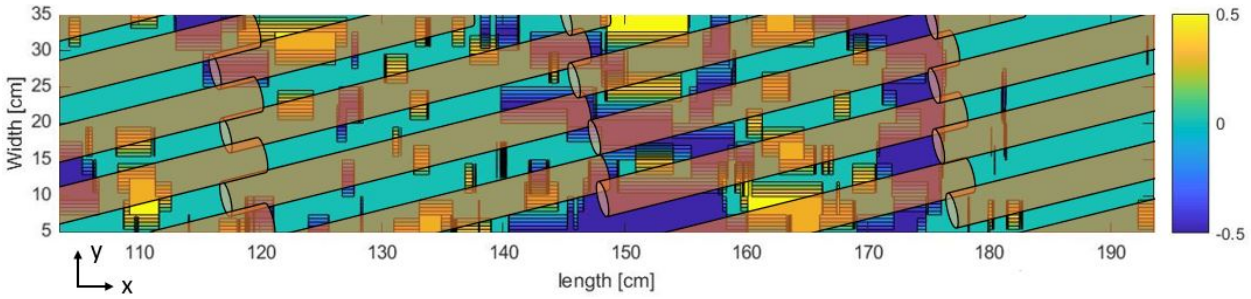

Figure 5.11: Erosion (blue) and sedimentation (yellow) regions of experiment R06 which are higher than 0.5 cm with the placed logs of layer 1 (brown). Signification erosion is in front of the logs of layer 1.

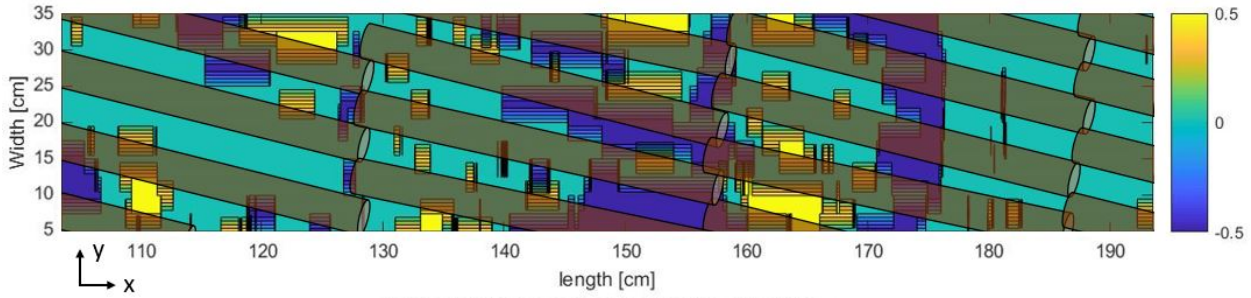

Figure 5.12: Erosion (blue) and sedimentation (yellow) regions of experiment R06 which are higher than 0.5 cm with the placed logs of layer 2 (brown). Signification erosion is present at $0.5 * L_{log}$ and in front of the logs of layer 2.

Figure 5.11 and Figure 5.12 shows:

- the largest erosion regions are present in front of the logs in layer 1 (Figure 5.11). In layer 2, this is located between and halfway two logs (Figure 5.12);
- erosion regions are also present in front of logs of layer 2, but are smaller than the erosion regions in front of the logs in layer 1.

From these observations, we concluded the following:

- the erosion regions in front of the logs of layer 1 are caused by the vertical jet flow as explained in Section 5.1 Figure 5.3;
- the scour caused by the vertical jet flow effect is also present in layer 2, but the effect is lower due to the lower pore velocities in this layer. We also saw this effect at the side of the flume in Figure 5.5;
- the erosion process which was present at the side of the flume also occur in the middle of the flume: scour caused by vertical jet flow due to stagnation in front of the log. In the middle of the flume, this occurred at higher velocities. Scour caused by vertical jet flow in layer 2 only occurred to a limited amount.

5.3 Erosion phase

During the experiments, the discharge was increased while the water level was emulated to be 20 cm. Every hour, the discharge was increased until the filter layer was not to able reduce the hydraulic load in such a way to prevent erosion of the base layer. During the experiments, the sediment was caught in the sediment trap if erosion was present. We define two stages of erosion this research: no erosion and start of erosion. All experiments showed a clear distinction between these two stages for each time step. The stages are described by means of the side view of the sediment trap in Figure 5.13. This figure shows the side view of the sediment trap at the end of each time step of experiment R05. The related flow characteristics of each time step of experiment R05 are given in Table 4.5. On the other side of the flume, a light shined towards the sediment trap in order to improve the sight in the sediment trap.

It is clearly visible that hardly any sediment is present in time step 1 to 5. The sediment which is caught by the sediment trap in this stage is due to initial effects. In time step 6, we saw a constant supply of sediment into the sediment trap. We conclude that this is the stage were erosion starts. A clear distinction between time step 5 and 6 is visible. We conclude, in the case of experiment R05, that time step 1 to 5 is in the stage of no erosion and time step 6 is in the stage of start of erosion.

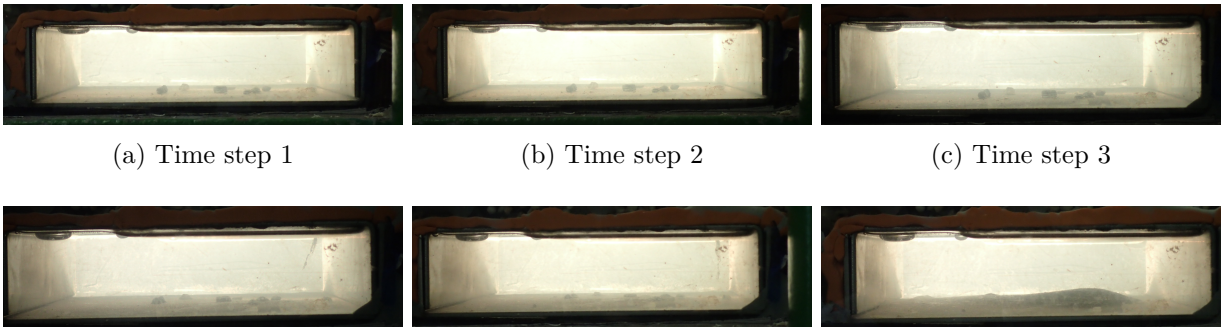

(a) Time step 1 (b) Time step 2 (c) Time step 3

(d) Time step 4 (e) Time step 5 (f) Time step 6

Figure 5.13: Side view of the sediment trap of experiment R05 for multiple time steps.

The method to determine which stage is present, Figure 5.13, is done for all experiments. The results are given in Table 5.1. Also, the critical gradient of the energy slope and depth-averaged flow velocity for the erosion stage is given. In experiment R08, the sediment at the side of the flume eroded in such a way that the filter layer became unstable, see Figure 5.14. The experiment was stopped in order to prevent damage to the ADV2, which was located inside the filter layer.

Table 5.1: Erosion stage of each time step of all experiments. A minus indicates the stage in which no erosion or only initial erosion is present. A plus indicates the stage in which erosion is present. In addition, the critical velocity and flow velocity at the last time step are given. Experiment R08 has not reached the stage of erosion, since the filter became unstable.

Experiment		R01	R02	R03	R04	R05	R06	R07	R08*	R09
t1		-	-	-	-	-	-	-	-	-
t2		-	-	-	-	-	-	-	-	-
t3		-	-	-	-	-	-	-	-	-
t4		-	-	-	-	-	-	-	-	-
t5		-	+	-	+	-	-	+	-	-
t6		-		-		+	+			+
t7		+		+						
layers	[-]	2	2	2	2	2	2	3	3	3
i_c	[‰]	2.44	3.61	1.99	3.27	2.56	8.50	5.90	8.20	8.20
$\overline{\overline{u_{loc3,c}}}$	[m/s]	0.68	0.69	0.69	0.60	0.66	0.70	0.77	0.75	0.80

Figure 5.14: Unstable filter layer at time step 5 of experiment R08. The experiment was stopped in order to prevent damage of the ADV2 inside the filter layer.

Table 5.1 shows that the critical gradient and critical depth-averaged flow velocity in a filter consisting of three layers are higher than critical gradient and critical depth-averaged flow of a filter consisting of two layers. Figure 5.15 shows the reason why. In this figure, the evaluation of the vertical jet, caused by the front of a log in layer 1, of experiment R07 time step 2, is elaborated. In this time step, the discharge (Q) was 50 l/s and depth-averaged flow velocity ($\overline{\overline{u_{loc6}}}$) is 0.63 m/s. This is at approximately the same hydraulic conditions in which the base layer in the middle of the flume in experiment R04 eroded.

At first, the flow approaches the front of the log in layer 1 (Figure 5.15a). Due to stagnation, a vertical jet flow is present (Figure 5.15b). When the flow is halfway the second layer, the flow caused by the vertical jet starts to diffuse due to the available space and constant flow velocity in the x-direction in the layer (Figure 5.15c). Thereafter, the fully diffused flow is carried along with the flow (Figure 5.15d).

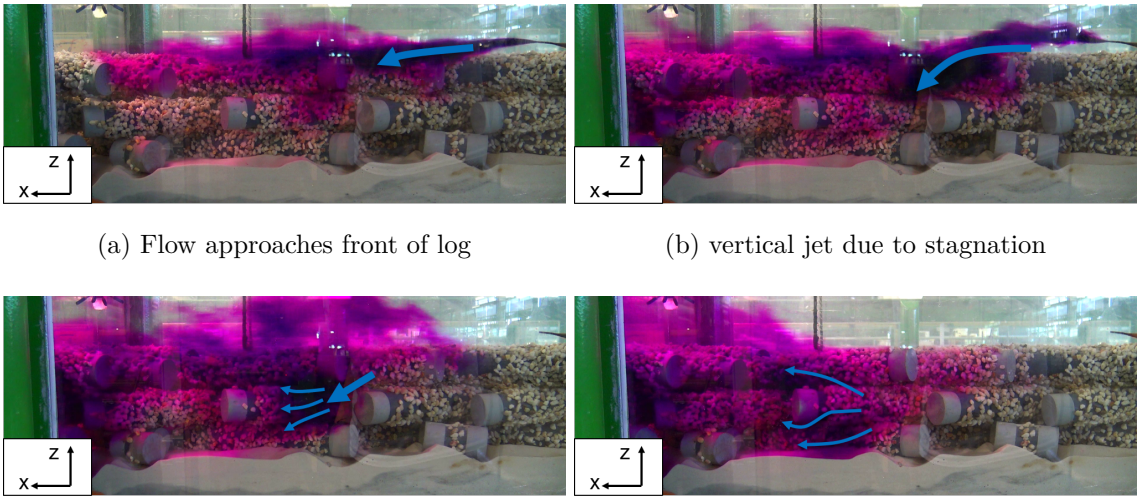

(a) Flow approaches front of log

(b) vertical jet due to stagnation

(c) Diffusion of flow in second layer

(d) Fully diffused flow

Figure 5.15: vertical jet of the log in layer 1 caused by stagnation of experiment R07 time step 2. In layer 2, the jet plane flow diffuses again, because of the space. The flow in layer 3 is hardly influenced by the vertical jet caused in front of the log in layer 1.

Figure 5.15 shows that the flow caused by the vertical jet of a log in layer 1 penetrates to a certain depth. During the flow conditions of the experiment in this figure, this is approximately at the transition between layer 2 and layer 3. Hence, in these conditions, no erosion of the base layer due to the vertical jet caused by a log in layer 1 was present. When we increased the discharge and average flow velocity over the filter structure, the penetration of the vertical jet also increased. At a certain flow velocity above the filter, the penetration of the jet flow caused by the log in layer 1 does reach the base layer. In that case, erosion occurred. Therefore, higher flow velocities were needed in experiment R07, R08 and R09 to cause erosion of the base layer due to vertical jet scour. We conclude that the penetration depth due to the vertical jet flow increases when the velocity over the filter structure increases. From the observations, we also conclude that the influence of vertical jet caused by stagnation in front of the log in layer 1 is the dominant process which leads to erosion of the base layer.

6 Discussion

This research focused on the hydraulic load reduction as the function of depth inside a filter consisting of logs. The effect of introducing more layers, i.e. increasing the filter layer thickness, was researched. In addition, the erosion processes and flow characteristics around a log were investigated by use of a dye. This chapter describes the way how the results should be interpreted and shows the shortcomings of the results. Subsequently, the link between the scale model and prototype is made.

6.1 Interpretation of the results

6.1.1 Flow measurements above the filter layer

A perfect comparison between the flow conditions above the filter and inside the filter could be made when the flow velocities were measured at the same location (in the x-direction). Since the ADV2 device was placed inside the filter layer at location 3 and could not be moved during the experiments, the flow measurements above the filter layer were done at location 6. In this research, we concluded that the measured flow velocities in location 6 are also representative of the flow velocities at location 3, see Section 4.1. This conclusion is based on experiment R04 and R05 respectively. It is consistent with the other measurements at location 6. During this research, there were no indications that the flow characteristics differ between the locations.

At the transition between the free flow and the filter layer, the ratio between the turbulent kinetic energy and the shear stress is 3.51 (Figure 4.9). In granular open filter, this ratio is similar, 3.2 (Figure 2.11). From this, we conclude that the turbulent kinetic energy between the free flow and the filter layer in case of logs is similar to the turbulent kinetic energy of granular open filters.

6.1.2 Geometrical adjustments for flow measurements inside the filter

In this research, the flow velocities were measured in the middle and between two logs, see Figure 6.1. In the first set of experiments, the flow measurements were done in the middle and between two logs of layer 1. In the second set of experiments, the flow measurements were done in the middle and between two logs of layer 2. In the third set of experiments, the flow measurements were done in the middle and between two logs of layer 3. As depicted in the figure, the layer above or under the considered measured layer has formed a new row, see Section 3.4.1.

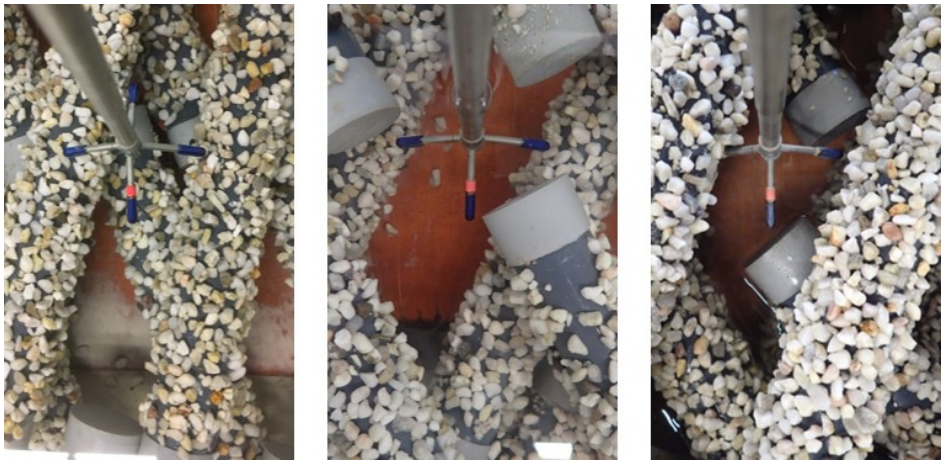

Figure 6.1: Position of the ADV1 inside the filter layer in first set of experiment (left), second set of experiments (middle) and third set of experiments (right).

In order to place ADV2 inside the filter layer, additional space was created. Therefore, the geometry around the ADV2 slightly differed from the original geometry explained in Section 3.4.1, see Figure 6.2. The space between two logs was slightly higher than one time the diameter of a log. If this additional space was not created, we were not able to perform measurements inside the filter layer. In this research, it was assumed that the local adjusted geometry had minor effects on the measurements inside the filter layer. In reality however, it does have an influence on the measured flow velocity, since the porosity is slightly higher at this location.

Figure 6.2: Created additional space for the ADV2 device in experiment R05: the distance between two logs is slightly higher than the normal geometry. The place of the ADV2 is depicted by the red circle.

6.1.3 Appropriateness flow measurements inside the filter layer

The measured pore flow velocity at the moment of erosion of each experiment is showed in Figure 6.3. The figure also shows the pore flow velocity relative to the critical flow velocity of the sand grains in the base layer ($u_c = 0.14$ m/s), see Table 3.1. In layer 1, the pore flow velocities are approximately equal to the critical flow velocity. This also holds for the region between the transition

of layer 1 and 2 to halfway layer 2. However, from the transition between layer 2 and layer 3 and deeper, the pore flow velocity is approximately 0.6 times the critical flow velocity.

Figure 6.3 indicates that from the transition between layer 2 and 3 and deeper, the critical flow is never exceeded. This means that the flow velocities in this region do not cause erosion. However, in these conditions, we saw constant supply of sediment in the sediment trap and stopped the experiment. When we analysed the data obtained from the laser, we saw significant erosion in front of the logs, see Section 5.2. This emphasises that the erosion is mainly caused by the vertical jet flow in front of the log caused by stagnation. One should be aware that the measured flow velocities in Chapter 4.3 does not provide the flow velocities in front of the log. So these measurements are not the representative values for causing erosion. It only indicates the hydraulic load reduction in the middle and between two logs. In order to obtain the flow conditions which causes erosion, additional research regarding the flow properties in front of the log should be carried out. The flow properties in front of the log are lacking in this research.

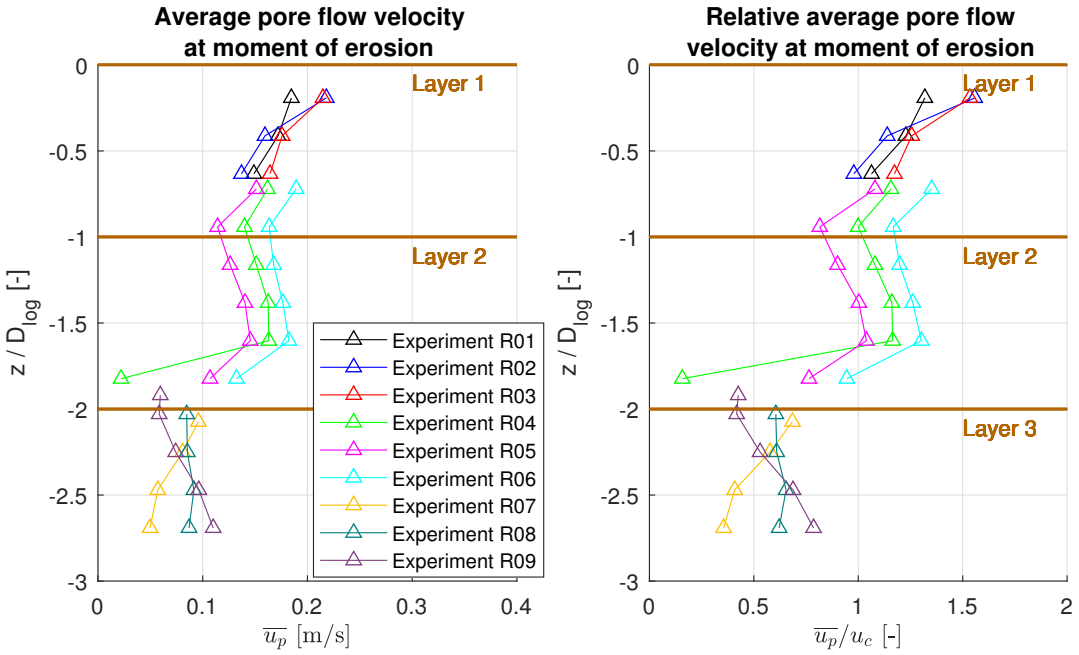

Figure 6.3: The time-averaged pore flow velocity in the last time step of each experiment (left). This time-averaged pore flow velocity is compared to the critical flow velocity of the sand grains in the base layer (right).

6.1.4 Hydraulic load reduction over depth inside filter layer

Figure 4.14 and Figure 4.16 showed the pore flow velocity and the turbulent kinetic energy at each considered depth into detail. From these figures, we concluded that the hydraulic load does not decrease exponentially over depth.

In previous granular open studies, the distribution of the turbulent kinetic energy in the filter layer is scaled to the dimension of the grains of the filter layer, which resulted in an exponential decrease (Figure 2.11 and Figure 2.12). The detail around a grain itself is not considered. It might be possible that the profile distributions change when we scale the pore flow velocity and turbulent kinetic energy to the dimension of the log.

Figure 6.4 shows the distribution of the pore flow velocity and turbulent kinetic energy when scaled to the dimension (diameter) of the log. In this figure, the average pore flow velocity and turbulent kinetic energy of each layer are depicted by a red solid point. As shown in the figure, the decrease of the pore flow velocity and turbulent kinetic energy (solid red line) is not exactly exponential (red dashed line). However, we see that the reduction of the turbulent kinetic energy in the first layer does follow the exponential decay. The bump of the hydraulic load in the second layer is caused by the structured layering of the logs. In granular open filters, the grains fit each other resulting in an exponential reduction due to the shape of the grains, whereas this is not the case in logs. The way how the filter layer is structured has an influence on the hydraulic load reduction.

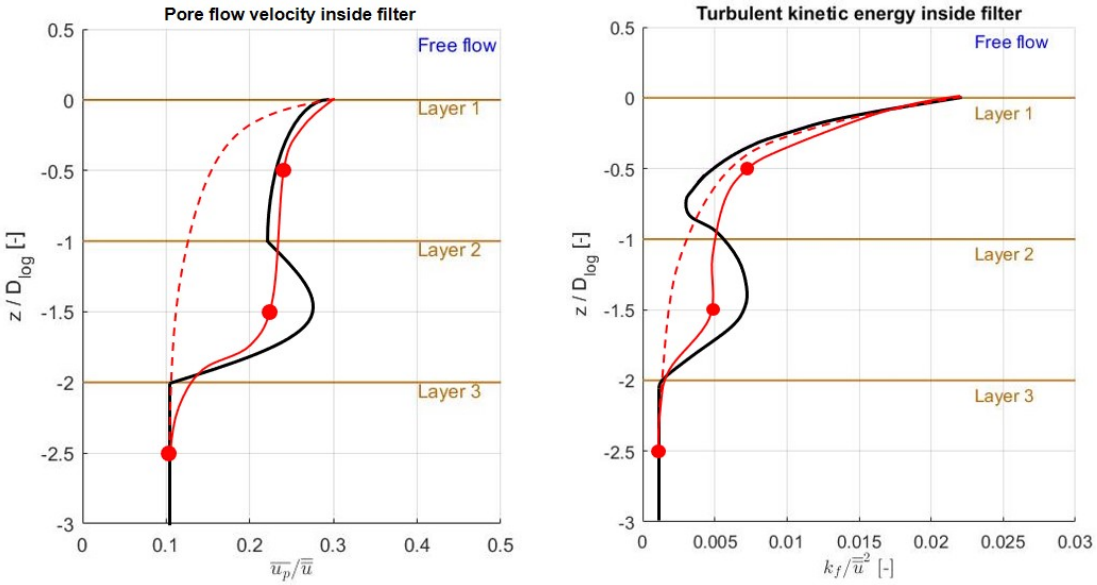

(a) Pore flow velocity (b) Turbulent kinetic energy

Figure 6.4: Schematically distribution of the pore flow velocity and filter turbulent kinetic energy over depth inside the filter layer when scaled to the dimension of the log. The dashed red line represents an exponential decrease, whereas the solid red line represents the real situation when the pore flow velocity or turbulent kinetic energy is averaged over the diameter of a log.

6.1.5 Erosion process

From the observations (Section 5.1) we saw that the flow is very anisotropic: the flow conditions in front, halfway and behind the log differs. The flow conditions are not equal inside the filter layer and vary locally. Erosion takes place in front of a log, caused by the vertical jet flow due to stagnation, see Figure 6.5. The eroded sediment is transported downstream by the mean flow in the filter by winnowing. Behind the log, a vertical eddy is present because the flow above the log is higher than behind the log.

While in the granular open filter the transport of the sediment is a diffusive process, the transport in the case of logs is an advective process. The flow is localised and the erosion depends on the geometry of the log. There is an entrainment of momentum in the bed, causing the erosion in front of the log. This is not present in granular open filters.

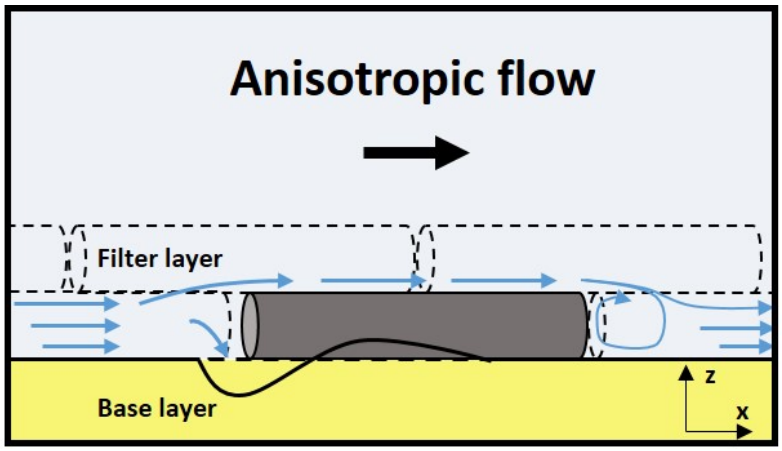

Figure 6.5: Schematic sketch of the flow around a log from the side. In front of the log (upstream), vertical jet is present due to stagnation. Behind the log (downstream) a eddy is present, because the flow above the log is higher than behind the log.

In this research, the experiments were stopped when a constant supply of sediment into the sediment trap was present. The question arises whether, if you have significant erosion, this procedure stops at a certain point. It is interesting to know what the erosion processes will be on the long term. Is the erosion phase defined in this research only an initial effect? Or will the logs fail if you continue with the same hydraulic conditions? In this research, these questions cannot be answered. Additional experiments should be carried out in which the time span of each time step is increased in order to provide an answer.

6.1.6 Characteristic length vortices inside the filter layer

The length of the vortices inside the filter layer are calculated by means of the Taylor hypothesis. However, this hypothesis only holds when the eddy does not change during the passage time and when the fluctuation caused by the eddy does not affect the transport velocity significantly [Bailly and Comte-Bellot, 2015]. In other words, the flow velocities of the fluctuations should be much lower than the mean flow fluctuation ($u'_p << \overline{u}$). The flow velocities in the filter layer are quite low, so we should question whether this assumption is valid. The length scales of the vortices inside the filter layer is in the order of 1.5 cm. If the grains were in the order of a few centimeters, the fluctuating pressure gradient caused by the eddy may lead to winnowing. In this study, the flow caused by the eddies is not relevant, since the void is in the order of the length of one log (33 cm). Since the vortices do not lead to a dominant erosion process, this is not further considered this research.

6.1.7 Influence log roughness

In order to ensure a hydraulic rough flow regime gravel was glued to the PVC tubes. The diameter and roughness of the logs were 4.54 cm and 1.91 mm respectively.

The results showed that, assuming the water level is 20 cm, the roughness height (k_r) is 7.02 mm. In general, for a flat bed in a flume experiment, $k_r = 3d_{n50}$ is used [Schiereck, 2016]. If we follow this, the roughness height is more affected by the roughness of the log ($k_r/k_{log} = 3.67$) than the diameter of the log ($k_r/D_{log} = 0.15$). Considering this approach, you might say the log roughness is important for the flow characteristics in the water column.

However, if we reflect the influence of the log roughness on the stability of the base layer, the log roughness is of minor importance. We saw that the erosion is caused by stagnation at the front of the log. The presence of the log is causing an other type of flow. This vertical jet flow is influenced by the front diameter of the log, not by the influence of the log roughness. The vertical jet flow caused by the front of the log could be reduced by designing a more streamlined front. In that case, erosion will be suppressed.

6.2 Model versus prototype

6.2.1 Scaling

In this research, the Froude scale (1:10) is enhanced in order to ensure the same gravitational effects as in prototype. To ensure the sediment mobility, the critical Shields number should be equal in both prototype and model ($n_{\psi_c} = 1$). Therefore, Equation 6.1 must hold. Since we do not know what the friction coefficient in the prototype will be, we assume that this is equal to the friction coefficient in the model ($n_{c_f} = 1$). By enhancing the Froude scale ($n_h = \sqrt{10}$) and Shields scale together, the scale of the diameter of the base layer should be ($n_{d_{50b}} =$) 10, see Equation 6.1. This means that the grain size of the scale model should be 30 µm. Since no particles lower than 100 µm could be used, see Section 3.2.1, it is not possible to enhance the Froude and Shields scale together.

$$n_{\psi_c} = \frac{n_{c_f} n_{\overline{\overline{u}}}^2}{n_{\rho_s - \rho_w} n_{d_{50b}}} = 1 \quad \Rightarrow \quad n_{d_{50b}} = \frac{n_{\overline{\overline{u}}}^2}{n_{c_f}} = 10 \tag{6.1}$$

The used particles of the base layer in the model are 140 µm, resulting in a base grains scale of (n_{d50b}=) 2.14. If we enhance the mobility parameter shields this lead to a velocity scale of ($n_{\overline{\overline{u}}}$=) 1.46, see Equation 6.1.

$$n_{\psi_c} = \frac{n_{c_f} n_{\overline{\overline{u}}}^2}{n_{\rho_s - \rho_w} n_{d_{50b}}} = 1 \quad \Rightarrow \quad n_{\overline{\overline{u}}}^2 = n_{d_{50b}} n_{c_f} \quad \Rightarrow \quad n_{\overline{\overline{u}}} = \sqrt{n_{d_{50b}}} = \sqrt{2.14} = 1.46 \tag{6.2}$$

The critical depth-averaged flow velocity of the model is calculated into the critical depth-averaged flow velocity of the prototype in Table 6.1. As given in the table, a filter consisting of logs could prevent erosion of the underlying subsoil up to depth-averaged flow velocity of 1 m/s, excluding experiment R04. Hence, if the depth average flow velocity of a river is lower than 1 m/s, a log filter is a type of bottom protection that could be used as bottom protection against erosion of the base layer. If a depth-averaged values of 2 m/s has to be obtained, the velocity scale should be $n_{\overline{\overline{u}}} = \sqrt{10}$, resulting in a prototype base diameter of ($d_{50b} =$) 1400 µm.

Table 6.1: Critical gradient and critical depth-averaged velocity of the model and the calculated prototype.

Experiment			R01	R02	R03	R04	R05	R06	R07	R08*	R09
	layers	[-]	2	2	2	2	2	2	3	3	3
	i_c	[‰]	2.44	3.61	1.99	3.27	2.56	8.50	5.90	8.20	8.20
Model	$\overline{\overline{u_{loc3,c}}}$	[m/s]	0.68	0.69	0.69	0.60	0.66	0.70	0.77	0.75	0.80
Prototype	$\overline{\overline{u_{loc3,c}}}$	[m/s]	0.99	1.00	1.00	0.88	0.96	1.02	1.12	1.10	1.17

6.2.2 Number of layers

Figure 4.14 and Figure 4.16 showed that at least two layers are needed in order to ensure a significant decrease of the pore flow velocity and turbulent kinetic energy. Beneath two layers, the pore flow velocity and turbulent kinetic energy are dominantly caused by the influence of the energy slope (pressure gradient). This flow is always present, regardless how thick the filter layer is. From this research, we conclude that the minimum required thickness of a filter layer consisting of logs is two layer. Adding more than two layers will not lead to further reduction of the pore flow velocity or turbulent kinetic energy.

However, one should keep in mind that the experiments were done in perfect conditions: the bed was flat, the geometry of the logs was structured and the logs hardly move during the experiments. In practical, the bed is not flat and the logs are more randomly placed. The range of the porosity at each location vary, resulting in local variation of flow velocity higher and turbulent kinetic energy.

In addition, we see a strong gradient in both the pore flow velocity and turbulent kinetic energy distribution slightly above the transition between layer 2 and layer 3, see Figure 6.4. So, when the grains of the base layer are located in this region, erosion will occur. This, in combination with the imperfect conditions in reality, could result in erosion when a two-layered log filter is placed in rivers.

So, on practical considerations, it is advised to create an additional, third, layer. This is advised in order to reduce the risk that the grains of the base layer is located in the region where the influence of the flow over the filter construction is still present.

6.2.3 Aspect ratio

In this research, it was difficult to enhance the same length scale for the dimensions of the log. The scale of the diameter of the log is ($n_{D_{log}}$ =) 11.0 whereas the scale of the length of the log is ($n_{L_{log}}$) = 15.2. In prototype, the aspect ratio (L/D) ratio is 10, whereas in the model the diameter is 7.3. The logs are distorted, leading to a scale effect: $n_{L/D} = 1.38$.

The effect of the erosion due to vertical jet flow depends on stagnation in front of the log. If the area of stagnation increases, we expect the pressure build up (in Figure 6.4) to increase as well. Hence, the downflow is expected to increase when a broader object halts the flow [Schiereck, 2016]. So, we expect that the effect of vertical jet flow increases when the aspect ratio decreases. One should keep in mind that aspect ratio's up to 1 cannot be considered as a log. In that case, the diameter is equal to the length, which acts more like a grain than a log.

In this research, the scale of the aspect ratio was slightly higher than 1, indicating that the aspect ratio in the model is lower than the aspect ratio in the prototype. The effect due to stagnation is, therefore, larger than in prototype, resulting in erosion at lower flow velocities. Since the length of the logs could vary in reality, the effect of this ratio is not further considered. In reality, the logs are not identical: the aspect ratio differs per log. It is interesting to know which aspect ratio leads to the same effects. When the aspect ratio increases, the stagnation caused by the front of the log decreases, since the diameter of the log decreases. At a certain ratio, it might be possible that the main erosion is not caused by the vertical jet flow anymore.

The shape in front of the log is important as well, since this causes the pressure build-up in front of the log. If the front of the log is designed in a more streamlined way, the pressure build up will be

less, resulting in a lower effect of the vertical jet flow caused by stagnation. However, one should keep the additional construction costs, which are needed to reshape the front of the logs, in mind. In addition, the anisotropic flow caused by the log is a given entity, it should not be avoided.

6.2.4 Geometry and porosity

The geometry of the filter layer is kept constant during this research. The filter layer consist of structured layers, see Section 3.4.1. Although this structure was mainly enhanced, the position of some logs slightly differed from the structured, due to wall effects or for example creating additional space for the ADV2 device inside the filter layer. At the side of the flume, the logs were modified in such a way that it fits inside the flume with minimal wall effects. However, at some locations at the side of the flume, it was not possible to place a log since the space at those locations were simply too small. This resulted in a higher porosity at the side of the flume with respect to the porosity in the middle of the flume. When looking at the results, one should bear in mind that the porosity at the side of the flume is higher than in the middle of the flume.

Since only one type of geometry is used, we considered only one porosity value. Therefore, initially, it was not possible to quantify the effect of porosity. However, we describe the effect of porosity by the consistent behaviour of all experiments. We saw the erosion of the base layer at the side of the flume at lower flow velocities than in the middle of the flume. This is due to the higher porosity at the side of the flume. When the filter layer is more densely packed (in the middle of the flume), the vertical jet flow caused by the log of layer 1 is better dissipated or blocked than when the filter layer is more loosely packed (at the side of the flume). From this, we conclude that the porosity is an important variable in a log filter. So, when the porosity increases, the vertical jet flow is less dissipated, resulting in more erosion.

In reality, the geometry of the logs is not well structured. Imagine a bunch of logs which are scattering in dimensions and are not ordered placed. The way how the logs are packed determine the amount of dissipation of the vertical jet flow caused by stagnation. If the logs are densely packed, the plane jet flow will be dissipated by the presence of other logs and less erosion will take place. If the logs are loosely packed, the effect of the plane jet flow will be less dissipated, resulting in more erosion. The structured layering of the logs in this research may induce erosion, because of the regular spacing in between the logs. If the logs are more randomly placed, the vertical jet plane flow will be more dissipated, resulting in less erosion. Therefore, it is recommended to use a mixture of trees, instead of placing them in a structured way.

It is interesting to know which porosity values leads to the same erosion effects and at which porosity leads to other erosion processes. How dense should the logs be packed in order to ensure that the erosion caused by stagnation and vertical jet not occur? Additional experiments should be carried out, which describe the influence of the porosity on the stability of the base layer.

The same holds for other types of geometry. In all experiments, the geometry of the logs was identical and chosen arbitrary on some considerations, Section 3.4.1. Since we only considered one geometry, we are not able to describe whether the same effects occur when another geometry is used. Additional experiments in which the geometry is varied should provide an insight into whether the same flow characteristics and erosion processes are present as in this thesis.

6.2.5 Pressure gradient measurements

The pressure gradient of the water over the filter was determined by measuring the water levels manually. During low flow velocities, it was not difficult to measure the water levels. However, when the discharge increased, the water surface got disturbed by the devices inside the flume, resulting in small waves. Measuring the water level in these conditions was difficult and resulted in inaccurate measurements of the water level. Therefore, the measured gradient is not always representing the real acting gradient. This has an effect on the calculated pore velocity and turbulent kinetic energy caused by the energy slope since these values depend on the gradient. Normally, the gradient is also used to check the friction velocity. However, in this research, this is done by using the flow measurements and its logarithmic profile. For future studies in which the gradient are water level should be measured accurately, it is advised to use a laser or an ultrasonic device to determine the water levels instead of measuring it manually.

7 Conclusions and Recommendations

In this thesis, an elementary insight of the hydraulic load reduction as a function of depth in the filter layer consisting of logs is presented. The research focused on the following main research question:

How does the hydraulic load as a function of depth in the filter layer, consisting of logs, behave and what is the influence on the underlying soil?

With the following sub-questions:

1. What is the minimum required thickness, i.e. the number of layers, of the filter layer in order to ensure the stability of the base layer to prevent erosion of the underlying soil
2. What type of erosion is a log filter inducing on the base layer?
3. What are the differences between the hydraulic load reduction in a log filter and a granular open filter?
4. Which parameters and variables are important for describing the load reduction?

In Section 7.1 the questions regarding this thesis are answered. In addition, recommendations for further research on this topic are presented in Section 7.2.

7.1 Conclusions

The findings regarding the sub-question "*What is the minimum required thickness, i.e. the number of layers, of the filter layer in order to ensure the stability of the base layer to prevent erosion of the underlying soil?*" are largely described by means of Figure 4.14 and Figure 4.16:

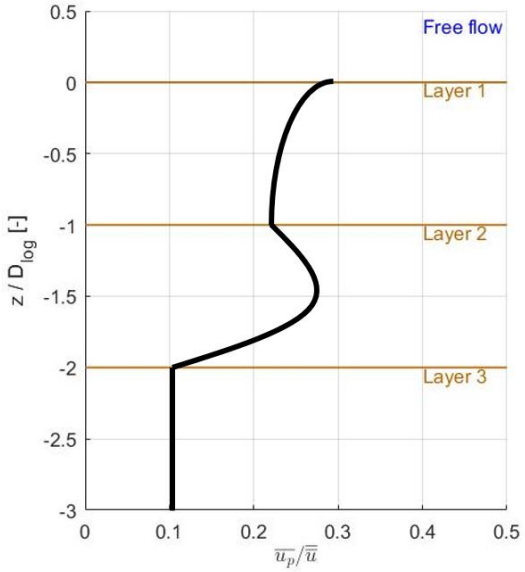

Figure 4.14: Schematic distribution of the pore velocity over depth inside the filter layer.

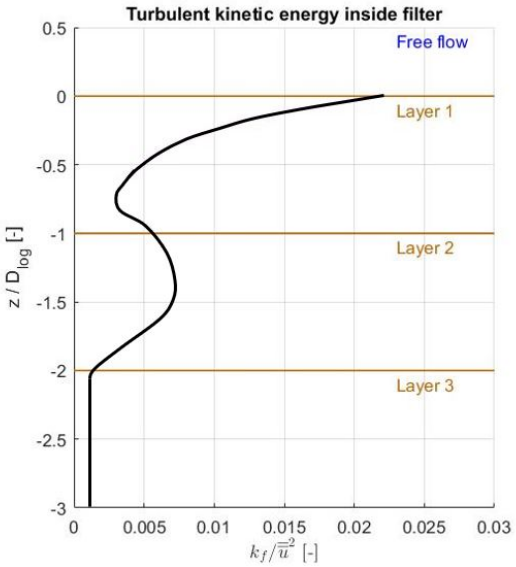

Figure 4.16: Schematic distribution of the filter turbulent kinetic energy over depth inside the filter layer.

- In layer 1, both the pore velocity and turbulent kinetic energy decrease over depth;
- In layer 2, the pore velocity and turbulent kinetic energy increase from the transition between the layer 1 and 2 until halfway layer 2. The maximum pore velocity and maximum turbulent kinetic energy in layer 2 is present halfway the layer. From that point and deeper, the pore velocity and turbulent kinetic energy decreases;
- In layer 3, the pore velocity and turbulent kinetic energy are constant. A third layer does not lead to a decrease of the pore velocity and turbulent kinetic energy;
- A significant decrease (strong gradient) of the pore velocity and turbulent kinetic energy is present slightly above the transition of layer 2 and 3;
- Beneath two layers the pore velocity and turbulent kinetic energy are dominantly caused by the influence of the energy slope (pressure gradient). This flow is always present, regardless of how thick the filter layer is. At this depth, the pore flow velocity and turbulent kinetic energy have no influence of the flow over the filter structure;
- A filter consisting of logs with at least two layers is stable up to depth-averaged flow velocities of 1 m/s, see Section 6.2.1.

So we can conclude that at least two layers are needed in order to ensure a significant decrease of the pore flow velocity and turbulent kinetic energy. Adding more than two layers will not lead to

further reduction of the pore velocity or turbulent kinetic energy. However, based on the imperfect conditions in reality, it is advised to design a three-layered log filter in order to prevent erosion due to the strong gradient slightly above the transition between layer 2 and 3 in the pore flow velocity and turbulent kinetic energy.

Secondly, the findings regarding the sub-question "*What type of erosion is a log filter inducing on the base layer?*" are visualized in Figure 7.1:

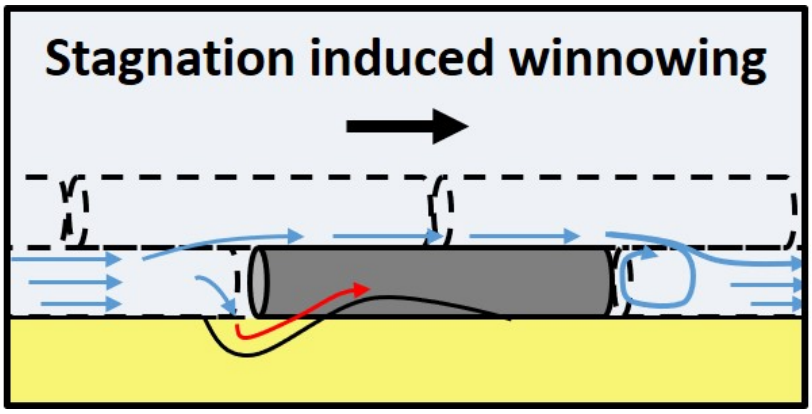

Figure 7.1: Schematic sketch of the flow around a log from the side. In front of the log (upstream) a vertical jet flow is caused by stagnation. Behind the log (downstream) an eddy is present because the flow above the log is higher than behind the log.

- The flow is very anisotropic, see Figure 6.5. The flow characteristics differ in front, halfway and behind the log. In front of the log, a vertical jet flow is induced, whereas behind the log a vertical eddy is present.

- In front of the log the vertical jet flow is caused by stagnation due to the presence of the log. This jet flow initiates erosion in front of the log. Downstream this process the flow velocity reduces and sedimentation occurs. The sedimentation dune downstream the vertical jet flow may become so large that the top of the dune reaches the depth in the filter where the critical flow velocity of the grains is present. In that case, the grains go into suspension, inducing winnowing.

- The erosion caused by stagnation also occurs in layer 2, but the amount of erosion is less due to the lower pore velocities in this layer.

- The flow caused by the vertical jet flow of a log in layer 1 penetrates to a certain depth, see Figure 5.15. The penetration length becomes deeper when the flow velocities over the filter increases.

So we can conclude that, in case of a log filter, the dominant process which causes erosion of the base layer is the vertical jet plane flow due to stagnation in front of the logs in the top layer. This process induces winnowing downstream of the vertical jet flow. This is not aligned with the theory in granular open filters. In granular open filters, the erosion is predominantly caused by the hydraulic load in the filter, i.e. pore flow velocity and turbulent kinetic energy, and the bed pressure fluctuations due to low-frequency vortices in the free flow above the filter.

Next, the conclusions regarding the sub-question "*What are the differences between the hydraulic load reduction in a log filter and a granular open filter?*" are:

- The pore flow velocity caused by the energy slope (gradient) can be well defined by the current formula for the granular open filter by Hoffmans (2012), Equation 2.22;
- It is not possible to describe the pore velocity caused by the flow over the filter structure by the equation of Hoffmans (2012), Equation 2.20. In this formula, the declination of the pore velocity is assumed to be exponential (Figure 2.10). This is not the case if logs are used as the filter, see Figure 4.14 and Figure 6.4a, since the pore flow velocity slightly increases in layer 2.
- The assumption of Klar, which stated that the relative turbulence in the pores is approximately uniform in all directions, is not valid in case of a log filter, see Section 4.3.2. The relative turbulence in the z-direction is 0.5 times the relative turbulence in x and y-direction. This is due to the shape of the pores: the shape of the pores is not circular as in granular open filters.
- The curve of Klar shows that the turbulent kinetic energy is constant at $z/D_{f50} = -5$. However, in case of logs, the turbulent kinetic energy is constant at $z/D_{log} = -2$.
- The turbulent kinetic energy caused by the energy slope (gradient) can be well defined by the current formula for the granular open filter by Hoffmans (2012), Equation 2.25;
- It is not possible to describe the turbulent kinetic energy caused by the flow over the filter structure by the equation of Hoffmans (2012), Equation 2.24. In this formula, the declination of the turbulent kinetic energy is assumed to be exponential, which is not the case if logs are used as the filter, see Figure 4.16 and Figure 6.4b, since the turbulent kinetic energy slightly increases in layer 2.
- The equation describing the damping parameter and damping length derived by Hoffmans are valid to use since the flow in the filter is always turbulent: the filter Reynolds number ranges from 10^3 to 10^6.
- The relative filter turbulence is constant over depth. The relative filter turbulence in case of logs is much lower ($r_{f,log} = 0.36$) than the relative filter turbulence of normal open filter ($r_{f,normal} = 1$). This results in a damping parameter which is much lower than in granular open filters.

At last, the conclusions regarding the sub-question "*Which parameters and variables are important for describing the load reduction?*" are:

- The number of layers is an important parameter for the load reduction of the flow. In order to provide a maximal reduction of the hydraulic load, a two-layer filter should be used. The hydraulic load in layer 3 dominantly depends on the influence of the energy slope. Therefore, the number of layers is important up to the third layer. A log filter consisting of 4 or more layers is not relevant.
- Although no experiments with varying porosity were carried out, visual observations showed consistent behaviour regarding the porosity. The erosion caused by stagnation, which was present at the side of the flume, also occurred in the middle of the flume. However, the

moment of erosion of the base layer in the middle of the flume occurred at higher velocities than at the side of the flume, see Chapter 5.1. This indicates that the vertical jet flow in front of the log in the middle of the flume is more dissipated or blocked than at the side of the flume. Since the porosity is higher at the side of the flume, we conclude that the porosity is an important parameter in the hydraulic load reduction.

7.2 Recommendations

First of all, it is essential to perform research on the flow properties of the anisotropic flow caused by the log filter. From this study, it followed that in front of a log a vertical jet flow is present and behind a log an eddy is present. Therefore, the flow velocities are strongly dependent on the measured location. In this study, the flow measurements were done in the middle and between two logs. However, the erosion occurred at a different location. The erosion was caused by the vertical jet flow in front of the log. Therefore, the measured velocities are not representative flow conditions which cause erosion, see Section 6.1.3. It only indicates the hydraulic load reduction in the middle and between two logs. In order to obtain the flow conditions which cause erosion, additional research regarding the flow properties in front of the log should be carried out, since these flow conditions cause erosion.

Secondly, it is recommended to carry out more research in the influence of the aspect ratio of the logs. In this study, only one aspect ratio was used. However, in reality, the aspect ratio of each log is different. We saw that the erosion is caused by stagnation in front of the log. It is expected that when the area of stagnation is increased, i.e. increasing the diameter of a log, the pressure build-up increases as well, see Section 6.2.3. Increasing the diameter goes hand in hand with decreasing the aspect ratio. Since the aspect ratio is not varied in this study, the effect of this parameter could not be analysed. An additional research should be carried out in which the effect of the underlying soil is regarded by varying the aspect ratio. It could be possible that at a certain aspect ratio the stagnation area has a minor effect on the erosion of the underlying soil. It may be possible to differ the shape of the front of the log as well. If the front of the log is designed in a more streamlined way, the effect of stagnation will be suppressed. However, it is difficult to practice, since the logs are round.

Moreover, from consistent behaviour, we saw that the porosity is an important parameter in the diffusion or blockage of the vertical jet flow caused by stagnation. At the side of the flume, where the porosity was higher, erosion occurred in an earlier stage than in the middle of the flume, where the porosity was lower. This indicates that the way how the logs are packed determines the amount of diffusion of the vertical jet flow caused by the logs in the top layer. A more densely packed log filter will diffuse or block the vertical jet flow more than a loosely packed filter. In reality, the logs will be randomly placed and will be constructed as a bunch of logs. This will leads to local variation in the porosity of the log filter. It is interesting to know which porosity values leads to the same erosion effects and which porosity leads to enough diffusion of the vertical jet flow. Since the porosity is not varied in this research, the effect of the porosity could not be analysed. Therefore, additional experiments should be carried out in which the porosity is varied. This results in an elementary insight which porosity value leads to the same effects as we saw in this thesis.

The same goes for the geometry of the structure: in all experiments, the geometry of the logs was identical and chosen arbitrary on some considerations. In reality, the geometry of the logs is not well structured. Imagine a bunch of logs which are scattering in dimensions and are not ordered

placed. The way how the logs are packed determines the amount of dissipation of the vertical jet flow caused by stagnation. The structured layering of the logs in this research may induce erosion, because of the regular spacing in between the logs. If the logs are more randomly placed, the vertical jet plane flow will be more dissipated, resulting in less erosion. Therefore, it is recommended to locate the logs randomly, instead of placing them in a structured way. An additional research with varying geometry shows which geometry provides a better stability against erosion. So the question is whether a geometry in which the logs are placed more randomly leads to the same effects as the geometry which is used in this research. A combination of different geometries is possible as well: start the filter by placing the logs perpendicular to the flow and further downstream in the longitudinal direction.

In this research, the erosion phase is defined as the moment when a constant supply of sand grains into the sediment trap was present. In that case, the experiment was stopped after one hour. However, it is interesting to know what the erosion processes will be on the long term. Is the erosion phase defined in this research an initial effect or will the logs fail if you continue with the same hydraulic loads? Since the experiments were stopped at the begin of erosion, this question could not be answered. Additional experiments should be carried out in which the time span of each time step is higher. It is possible that the erosion holds after some hours and an equilibrium state has been formed. In that case, the base layer will not erode any further.

Bibliography

[Bailly and Comte-Bellot, 2015] Bailly, C. and Comte-Bellot, G. (2015). *Turbulence*.

[Battjes, 2002] Battjes, A. (2002). Vloeistofmechanica.

[Bezuijen and Köhler, 1996] Bezuijen, A. and Köhler, H.-J. (1996). Filter and revetment design of water imposed embankments induced by wave and draw-down loadings. (January 1996).

[Bosboom and Stive, 2015] Bosboom, J. and Stive, J. (2015). *Coastal Dynamics I*. Delft Academic Press / VSSD, 0.5 edition.

[Burns et al., 2011] Burns, S., Bhatia, S., Avila, C., and Hunt, B. E. (2011). *Scour and Erosion - Proceedings of the Fifth International Conference on Scour and Erosion (ICSE-5) - Knovel*. Amer Society of Civil Engineers.

[CUR, 2010] CUR (2010). *Interface stability of granular filter structures*.

[de Vriend et al., 2011] de Vriend, H., Havinga, H., van Prooijen, B., Visser, P., and Wang, Z. (2011). River Engineering.

[Doroudian et al., 2010] Doroudian, B., Bagherimiyab, F., and Lemmin, U. (2010). Improving the accuracy of four-receiver acoustic Doppler velocimeter (ADV) measurements in turbulent boundary layer. pages 575–591.

[Gadelmawla et al., 2002] Gadelmawla, E. S., Koura, M. M., Maksoud, T. M. A., Elewa, I. M., and Soliman, H. H. (2002). Roughness parameters. *Journal of Materials Processing Technology*, 123(1):133–145.

[Goring and Nikora, 2002] Goring, D. G. and Nikora, V. I. (2002). Despiking Acoustic Doppler Velocimeter Data. *Journal of Hydraulic Engineering*, 128(1):117–126.

[Haage and Çete, 2016] Haage, S. and Çete, C. (2016). *Bodembescherming met behulp van boomstammen*. Bsc thesis, Delft University of Technology.

[Harris et al., 2016] Harris, J., Whitehouse, R., and Moxon, S. (2016). *Scour and Erosion: Proceedings of the 8th International Conference on Scour and Erosion*.

[Hoffmans, 2012] Hoffmans, G. (2012). *The Influence of Turbulence on Soil Erosion*.

[Hughes, 1993] Hughes, S. A. (1993). *Physical Models and Laboratory Techniques in Coastal Engineering*, volume 7.

[Joustra, 2013] Joustra, R. (2013). *Interface stability in granular open filters in unidirectional flows*. Msc thesis, University of Twente.

[Klar, 2005] Klar, M. (2005). *Design of an endoscopic 3-D Particle-Tracking Velocimetry system and its application in flow measurements within a gravel layer*. Doctoral dissertation, University of Heidelberg.

[NortekUSA, 2012] NortekUSA (2012). Vectrino II A profiling bi-static acoustic velocimeter.

[Parsheh et al., 2010] Parsheh, M., Sotiropoulos, F., and Porté-Agel, F. (2010). Estimation of Power Spectra of Acoustic-Doppler Velocimetry Data Contaminated with Intermittent Spikes. *Journal of Hydraulic Engineering*, 136(6):368–378.

[Sagaut, 2013] Sagaut, P. (2013). *Multiscale and Multiresolution Approaches in Turbulence: LES, DES and Hybrid RANS/LES Methods : Applications and Guidelines*.

[Schiereck, 2016] Schiereck, G. (2016). *Introduction to bed, bank and shore protection*. Delft Academic Press / VSSD, 2nd edition.

[Sellmeyer, 1988] Sellmeyer, J. (1988). On the mechanism of piping under impervious structures. *Repository.Tudelft.Nl*, page 116.

[Sutherland and Soulsby, 2010] Sutherland, J. and Soulsby, R. (2010). Guidelines for physical modelling of mobile sediments. *Proc. Coastlab 2010*, (October):15pp.

[van de Sande, 2013] van de Sande, S. (2013). *Stability of Open Filter*. Msc thesis, Delft University of Technology.

[van de Sande et al., 2014] van de Sande, S., Uijttewaal, W., and Verheij, H. (2014). Validation and optimization of a design formula for stable geometrically open filter structures. *Proceedings of the Coastal Engineering Conference*.

[van Leeuwen et al., 2016] van Leeuwen, P., van Olst, L., and van der Scheer, B. (2016). *Bodembescherming met behulp van boomstammen*. Bsc thesis, Delft University of Technology.

[van Os, 1998] van Os, P. (1998). *Hydraulische belasting op een geometrisch open filterconstructie*. Msc thesis, Delft University of Technology.

[van Rijn, 1993] van Rijn, L. (1993). *Principles of Sediment Transport in Rivers, Estuaries and Coastal Seas*.

[Verheij et al., 2012] Verheij, H., Hoffmans, G., Dorst, K., and Vandesande, S. (2012). Interface stability of granular filter structures under currents. *Icse6*, (1):241–248.

[Vries, 1982] Vries, M. D. (1982). Scale Models in Hydraulic Engineering. (January):415.

A Literature

A.1 Dimensionless numbers

The following dimensionless characters are used in this thesis:

1. Froude number Fr;
2. Reynolds number Re;
3. Particle Reynolds number Re_*;
4. filter Reynolds number Re_f;
5. Particle diameter D_*.

A.1.1 Froude number

The Froude number relates the inertial forces to gravity and it describes the type of flow. The flow is called supercritical when $Fr > 1$ and called subcritical flow when $Fr < 1$ [van Rijn, 1993]. The Froude number is calculated by:

$$Fr = \frac{\overline{U}}{\sqrt{gh}} \tag{A.1}$$

in which:

$\overline{U}$	depth-averaged flow velocity in an open channel [m/s];
g	gravitational constant [m/s^2]
h	water level [m].

A.1.2 Reynolds number

The Reynolds number relates the inertial forces to the viscous forces and specifies the type of the flow. Laminar flow is present when $Re < 500$, in which the viscous forces are dominant. Turbulent flow is present when $Re > 2000$, in which the inertial forces are dominant [van Rijn, 1993]. In this case, random eddies, vortices and fluctuations are caused by the flow. The Reynolds number is defined as:

$$Re = \frac{R\bar{U}}{\nu} \tag{A.2}$$

in which:

R	hydraulic radius [m];
ν	kinematic viscosity coefficient [-].

A.1.3 Particle Reynolds number

The hydraulic conditions near the bed are expressed by the particle Reynolds number [Hoffmans, 2012] [van Rijn, 1993]:

$$Re_* = \frac{u_* d}{\nu} \tag{A.3}$$

in which:

u_*	shear velocity [m/s];
d	grain diameter [m].

A.1.4 Filter Reynolds number

The filter Reynolds number is a dimensionless number that is a measure of the type of flow through a porous medium. Three basic types are present: laminar $Re_f \leq 10$, transitional $10 < Re_f < 1000$ and turbulent $Re_f > 1000$. The filter Reynolds number is defined as [Hoffmans, 2012]:

$$Re_f = \frac{d_{f50}\overline{u_p}}{\nu} \tag{A.4}$$

in which:

d_{f50}	median diameter of filter [m];
$\overline{u_p}$	time-averaged local pore velocity [m/s].

A.1.5 Particle diameter

The particle diameter D_* is the influence of gravity, density and viscosity on a particle [Hoffmans, 2012]:

$$D_* = [\frac{(s-1)g}{\nu^2}]^{1/3} d_{50} \tag{A.5}$$

in which:

s	specific gravity ($=\rho_s/\rho$) [-];
d_{50}	median particle diameter of bed material [m].

A.2 Basics of current fluid mechanics

A two dimensional considered open channel consisting of a very gentle slope ($\tan i_b = -dz_b/dx << 1$) and no changes in depth of the bed in y-direction results in a uniform flow, see Figure A.1. In this situation the average velocity and depth of the flow does not vary in the flow direction, which means the energy line and the piezometric head are parallel to the bottom of the river. From this two dimensional considered flow, the shear stress and velocity could be derived from the vertical [Battjes, 2002].

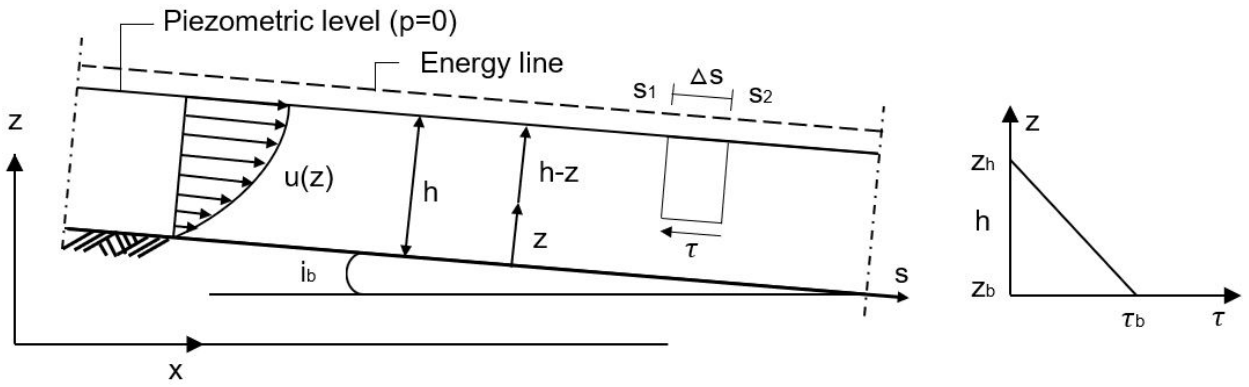

Figure A.1: Two dimensional open channel with no change in depth in y-direction

For the derivation of the bottom shear stress a impulse balance is made, which is a column that reaches a certain depth z from the bottom until the water surface ($z = h$). The component of the weight of the column in flow direction per unit width has to be in equilibrium with the shear force per unit width. The bed shear stress (τ_b) is defined as follows:

$$\tau_b = \rho g R i_b = \rho g h i_b \tag{A.6}$$

in which:

h	water depth [m], which only can be used for an infinitely wide channel;
i_b	the bottom slope [−].

In order to provide a relation between the resistance of the bed (bed shear stress) and the average flow velocity $\overline{\overline{u}}$, the following formula is used [Schiereck, 2016]:

$$\tau_b = c_f \rho \overline{\overline{u}}^2 = \rho u_*^2 = \rho \overline{u'w'} \tag{A.7}$$

in which:

c_f	friction coefficient (between flow and wall) [-];
ρ	water density [kg/m^3];
$\overline{\overline{u}}$	averaged flow velocity over turbulence period and over water depth [m/s];
u_*	shear velocity [m/s].

Combining Equation A.6 and A.7 lead to the formula which provide a relation between the resistance and the average flow:

$$\tau_b = \rho g h i_b = c_f \rho \overline{\overline{u}}^2 = \rho u_*^2 \tag{A.8}$$

In the past, many research related the discharge and average flow velocity empirical, such as:

$$\text{Chezy}: \quad \overline{\overline{u}} = C\sqrt{R i_b} \quad \text{with}: C = \sqrt{\frac{g}{c_f}} \tag{A.9}$$

$$\text{Manning}: \quad \overline{\overline{u}} = \frac{1}{n} R^{2/3} \sqrt{i_b} \quad \text{with}: n = R^{1/6}\sqrt{\frac{c_f}{g}} \tag{A.10}$$

in which:

C Chézy coefficient [$m^{1/2}/s$];
n Manning number [$s/m^{1/3}$].

The expression of the friction coefficient depends on the hydraulic regime. The type of hydraulic regimes itself depends on the ratio between the Nikuradse roughness (k_r) and the length scale of the viscous sublayer ($\nu/u_{*,c}$). Three different hydraulic regimes are possible:

- Hydraulic rough flow: the roughness elements are so large that no viscous sublayer is present and the velocity distribution does not depend on the viscosity (ν), Figure A.2;
- Hydraulic smooth flow: the roughness elements are much smaller than the viscous sublayer and do not affect the velocity distribution, Figure A.2;
- Hydraulic transitional flow: the velocity distribution depends on both the viscosity and bottom roughness.

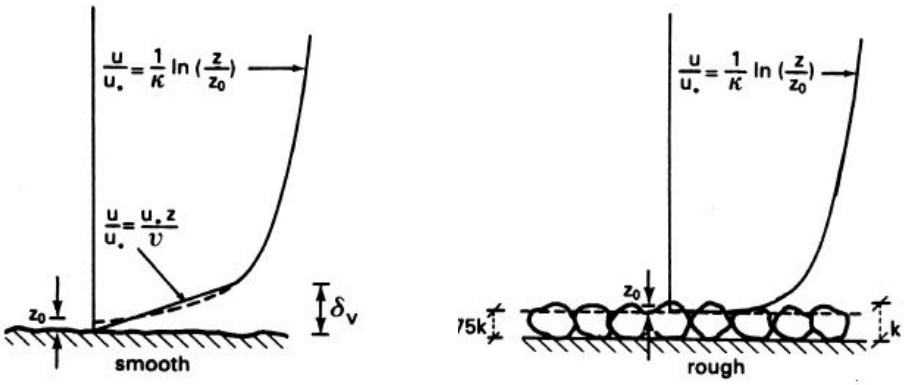

(a) Hydraulic smooth (b) Hydraulic rough

Figure A.2: Velocity distribution of hydraulic smooth and hydraulic rough regime [van Rijn, 1993].

The Nikuradse roughness (k_r) is the roughness of the bottom which influence the velocity distribution close to the bottom. The elements on the bed generate eddies which affect the turbulent structure and therefore the flow velocity near the bed. Further away from the bed the small eddies will be absorbed by the larger eddies from the flow above the bed. In general for a flat bed in a flume experiment $k_r \approx 3d_{n50}$ is used [Schiereck, 2016]. Usually the following k_r for wood and PVC are given in table A.1.

Type material	k_r [m]
old wood	$1 \cdot 10^{-3} < k_r < 2 \cdot 10^{-3}$
not polished wood	$5 \cdot 10^{-4} < k_r < 1 \cdot 10^{-3}$
polished wood	$4 \cdot 10^{-4} < k_r < 5 \cdot 10^{-4}$
PVC	$3 \cdot 10^{-5} < k_r < 4 \cdot 10^{-5}$

Table A.1: Roughness for wood and PVC [Battjes, 2002]

The sediment in an open channel is usually made of alluvial maeterial and consist of ripples. Therefore, the flow is alsways assumed as a hydraulic rough regime and an expression of the friction coefficient is obtained using the Nikuradse-Colebrook formula [Battjes, 2002]:

$$\frac{1}{c_f} = 5.75 \log \frac{12R}{k_r} \tag{A.11}$$

The hydraulic regime depends on the parameter k^+:

$$k^+ = \frac{u_{*,c} k_r}{\nu} \begin{cases} \text{for hydraulic rough bed:} & k^+ \geq 70 \\ \text{for hydraulic smooth bed:} & k^+ \leq 5 \\ \text{for transition zone:} & 5 < k^+ < 70 \end{cases} \tag{A.12}$$

Knowing the hydraulic regime, the Chezy value could be calculated [van Rijn, 1993]:

$$C = \begin{cases} \text{for hydraulic rough flow:} & C = 18 \log(\frac{12h}{k_r}) \\ \text{for hydraulic smooth flow:} & C = 18 \log(\frac{12h}{3.3\nu/u_{*,c}}) \\ & C = 18 \log(\frac{11.4h}{\nu C/\overline{\overline{u}}}) \\ \text{for transitional flow:} & C = 18 \log(\frac{12h}{k_r + 3.3\nu/u_{*,c}}) \\ & C = 18 \log(\frac{12h}{k_r + 1.05\nu C/\overline{\overline{u}}}) \end{cases} \tag{A.13}$$

The general flow distribution as function of depth is as follows:

$$u(z) = \frac{u_{*,c}}{\kappa} \ln(\frac{z}{y_0}) \tag{A.14}$$

with

$$y_0 \approx \begin{cases} 0.033\ k_r & \text{for hydraulic rough bed} \quad (k^+ \geq 70) \\ 0.11\ (\nu/u_{*,c}) & \text{for hydraulic smooth bed} \quad (k^+ \leq 5) \\ 0.11 \frac{\nu}{u_{*,c}} + 0.033\ k_r & \text{for transition zone} \quad (5 < k^+ < 70) \end{cases} \tag{A.15}$$

in which:

κ	Von Kármán constant (≈ 0.4) [-];
z	depth, with respect to bottom [m];
y_0	zero-velocity level in which u = 0 in h(z)=y_0 [m].

The zero-velocity level is often defined as the plane that is formed after smoothing the roughness elements. Normally this is a value of $\approx 0.75 k_r$ above the underside of the elements on top of the bed. Realistic values of zero-velocity level (z = y_0) are obtained by plotting u/u_* against $z - z_0'/z_0'$ on semi-logarithmic scale and varying z_0' until best fit is obtained (for sand and gravel $z_0' \approx 0.25 k_r$).

In a two dimensional open channel with turbulent flow a logarithmic flow velocity profile (in z-direction) is present explained by the following formula [Battjes, 2002]:

$$\frac{\overline{\overline{u}}}{u_*} = \frac{1}{\kappa} \ln(e^{-1} \frac{z}{y_0}) \quad \Rightarrow \quad \frac{1}{\sqrt{c_f}} = \frac{1}{\kappa} \ln(e^{-1} \frac{z}{y_0}) \tag{A.16}$$

The maximum flow velocity is at the free surface ($z = h$):

$$u_{max} = \frac{u_*}{\kappa} \ln(\frac{h}{y_0}) \tag{A.17}$$

Combining A.16 and A.17 results in:

$$\frac{u_{max}}{\bar{\bar{u}}} = 1 + \frac{\sqrt{c_f}}{\kappa} \tag{A.18}$$

The following turbulence relations are found in the outer flow of uniform, for $u_* z/\nu > 70$, for smooth beds [Hoffmans, 2012]:

$$\overline{u(z)'} = \sigma_u(z) = \alpha_u u_* \exp(-\frac{z}{h}) \tag{A.19}$$

$$\overline{v(z)'} = \sigma_v(z) = \alpha_v u_* \exp(-\frac{z}{h}) \tag{A.20}$$

$$\overline{w(z)'} = \sigma_w(z) = \alpha_w u_* \exp(-\frac{z}{h}) \tag{A.21}$$

in which α_u (=1.92), α_v (=1.34) and α_w (=1.06) are coefficients.

For channels with smooth and rough beds, the turbulence distributions are almost the same and the turbulence energy as function of depth can be written as follows [Hoffmans, 2012]

$$k(z) = \frac{1}{2}(\overline{u(z)'^2} + \overline{v(z)'^2} + \overline{w(z)'^2} = k_b \exp(-\frac{2z}{h}) \tag{A.22}$$

with

$$k_b = \chi u_*^2 \tag{A.23}$$

in which k_b is the turbulence energy at $k^+ = 70$ and χ (= 3.3) is a constant used in k-ϵ models.

The depth-averaged turbulence energy ($\bar{k_0}$) is defined as follows:

$$k_0 = \frac{1}{h}\int_0^h k(z)dz = (\alpha_0 u_*)^2 \tag{A.24}$$

in which α_0 (=1.2) is the factor of α_u, α_v and α_w combined.
The depth-averaged turbulence intensity can be approximated with [Schiereck, 2016] [Hoffmans, 2012]:

$$\bar{r} = \frac{\sqrt{k_0}}{\bar{\bar{u}}} = \alpha_0 \frac{u_*}{\bar{\bar{u}}} = \alpha_0 \frac{\sqrt{g}}{C} = 1.2\frac{\sqrt{g}}{C} \qquad r_{xz} = \frac{\overline{u'w'}}{\bar{\bar{u}}^2} = \frac{g}{C^2} \qquad (\text{with } u_*^2 = \overline{u'w'}) \tag{A.25}$$

in which:

$\bar{r}$	relative depth averaged turbulence intensity [-];
r_{xz}	relative turbulent shear stress in x,z [-].

In reality the flow is never fully uniform. The flow is regarded uniform if the boundary layer is fully developed. The boundary layer is the region in which the water is influenced by the bottom or wall. A fully developed boundary layer means the entire water column is influenced by the wall. The growth of the boundary layer is shown in figure A.3, in which the growth $\partial(x) \approx 0.02x$ to $\approx 0.03x$. Consequently, a fully developed flow is present at 30 to 50 times the water depth.

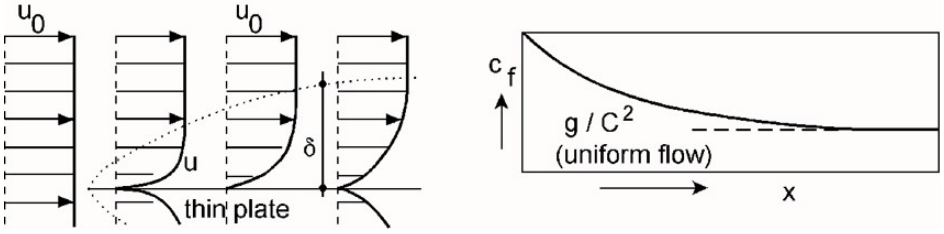

Figure A.3: Growth boundary layer

A.3 Shields curve

The Shields curve consist of three ranges [van Rijn, 1993]:

$$\begin{aligned} \psi_c &\geq 0.0035 && \text{for} \quad Re_* \leq 5, \text{ hydraulic smooth regime} \\ 0.03 \leq \psi_c &\leq 0.04 && \text{for} \quad 5 \leq Re_* \leq 70, \text{ transitional regime} \\ 0.04 \leq \psi_c &\leq 0.06 && \text{for} \quad Re_* \geq 70, \text{ hydraulic rough regime} \end{aligned}$$

However, the Shields curve is not practical, since it needs a iteration of ψ_c and Re_*. Van Rijn expressed the critical shields parameter with the dimensionless particle number D_* (Appendix A.1.5):

$$\begin{aligned} \psi_c &= 0.24 D_*^{-1} && \text{for} \quad 1 < D_* \leq 4 \\ \psi_c &= 0.14 D_*^{-0.64} && \text{for} \quad 4 < D_* \leq 10 \\ \psi_c &= 0.04 D_*^{-0.1} && \text{for} \quad 10 < D_* \leq 20 \\ \psi_c &= 0.013 D_*^{0.29} && \text{for} \quad 20 < D_* \leq 150 \\ \psi_c &= 0.055 && \text{for} \quad D_* > 150 \end{aligned} \tag{A.26}$$

A.4 Derivation Navier-stokes equations

At first the equations that govern the evolution of a fluid has to be explained, also known as the Navier-Stokes equations. The equations of motion are derived from the combination of the continuity equation (from the mass balance) and the momentum equations.

The mass balance for a fluid element can be described as follows:

Rate of increase of mass in fluid element = Net flux of mass into fluid element

The rate of increase of mass in fluid element is given by:

$$\frac{\partial}{\partial t}(\rho dx dy dz) = \frac{\partial \rho}{\partial t} dx dy dz \tag{A.27}$$

The flux of mass into fluid element is given by:

$$[\rho u + \frac{\partial(\rho u)}{\partial x} dx] dy dz - (\rho u) dy dz + [\rho v + \frac{\partial(\rho v)}{\partial y} dy] dx dz - (\rho v) dx dz + [rhow + \frac{\partial(\rho w)}{\partial z}] dx dy - (\rho w) dx dy \tag{A.28}$$

Combining these 2 terms and simplification results in the three-demensiona mass conservation, also know as the continuity equation:

$$\frac{\partial \rho}{\partial t} + \frac{\partial((\rho u)}{\partial x} + \frac{\partial(\rho v)}{\partial y} + \frac{\partial(\rho w)}{\partial z} = 0 \tag{A.29}$$

For an incompressible fluid the continuity equation simplifies to:

$$\frac{\partial u}{\partial x} + \frac{\partial v}{\partial y} + \frac{\partial w}{\partial z} = 0 \quad \Rightarrow \quad \nabla V = 0 \tag{A.30}$$

Following Newton's Second Law the rate of change of momentum of a fluid particle equals the forces on the particle:

Rate of increase of momentum in fluid element = sum of forces on fluid element

$$\underbrace{\rho dxdydz}_{\text{mass}} \underbrace{\frac{DV}{Dt}}_{\text{acceleration}} = \underbrace{F}_{\text{forces}}$$

This equation has three components, i.e. the rate of increase of momentum in fluid element in x-direction balances the sum of forces on the fluid element in x-direction. The rate of increase of momentum of all direction is as follows:

$$\underbrace{\rho dxdydz\frac{Du}{Dt}}_{\text{x-direction}} = (\frac{\partial \rho u}{dt} + \frac{\partial(\rho uu)}{\partial x} + \frac{\partial(\rho uv)}{\partial y} + \frac{\partial(\rho uw)}{\partial z})dxdydz \tag{A.31}$$

$$\underbrace{\rho dxdydz\frac{Du}{Dt}}_{\text{y-direction}} = (\frac{\partial \rho v}{dt} + \frac{\partial(\rho vu)}{\partial x} + \frac{\partial(\rho vv)}{\partial y} + \frac{\partial(\rho vw)}{\partial z})dxdydz \tag{A.32}$$

$$\underbrace{\rho dxdydz\frac{Dw}{Dt}}_{\text{z-direction}} = (\frac{\partial \rho w}{dt} + \frac{\partial(\rho wu)}{\partial x} + \frac{\partial(\rho wv)}{\partial y} + \frac{\partial(\rho ww)}{\partial z})dxdydz \tag{A.33}$$

The forces which acts on a fluid can be distinguished in two types:

Type of force		equation in z-direction
Surface forces	Pressure forces (in every direction)	$-\frac{\partial \rho}{\partial z}dxdydz$
	Viscous forces (in every direction)	$[\frac{\partial \tau_{xz}}{\partial x} + \frac{\partial \tau_{yz}}{\partial y} + \frac{\partial \tau_{zz}}{\partial z}]dxdydz$
Body forces	Gravity (only in z-direction)	$-\rho g k dxdydz$

Table A.2: Forces which acts on a fluid

Combining equation A.31, A.32, A.33 and A.2 results in the moment equation in all directions, x, y and z respectively. These equation are known as the Navier-Stokes equation or equations of motion:

$$\rho\frac{Du}{Dt} = -\frac{\partial p}{\partial x} + [\frac{\partial \tau_{xx}}{\partial x} + \frac{\partial \tau_{yx}}{\partial y} + \frac{\partial \tau_{zx}}{\partial z}] \tag{A.34}$$

$$\rho\frac{Dv}{Dt} = -\frac{\partial p}{\partial y} + [\frac{\partial \tau_{xy}}{\partial x} + \frac{\partial \tau_{yy}}{\partial y} + \frac{\partial \tau_{zy}}{\partial z}] \tag{A.35}$$

$$\rho\frac{Dw}{Dt} = -\frac{\partial p}{\partial z} - \rho g + [\frac{\partial \tau_{xz}}{\partial x} + \frac{\partial \tau_{yz}}{\partial y} + \frac{\partial \tau_{zz}}{\partial z}] \tag{A.36}$$

A.5 Derivation Reynolds averaged Navier-Stokes equations

If the smallest scale of motion are in the order of a few millimetres, it is impossible to resolve fluctuations on all scales in a numerical model. Therefore Reynolds decomposition is used, in which velocities are divided by an average ($\bar{u}$) and fluctuation part (u'):

$$u = \bar{u} + u' \quad \bar{u}' = 0 \quad \bar{u} = \overline{\bar{u} + u'} \tag{A.37}$$

Using Reynolds decomposition into the Navier-stokes Equation in combination with the continuity equation (for the last three terms) results in the Reynolds averaged Navier-Stokes (RANS) equations:

$$\frac{\partial \bar{u}}{\partial t} + \frac{\partial \bar{u}\bar{u}}{\partial x} + \frac{\partial \bar{u}\bar{v}}{\partial y} + \frac{\partial \bar{u}\bar{w}}{\partial z} + \frac{1}{\rho}\frac{\partial \bar{p}}{\partial x} + [\frac{\partial \overline{u'u'}}{\partial x} + \frac{\partial \overline{v'u'}}{\partial y} + \frac{\partial \overline{w'u'}}{\partial z}] = 0 \tag{A.38}$$

$$\frac{\partial \bar{v}}{\partial t} + \frac{\partial \bar{u}\bar{v}}{\partial x} + \frac{\partial \bar{v}\bar{v}}{\partial y} + \frac{\partial \bar{v}\bar{w}}{\partial z} + \frac{1}{\rho}\frac{\partial \bar{p}}{\partial y} + [\frac{\partial \overline{u'v'}}{\partial x} + \frac{\partial \overline{v'v'}}{\partial y} + \frac{\partial \overline{w'v'}}{\partial z}] = 0 \tag{A.39}$$

$$\frac{\partial \bar{w}}{\partial t} + \frac{\partial \bar{u}\bar{w}}{\partial x} + \frac{\partial \bar{v}\bar{w}}{\partial y} + \frac{\partial \bar{w}\bar{w}}{\partial z} + \frac{1}{\rho}\frac{\partial \bar{p}}{\partial w} + g + [\frac{\partial \overline{u'w'}}{\partial x} + \frac{\partial \overline{v'w'}}{\partial y} + \frac{\partial \overline{w'w'}}{\partial z}] = 0 \tag{A.40}$$

The first 6 terms of the RANS equations are large scale flows (average) and the last three terms are the small scale flows (fluctuations). The moment flux due to small scale motion are equivalent to a stress, called the Reynolds stresses. The Reynolds stresses consist of three normal stresses (i.e. τ_{xx}) and three shear stresses (i.e. τ_{xy}):

$$\begin{aligned} \text{Normal stresses} \quad & \tau_{xx} = -\overline{\rho u'u'}, \quad \tau_{yy} = -\overline{\rho v'v'}, \quad \tau_{zz} = -\overline{\rho w'w'} \\ \text{Shear stresses} \quad & \tau_{xy} = \tau_{yx} = -\overline{\rho u'v'}, \quad \tau_{xz} = \tau_{zx} = -\overline{\rho u'w'}, \quad \tau_{yz} = \tau_{zy} = -\overline{\rho v'w'} \end{aligned}$$

Filling in the Reynolds stresses the RANS-equations becomes:

$$\frac{\partial \bar{u}}{\partial t} + \frac{\partial \bar{u}\bar{u}}{\partial x} + \frac{\partial \bar{u}\bar{v}}{\partial y} + \frac{\partial \bar{u}\bar{w}}{\partial z} + \frac{1}{\rho}\frac{\partial \bar{p}}{\partial x} + \frac{1}{\bar{\rho}}[\frac{\partial \tau_{xx}}{\partial x} + \frac{\partial \tau_{xy}}{\partial y} + \frac{\partial \tau_{xz}}{\partial z}] = 0 \tag{A.41}$$

$$\frac{\partial \bar{v}}{\partial t} + \frac{\partial \bar{u}\bar{v}}{\partial x} + \frac{\partial \bar{v}\bar{v}}{\partial y} + \frac{\partial \bar{v}\bar{w}}{\partial z} + \frac{1}{\rho}\frac{\partial \bar{p}}{\partial y} + \frac{1}{\bar{\rho}}[\frac{\partial \tau_{yx}}{\partial x} + \frac{\partial \tau_{yy}}{\partial y} + \frac{\partial \tau_{yz}}{\partial z}] = 0 \tag{A.42}$$

$$\frac{\partial \bar{w}}{\partial t} + \frac{\partial \bar{u}\bar{w}}{\partial x} + \frac{\partial \bar{v}\bar{w}}{\partial y} + \frac{\partial \bar{w}\bar{w}}{\partial z} + \frac{1}{\rho}\frac{\partial \bar{p}}{\partial w} + g + \frac{1}{\bar{\rho}}[\frac{\partial \tau_{zx}}{\partial x} + \frac{\partial \tau_{zy}}{\partial y} + \frac{\partial \tau_{zz}}{\partial z}] = 0 \tag{A.43}$$

A.6 Fall velocity

When a particle moves in still and clear water it will accelerate until it reaches a equilibrium between the upward force, drag force F_D (eq. A.44) and the downward force, gravitational force F_g (eq. A.45). Equilibrium of the forces leads to the definition of the fall velocity w_s:

$$F_D = \frac{1}{2} C_D \cdot \rho \cdot w_s^2 (\frac{\pi}{4} d^2) \tag{A.44}$$

$$F_G = (\rho_s - \rho) g (\frac{\pi}{6} d^3) \tag{A.45}$$

$$\Downarrow$$

$$w_s = \sqrt{\frac{4(s-1)g \cdot d}{3C_D}} \tag{A.46}$$

in which C_D is the drag coefficient and d the diameter of the grain. So, the fall velocity depends on the density of the fluid and grains, the size of the grain and the drag coefficient.

The drag coefficient depends on the shape and roughness of the grain and on the particle Reynolds-number. The particle Reynolds-number Re indicates whether the grain protrudes into the turbulent

boundary layer or is only present in the viscous sub-layer. The grain Reynolds number is defined as [Bosboom and Stive, 2015]:

$$Re = w_s d/\nu \tag{A.47}$$

in which:

ν kinematic viscosity coefficient (1.33 10^{-6} m^2/s). This represents the fluid's internal resistance to flow and is a function of the temperature and to a smaller extent of the density.

High values of Re ($400 < Re < 2 * 10^5$) indicates large grains which exceed the viscous sub-layers, also called the Newton range. The drag coefficient becomes constant ($C_D = 0.5$) and therefore the fall velocity depends on the square root of the diameter of the grain (eq. A.51) [Schiereck, 2016].

Small values of Re ($Re < 0.5$) is the so-called Stoke-range and the drag coefficient is described as:

$$C_d = 25/Re \tag{A.48}$$

The fall velocity at low values of Re will depends on the square of the grain diameter, the relative density and the kinematic viscosity coefficient (eq A.49).

The particle Reynolds number of very low and high values are discussed, which represents silt, clay and gravel respectively. However, the fall velocity of sand is in the transition range between the square root and square root dependency of the grain diameter. So far, no simple relationship in this transition range is made and therefore empirical formulas for the fall velocity of sand is used. An example is the Van Rijn formula (eq. A.50) [Schiereck, 2016].

$$w_s = \frac{\Delta g d^2}{18\nu} \qquad \text{for} \quad 1 < d \leq 100\ \mu\text{m} \tag{A.49}$$

$$w_s = \frac{10\nu}{d}\left(\sqrt{1 + \frac{0.01\Delta g d^3}{\nu^3}} - 1\right) \qquad \text{for} \quad 100 < d \leq 1000\ \mu\text{m} \tag{A.50}$$

$$w_s = 1.1\sqrt{\Delta g d} \qquad \text{for} \quad d > 1000\ \mu\text{m} \tag{A.51}$$

The fall velocity does not only depend on the diameter of the grain, it does also depend on the environment. Example of environmental influences are the temperature, the vicinity of the walls and the presence of other grains. The latter is present with hindered settling, in which the fall velocity decreases [de Vriend et al., 2011].

A.7 Critical gradient in granular filters

The ratio between the load and strength on grains is called gradient i. The load is defined as the hydraulic load and the strength is the erosive capacity (stability) of material. The critical gradient i_c is the gradient in which the grains under an filter layer start to move.

In geometrically closed filters the critical gradient is not in question, because the ratio of the grain diameters between the layers are designed in such a way that the grains of the underlying layer can not pass the pores of grains in the filter layer. However, the critical gradient in case of a geometrically open filters is very important. It describes the moment when the hydraulic load exceeds the stable situation and when the filter becomes unstable, see Figure A.4.

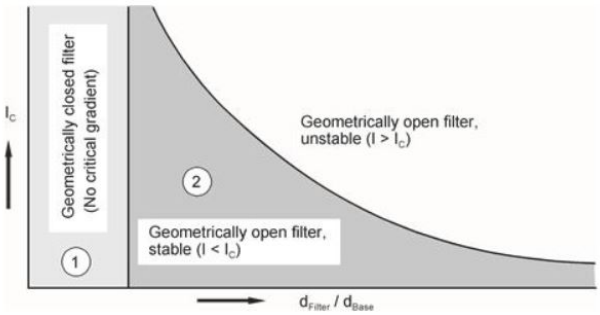

Figure A.4: Critical gradient for the ratio between de filter and base diameter [Schiereck, 2016]

A.8 Forcheimer equation

When all (quadratic) inertia and turbulence terms in Equation 2.18 are replaced by a (linear) viscous gradient, the following formula is obtained:

$$\frac{1}{\rho g}\frac{\delta p}{\delta x} = i = au_f + bu_f|u_f| + c\frac{\delta u_f}{\delta t} \quad \text{with} \quad a = \alpha\frac{(1-n_f)^2}{n_f^3}\frac{\nu}{gd_{n50,f}^2} \quad b = \beta\frac{1-n}{n^3}\frac{1}{gd_{n50,f}} \tag{A.52}$$

in which:

p	pressure [kPa];
i	gradient material, which is the ratio between the hydraulic load and strength of the grains [-];
ν	kinematic viscosity of water [m^2/s];
d_{n50}	nominal diameter grain size of which 50% of the grains is finer [m];
a	model coefficient [s/m] ;
b	model coefficient [s^2/m^2];
c	model coefficient [s^2/m];
α	model constant and for first estimate $\approx$ 1000 [-];
β	model constant and for first estimate $\approx$ 1.1 [-].

The values of α and β and consequently a and b are obtained by field tests.

For stationary flow the last term in Equation A.52 is equal to zero and the classical Forcheimer-equation is obtained:

$$\frac{1}{\rho g}\frac{\delta p}{\delta x} = i = \underbrace{au_f}_{\text{laminar term}} + \underbrace{bu_f|u_f|}_{\text{turbulent term}} \tag{A.53}$$

The first term at the right hand side of the Forcheimer equation is the linear laminar term and the second term at the right hand side is the quadratic turbulent term. If only laminar flow is present, i.e. sand or clay, the Forcheimer equation turns into Darcy's law:

$$u_f = \kappa i \tag{A.54}$$

in which κ is the permeability. Note that the permeability κ in Darcy's law is equal to the inverse of a in Equation A.53.

The quadratic turbulent term of the Forcheimer equation is present using rock. For gravel, both laminar and turbulent term are present, since it is in the transition of both terms.

The values of the permeability (κ) of sand, gravel and rock with the character of the flow are given in Table A.3. These values are guidelines. In practice, the permeability of the filter material has to be determined [van Os, 1998]. This could be done by in-situ test, which has to be carried out in such a way that the total discharge of the groundwater flow is involved. The groundwater flow could be involved by monitoring at several location the head in the sandy layer during changes in the outer water level [Sellmeyer, 1988]. When the permeability is determined it is possible to obtain the gradient of the material and the filter velocity.

Table A.3: Material with values of permeability and the character of the flow

Material	d_{n50} [m]	κ [m/s]	Character of the flow
Sand	$63{\cdot}10^{-6}$ - $2{\cdot}10^{-3}$	10^{-6} - 10^{-3}	laminar
Gravel	$2{\cdot}10^{-3}$ - $63{\cdot}10^{-3}$	10^{-3} - $5{\cdot}10^{-1}$	transition
Rock	$63{\cdot}10^{-3}$ - 1	$5{\cdot}10^{-1}$ - 1	turbulent

A.8.1 Laminar flow

Using Darcy's law (Equation A.54) in combination with the continuity equation, the Laplace equation is found [Schiereck, 2016]:

$$\kappa_x \frac{\delta^2 h}{\delta x^2} + \kappa_z \frac{\delta^2 h}{\delta z^2} = 0 \tag{A.55}$$

in which the piezometric head (h) is used instead of pressure (p). For simple geometries this equation could be solved analytically. For complex situations the equation should be solved numerically.

The flow force which is acting on the grains is defined as:

$$F_f = \rho g i = \rho g \frac{\delta h}{\delta x} \tag{A.56}$$

The grains at the outer boundaries of the soil has to withstand this force in order to be stable. The equation holds for all directions.

A.8.2 Turbulent flow

In case of high turbulence character of the flow the laminar term in the Forcheimer relation (Equation A.53) could be neglected and the filter velocity becomes as follows [van Rijn, 1993]:

$$u_f = \sqrt{\frac{in^3 g d_{n50}}{\beta(1-n)}} \tag{A.57}$$

A.9 Design equations of geometrically open filters

Graauw (1983) made an empirical relation between the critical gradient (i_c) in porous flow and the Forcheimer equation with the threshold of movement by Shields for closed streamlines [CUR, 2010]:

$$i_c = (\underbrace{\frac{0.06}{n_f^3 \cdot d_{15f}^{4/3}}}_{\text{laminar part}} + \underbrace{\frac{n_f^{5/3} \cdot d_{15f}^{1/3}}{1000 \cdot d_{50b}^{5/3}}}_{\text{turbulent part}}) u_{*c}^2 \tag{A.58}$$

in which:

n_f	porosity filter layer [-];
u_{*c}	the critical shear velocity [m/s].

Klein Breteler derived an empirical formula for the critical filter velocity in a closed streamlines filter structure in 1987 [CUR, 2010]:

$$u_{f,c} = [\frac{n_f}{c}(\frac{d_{15f}}{\nu})^m (\psi_b \cdot \Delta_b \cdot g \cdot d_{50b})^{0.5}]^{\frac{1}{1-m}} \tag{A.59}$$

in which:

$$c = \begin{cases} 1.18 & \text{for} \quad d_{50b} = 0.1 \text{ mm} \\ 0.22 & \text{for} \quad d_{50b} = 1.0 \text{ mm} \end{cases} \quad \text{and} \quad m = \begin{cases} 0.25 & \text{for} \quad d_{50b} = 0.1 \text{ mm} \\ 0.00 & \text{for} \quad d_{50b} = 1.0 \text{ mm} \end{cases} ;$$

ν	kinematic viscosity of water [m^2/s];
ψ_b	bed transport parameter [-];
Δ_b	relative density of the base layer [-].

This formula is only valid for base material diameter between between 0.1 mm and 1.0 mm. Furthermore, the equation did not consider the entrainment of turbulent pressure and velocity fluctuations from the flow above the filter. Klein Breteler derived the equation from block revetments, which cause a strong damping of turbulence. This is not always the case for other type of open filters [CUR, 2010].

Combining the Klein Breteler formula (Equation A.59), the turbulent part of the Forcheimer relation (Equation A.57) and $n_f \approx 0.5$ results in a relation between the Shields-parameter and the critical gradient for closed streamlines defined as follows [van Os, 1998]:

$$\psi_b = \frac{c^2 \alpha}{\beta} \cdot (\frac{d_{50f} \cdot i_c}{\Delta_b \cdot d_{50b}}) \tag{A.60}$$

In case of bed protection in rivers, the gradient is very small and according to Equation A.58 the ratio between is very large. However, the influence of free flow above the filter layer is not considered.

Due to different flow velocity between the stationary, uniform flow above the filter layer and the flow in the filter layer a shear stress exist at the transition between the two flows layers. According to Hoffmans (1996) a shear stress also occur at the transition between the filter layer and base layer and he derived the following formula:

$$\tau_b = \tau_0 \frac{\beta \cdot d_{50f}}{c_2 \cdot R} = \frac{\beta}{c_2} \rho \cdot g \cdot i \cdot d_{50f} \tag{A.61}$$

in which c_2 is a model constant which depends on the porosity of the filter material.
Combining this equation with the critical bed shear stress defined by Shields (Equation 2.16), the following expression of the Shields parameter is made:

$$\psi_b = \frac{\beta}{c_2}\left(\frac{d_{50f} \cdot i_c}{\Delta_b \cdot d_{50b}}\right) \tag{A.62}$$

The Klein Breteler formula (Equation A.59) did not include near-bed pressure fluctuations. However, the Bakker/Konter-formule does include the near bed-pressure fluctuations [CUR, 2010]:

$$\frac{d_{15f}}{d_{50b}} = \frac{2.2}{C_0 e^2}\frac{R}{d_{50f}}\frac{\psi_{c,b}}{\psi_{c,f}}\frac{\Delta_b}{\Delta_f} \quad \Rightarrow \quad \frac{1}{d_{15f}} = \frac{C_0 e^2}{2.20}\frac{d_{50f}}{d_{50b}R}\frac{\psi_{c,f}}{\psi_{c,b}}\frac{\Delta_f}{\Delta_b} \tag{A.63}$$

in which:

- C_0 turbulence coefficient that varies from 6 (for using time- and space-averaged bed shear stress) to 100 (for maximum bed shear stress) and commonly 15 [-];
- e coefficient that takes the difference of the flow in granular filters and open channels into account and is usually 0.24 [-].

Wörman investigated granular open filter at piers in 1989 [CUR, 2010]. He derived an equation in which the minimal filer layer thickness D_f could be determined by a certain filter and base diameter [Verheij et al., 2012]:

$$\frac{D_f}{d_{50f}} = 0.16\frac{n_f}{1-n_f}\frac{d_{85f}}{d_{85b}}\frac{\Delta_f}{\Delta_b} \tag{A.64}$$

Wörman did only experiments with small filter layer thicknessess ($D_f < 0.1$ m) and low average velocities ($\bar{u} < 0.5$ m/s) [Joustra, 2013].

Hoffmans (2000) presented a new design formula which is based on a theoretical approach [Verheij et al., 2012]:

$$\frac{D_f}{d_{15f}} = \alpha_d \ln\left(\frac{d_{50f}}{d_{50B}}\frac{\Delta_f}{\Delta_b}\frac{\Psi_{c,f}}{\Psi_{c,b}}\frac{1-\gamma V_f}{1-\gamma V_b}\right) \tag{A.65}$$

in which:

- α_d The load damping coefficient which describes the damping of the turbulent kinetic energy by the filter [-]. Proposed value of $\alpha_d = 1.5$;
- γ Transport parameter (=0.625 [-]);
- V_f Variation coefficient representing the non-uniformity of the filter material ($V_f = 1 - d_{15f}/d_{50f}$ [-];
- V_b Variation coefficient representing the non-uniformity of the base material ($V_b = 1 - d_{15b}/d_{50b}$ [-].

Note: this equation is based on the philosophy of simultaneous erosion of the filter material and bed material [Joustra, 2013].

Van de Sande showed that Equation A.65 is valid for single layerd geometrically open filter structeres loaded by current and showed that two adjustments would lead to better representative outcome [van de Sande et al., 2014]:

- The relative layer thickness fits better when it is related to the median sieve diameter (d_{50f}) of the filter material;
- The α_d value on d_{15f} is too conservative.

Van de Sande proposed a new formula, which is based on the Hoffmans formula [van de Sande et al., 2014]:

$$\frac{D_f}{d_{50f}} = \alpha_d \ln\left(\frac{d_{50f}}{d_{50b}}\frac{\Delta_f}{\Delta_b}\frac{\Psi_{c,f}}{\Psi_{c,b}}\frac{1-\gamma V_f}{1-\gamma V_b}\right) \tag{A.66}$$

With values of α_d:

Deterministic approach	Probabilistic approach (log-normal distribution)
$\alpha_d = 0.82$, safe upper-limit	$E(\alpha_d) = 0.46$
$\alpha_d = 0.69$, 90 % confidence limit	$Var(\alpha_d) = 0.03$

Using this formula two steps are needed:

1. Determine the required filter material to withstand the currents (e.g. using Shields parameter);
2. Determine the required layer thickness by given filter and base materials by using Equation A.66.

Note: when using this formula the properties of the chosen filter material should be used and not the dimensions calculated in step one.

A.10 Size vortices

In order to determine the state of turbulent flow, i.e. the length and time scale of one vortex, measures of different scales describing turbulence are needed. Two existing quantities are used:

- The velocity correlation function
- The energy spectrum.

Consider only the one-dimensional fluctuation in x direction, so u(x,t). When the correlation is computed between one time series in x direction and the same time series lagged by one or more time units (τ), a so-called autocorrelation is created. The autocorrelation coefficient (r_k) is a the simple correlation coefficient of N-1 observations:

$$r_k = \frac{c_k}{c_0} = \frac{c_k}{\sigma} \tag{A.67}$$

$$r_k(k) = \frac{\frac{1}{N}\sum_{t=1}^{N-k}(u'(x,t) * u'(x,t+\tau))}{\frac{1}{N}\sum_{t=1}^{N-k}(u'(x,t) * u'(x,t))} \tag{A.68}$$

The autocorrelation function can be plotted against the lag time. Thereafter, the duration over which the velocities are correlated can be calculated, e.g. the duration of an eddy turnover. The

Taylor macro-scale is related to the time scale of large turbulent structures and is determined by the integration of the autocorrelation function:

$$T_{char} = \int_0^\infty R(\tau) d\tau \tag{A.69}$$

The Taylor macro-scale motions are important for turbulent diffusion and transport momentum. The Taylor micro-structure (λ_τ) is defined by the curvature at the origin of the velocity correlation function. This depends on the smallest eddies [Sagaut, 2013]:

$$\lambda_\tau = \sqrt{-\frac{2}{\frac{d^2R}{d\tau^2}|_{t=0}}} \tag{A.70}$$

So far, only the time scale of turbulent properties are considered. In reality however, length scales are observed as well. The length is calculated by means of the Taylor's hypothesis: from a observation point the eddies will pass during the time interval L/$\overline{u}$, which L the size of the eddy and $\overline{u}$ the local mean flow speed. In this case calculation of the length scale is possible:

$$L_{char} = \overline{u} * T_{char} \tag{A.71}$$

Note that the Taylor's hypotheses assumes a frozen turbulence approximation: the eddy does not change during the passage time and the fluctuation caused by the eddy does not affect the transport velocity significantly. Smaller eddies are also present. The turbulent energy from these smallest eddies will be converted into heat and is can be calculated by the Kolmogorov scale.

B Grading curves Sand

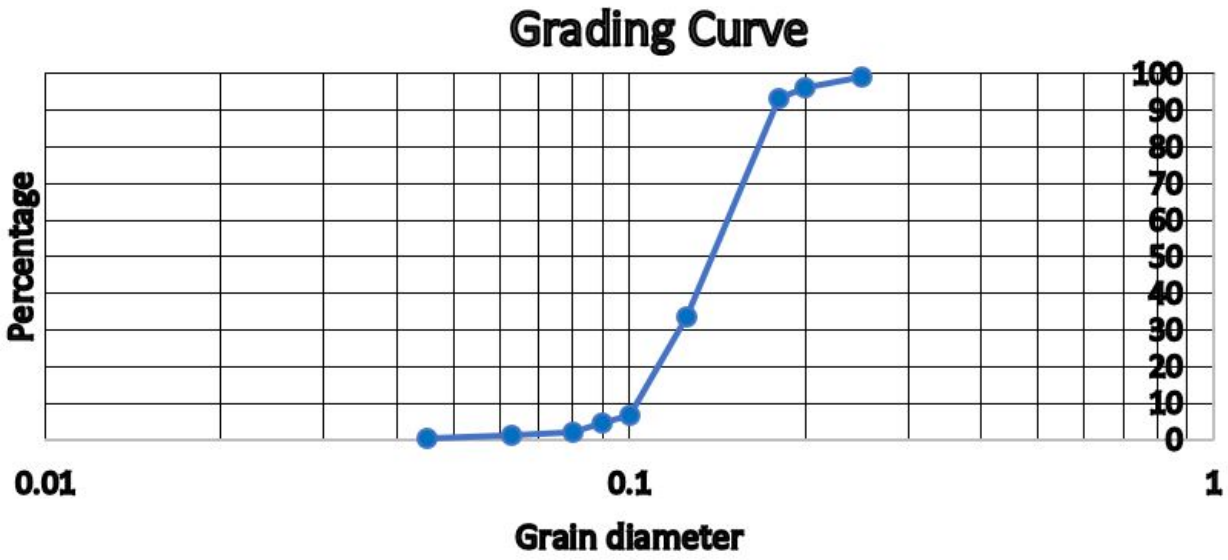

Figure B.1: Grading curve of the sand.

C Results velocity measurements

C.1 Time steps characteristics per experiment

The characteristic flow conditions of each time step of all experiments are given in this section. In each experiment, the discharge is increased and the height of the weir is adjusted to maintain similar water levels during the experiment. At location 1, 2, and 5 the water levels are determined by subtracting the measured bed level from the measured water level. For locations 3, 4 and 6 this is not possible, since the bed is lower due to the filter. For those location, the water level for the given location relative to the bed level at location 2 is used. During the first and second set of experiments (experiments R01, R02, R03, R04, R05 and R06) the water level is measured at all the locations. In the third set of experiments (experiment R07, R08 and R09) the water level is only measured at location 1, 2 and at the end of the filter. The water levels between these locations are calculated means of a linear approximation.

Table C.1: Time step characteristics experiment R01.

t	Q [l/s]	h_{weir} [cm]	h_{loc1} [cm]	h_{loc2} [cm]	h_{loc3} [cm]	h_{loc4} [cm]	h_{loc5} [cm]	h_{loc6} [cm]
t1	10.2	30	22.32	22.05	22.05	22.05	22.14	21.98
t2	20.1	27	22.62	22.25	22.28	22.15	22.22	22.15
t3	30.8	24	22.54	22.25	22.03	22.00	21.87	22.03
t4	41.5	21	22.04	21.31	21.31	20.96	20.74	21.13
t5	46.0	19	20.67	18.78	19.67	19.53	19.15	19.54
t6	50.9	18	20.35	19.35	19.50	19.09	18.97	19.38
t7	55.7	18	21.53	20.53	20.55	19.88	19.77	20.26

Table C.2: Time step characteristics experiment R02.

t	Q [l/s]	h_{weir} [cm]	h_{loc1} [cm]	h_{loc2} [cm]	h_{loc3} [cm]	h_{loc4} [cm]	h_{loc5} [cm]	h_{loc6} [cm]
t1	26.7	30	21.60	21.05	21.03	20.96	20.98	20.96
t2	40.5	27	21.76	21.16	21.15	20.76	20.64	20.83
t3	46.5	24	20.83	20.05	19.92	19.40	18.83	19.86
t4	53.1	21	21.20	20.15	19.91	19.56	19.25	19.86
t5	56.2	19	21.83	20.28	20.27	19.32	19.39	20.27

Table C.3: Time step characteristics experiment R03.

t	Q [l/s]	h_{weir} [cm]	h_{loc1} [cm]	h_{loc2} [cm]	h_{loc3} [cm]	h_{loc4} [cm]	h_{loc5} [cm]	h_{loc6} [cm]
t1	26.7	24	21.53	21.13	21.16	21.04	20.98	21.09
t2	40.2	21	21.57	21.00	21.04	20.70	20.43	20.88
t3	45.7	19	20.75	20.00	20.03	19.31	18.58	19.77
t4	46.7	19	21.03	20.13	20.18	19.62	19.06	20.12
t5	50.4	19	21.60	20.64	20.70	19.72	20.10	20.63
t6	53.5	18	21.00	19.98	20.03	19.59	18.46	19.88
t7	56.5	18	22.05	21.03	20.54	20.13	19.46	20.27

Table C.4: Time step characteristics experiment R04.

t	Q [l/s]	h_{weir} [cm]	h_{loc1} [cm]	h_{loc2} [cm]	h_{loc3} [cm]	h_{loc4} [cm]	h_{loc5} [cm]	h_{loc6} [cm]
t1	25.1	24	21.40	20.78	21.10	20.55	20.47	20.5
t2	30.4	23	21.85	21.17	21.15	21.00	20.73	21.05
t3	40.2	21	22.20	21.35	21.30	21.05	20.52	21.11
t4	44.9	19	21.02	20.02	19.88	19.50	18.99	19.75
t5	50.2	19	22.02	20.97	20.95	20.44	19.82	20.72

Table C.5: Time step characteristics experiment R05.

t	Q [l/s]	h_{weir} [cm]	h_{loc1} [cm]	h_{loc2} [cm]	h_{loc3} [cm]	h_{loc4} [cm]	h_{loc5} [cm]	h_{loc6} [cm]
t1	25.0	24	21.36	20.74	20.72	20.54	20.49	20.60
t2	30.5	23	21.65	21.05	21.01	20.75	20.59	20.90
t3	40.5	21	22.18	21.30	21.32	20.89	20.53	21.18
t4	45.0	19	21.00	20.01	19.95	19.19	18.62	19.26
t5	50.1	19	22.02	20.82	20.80	20.10	19.90	20.23
t6	55.6	18	22.07	20.77	21.00	19.90	19.74	20.35

Table C.6: Time step characteristics experiment R06.

t	Q [l/s]	h_{weir} [cm]	h_{loc1} [cm]	h_{loc2} [cm]	h_{loc3} [cm]	h_{loc4} [cm]	h_{loc5} [cm]	h_{loc6} [cm]
t1	30.2	23	21.82	21.25	21.08	20.90	20.66	20.95
t2	39.6	21	22.03	21.19	21.13	20.85	20.49	21.03
t3	44.9	19	21.09	20.08	20.03	19.88	18.80	19.80
t4	50.2	19	23.80	22.95	22.92	22.49	21.87	22.80
t5	54.8	18	21.82	20.52	20.50	19.97	19.37	20.34
t6	60.0	18	22.95	21.65	21.33	20.97	20.37	21.15

Table C.7: Time step characteristics experiment R07.

t	Q [l/s]	h_{weir} [cm]	h_{loc1} [cm]	h_{loc2} [cm]	h_{loc3} [cm]	h_{loc4} [cm]	h_{loc5} [cm]	h_{loc6} [cm]
t1	44.7	24.0	20.87	19.73	19.34	18.62	18.45	18.91
t2	49.7	22.8	21.56	20.32	19.99	19.37	19.22	19.62
t3	54.8	22.5	21.86	20.46	20.12	19.49	19.34	19.74
t4	60.0	21.8	22.34	20.8	20.19	19.05	18.77	19.50
t5	64.4	21.2	25.06	21.63	20.91	19.57	19.25	20.11

Table C.8: Time step characteristics experiment R08.

t	Q [l/s]	h_{weir} [cm]	h_{loc1} [cm]	h_{loc2} [cm]	h_{loc3} [cm]	h_{loc4} [cm]	h_{loc5} [cm]	h_{loc6} [cm]
t1	39.7	24.0	21.07	20.08	19.84	19.39	19.2548	19.57
t2	44.8	22.8	20.77	19.67	19.32	18.68	18.52	18.94
t3	50.2	22.5	21.68	20.46	20.00	19.14	18.94	19.49
t4	55.4	21.8	21.93	20.55	20.14	19.37	19.18	19.68
t5	60.7	21.2	22.37	20.83	20.34	19.43	19.21	19.80

Table C.9: Time step characteristics experiment R09.

t	Q [l/s]	h_{weir} [cm]	h_{loc1} [cm]	h_{loc2} [cm]	h_{loc3} [cm]	h_{loc4} [cm]	h_{loc5} [cm]	h_{loc6} [cm]
t1	39.9	24.0	21.06	20.13	19.89	19.45	19.32	19.63
t2	44.6	22.8	20.82	19.73	19.43	18.87	18.70	19.09
t3	49.5	22.5	21.54	20.38	19.93	19.08	18.85	19.42
t4	55.0	21.8	21.42	20.51	20.03	19.13	18.89	19.49
t5	59.8	21.2	22.24	20.78	20.23	19.21	18.92	19.62
t6	65.0	20.5	22.56	20.91	20.25	19.03	18.68	19.52

C.2 Measured heights

C.2.1 Above the filter

Table C.10: Measured heights ADV1 relative to the bottom of the flume at location 3 of all experiments.

	Measured height [cm]								
Measurement	R01	R02	R03	R04	R05	R06	R07	R08	R09
1	25.7	25.7	25.7	28.7	28.7	28.7	31.0	31.0	31.0
2	23.7	21.7	22.7	25.7	25.7	25.7	29.5	29.5	29.5
3	21.7	18.7	20.7	22.7	22.7	22.7	26.5	26.5	26.5
4	19.7	16.7	18.7	20.7	20.7	20.7	24.5	24.5	24.5
5	17.7	15.7	17.7	18.7	18.7	18.7	22.5	22.5	22.5
6	16.7	14.7	16.7	17.7	17.7	17.7	21.5	21.5	21.5
7	15.7	13.7	15.7	16.7	16.7	16.7	20.5	20.5	20.5
8	14.7	12.7	15.2	15.7	15.7	15.7	19.5	19.5	19.5
9	13.7	11.7	14.7	15.2	15.2	15.2	-	-	-
10	12.7	10.7	14.2	14.7	14.7	14.7	-	-	-
11	11.7	-	13.7	-	-	-	-	-	-

C.2.2 Inside the filter

Table C.11: Measured height ADV2 relative to the bottom of the flume at location 3 for the first set of experiments (R01, R02 and R03).

Measurement	Measured height [cm]					
1	13.2	13.0	12.8	12.6	12.4	12.2
2	12.2	12.0	11.8	11.6	11.4	11.2
3	11.2	11.0	10.8	10.6	10.4	10.2
4	10.2	10.0	9.8	9.6	9.4	9.2

Table C.12: Measured heights ADV2 relative to to the bottom of the flume at location 3 for the second set of experiments (R04, R05 and R06).

Measurement	Measured height [cm]					
1	11.8	11.6	11.4	11.2	11.0	10.8
2	10.8	10.6	10.4	10.2	10.0	9.8
3	9.8	9.6	9.4	9.2	9.0	8.8
4	8.8	8.6	8.4	8.2	8.0	7.8
5	7.8	7.6	7.4	7.2	7.0	6.8
6	6.8	6.6	6.4	6.2	6.0	5.8
7	5.8	5.6	5.4	5.2	5.0	4.8

Table C.13: Measured heights ADV2 relative to to the bottom of the flume at location 3 of experiment R07 and R08.

Measurement	Measured height [cm]					
1: R07	9.6	9.4	9.2	9.0	8.8	8.6
1: R08	9.8	9.6	9.4	9.2	9.0	8.8
2	8.8	8.6	8.4	8.2	8.0	7.8
3	7.8	7.6	7.4	7.2	7.0	6.8
4	6.8	6.6	6.4	6.2	6.0	5.8
5	5.8	5.6	5.4	5.2	5.0	4.8

Table C.14: Measured heights ADV2 relative to to the bottom of the flume at location 3 of experiment R09.

Measurement	Measured height [cm]					
1	10.3	10.1	9.9	9.7	9.5	9.3
2	9.8	9.6	9.4	9.2	9.0	8.8
3	8.8	8.6	8.4	8.2	8.0	7.8
4	7.8	7.6	7.4	7.2	7.0	6.8
5	6.8	6.6	6.4	6.2	6.0	5.8
6	5.8	5.6	5.4	5.2	5.0	4.8

C.3 Neglected measurements

C.3.1 Third measurement of ADV1 in experiment R01 and R03

In experiment R01 and R03, the third measurement provides velocities which are much lower than in theory should be. An example is given in figure C.1. Here, the velocity profile in x, y and z-direction of experiment R01 is given. The measured velocities in between $z/h = 0.3$ and $z/h = 0.4$ reach zero. When looking at the signal, these measured velocities is not reliable, see Figure. Therefore, this measurement, and also the third measurement of each time step in experiment R03, is not taken into account.

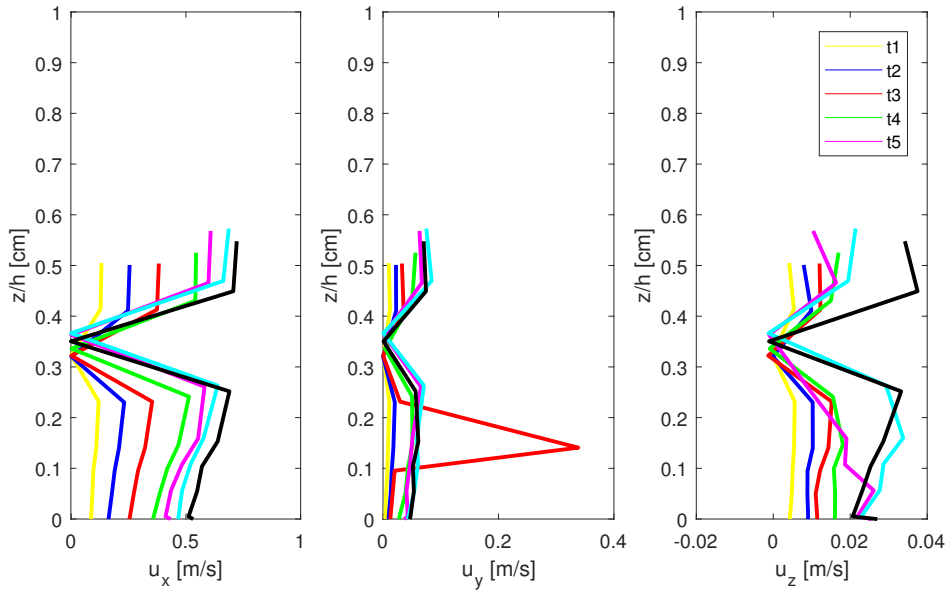

Figure C.1: Velocity profile in x, y and z-direction of experiment R01. The measured velocities in between $z/h = 0.3$ and $z/h = 0.4$ give unreliable velocities.

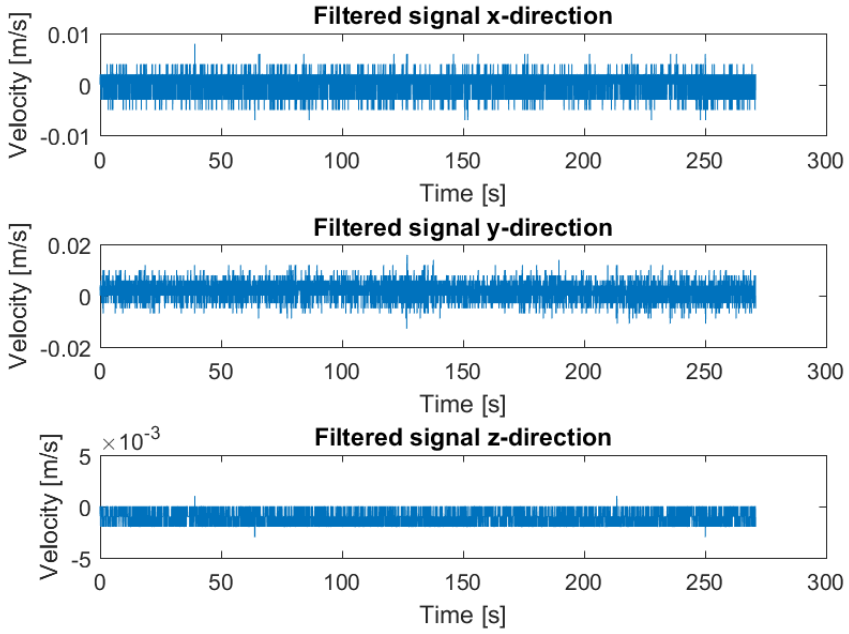

Figure C.2: Measured velocity at $z = 21.7$ cm in x, y and z-direction of the fifth time step of experiment R01. The measured velocities gives non-reliable results.

C.3.2 Experiment R01: time step 3 measurement 5

The signal of the flow velocity in y-direction in measurement 5 in time step 3 of experiment R01 gave a non reliable output. The signals was only fluctuating on 0 and 0.5 m/s, see Figure C.3. For that reason, the signal is not taken into account in the analysis of the flow above the filter.

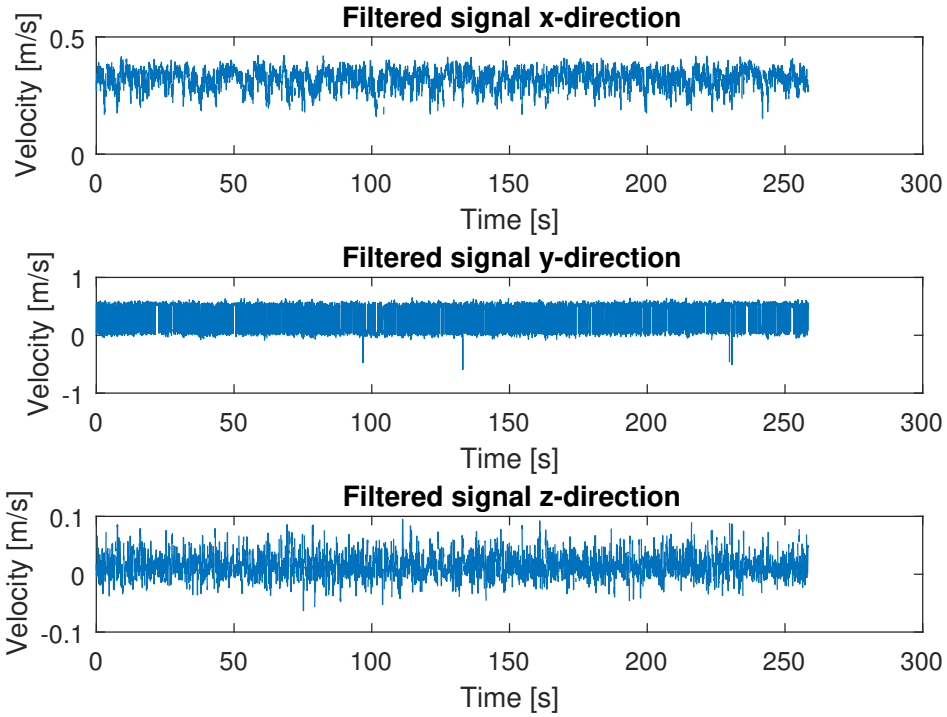

Figure C.3: Output signal of measurement 5 of Experiment R01 time step 3. The signal in y-direction gives non-reliable output.

C.3.3 Lowest measurement of ADV2 in each time step of each experiment

The lowest measurement of the ADV2 in each experiments was influenced by boundaries, i.e. the bed or the log of the next layer. For example, we consider the lowest measurement of experiment R09, Table C.14, the sample volume between 4.8 and 5.8 cm relative to the bottom of the flume. The false bottom itself is placed at 5 cm. Hence, the sample volume of the ADV2 partly in the bed. The result of the measured velocities of 5.2 cm of experiment R09 in the last time step is given in Figure C.4. It is visible that the output of the signal does not provides reasonable results. Since this signal is present for the lowest measurement of the ADV2 in each experiment, these measurements are neglected. This also occur when the sample volume reaches depths in which a logs is located.

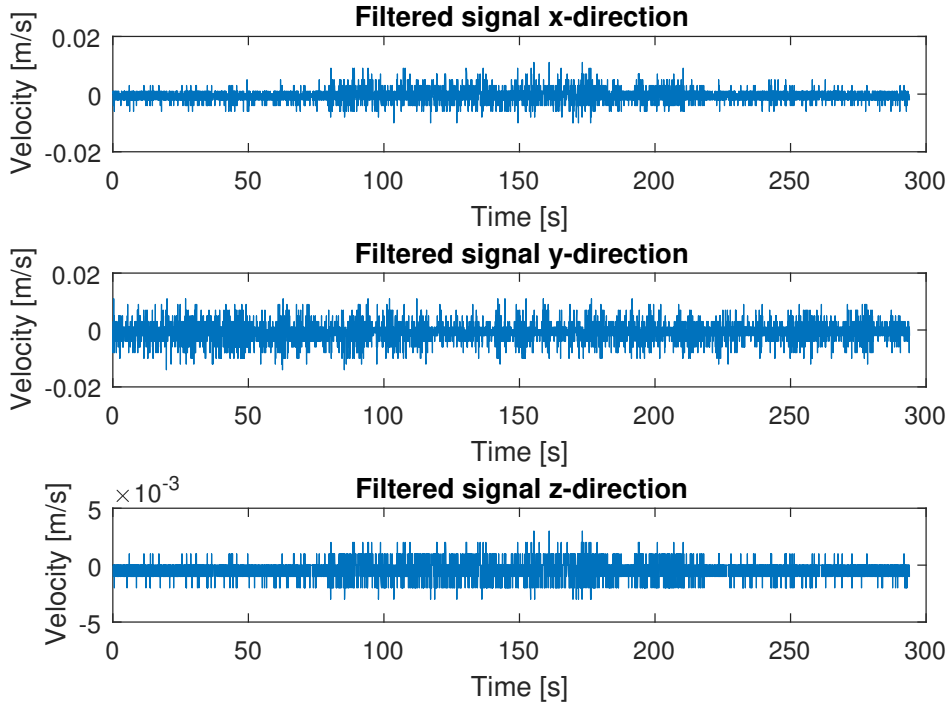

Figure C.4: The non-reliable measured velocities in x,y- and z-direction of measurement 6 of Experiment R09 in time step 6.

C.4 Results velocity measurements above filter

C.4.1 Measured average velocities

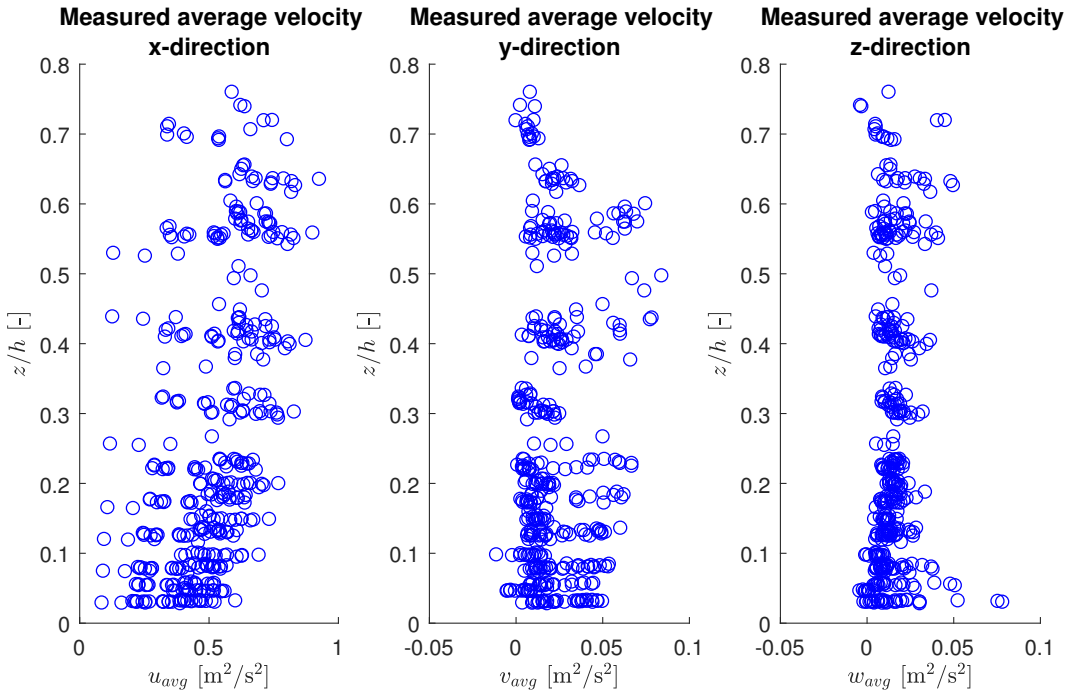

Figure C.5: Measured average velocities in x, y and z-direction.

C.4.2 Measured fluctuation velocities

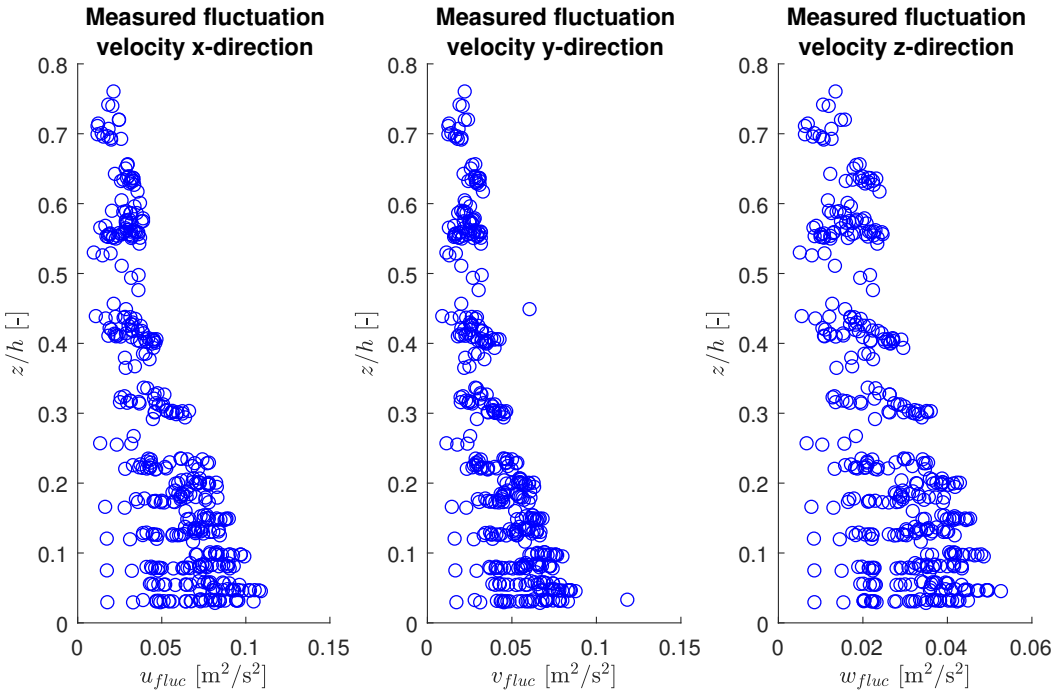

Figure C.6: Measured fluctuation velocities in x, y and z-direction.

Therefore, the average velocities and average fluctuation velocities over depth in all directions of all experiments are plotted in Figures C.7 and C.8, respectively. Again, the depth is relative to the diameter of a log.

C.5 Results velocity measurements inside filter

C.5.1 Mean flow velocities in all direction of all experiments

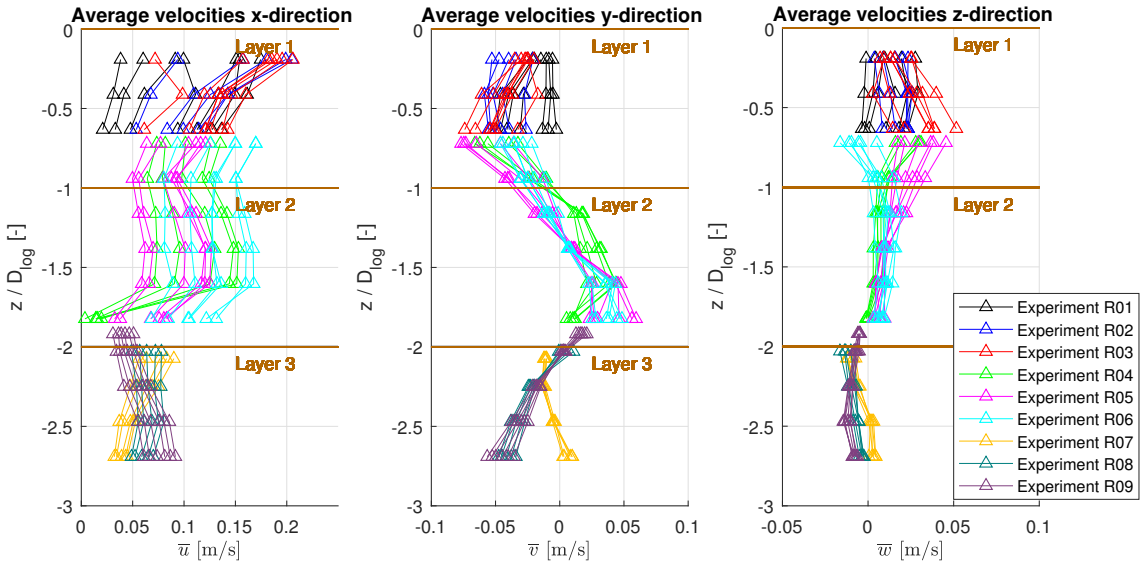

Figure C.7: Mean flow velocities in all directions of all experiments over depth inside the filter.

C.5.2 Fluctuation velocities in all direction of all experiments

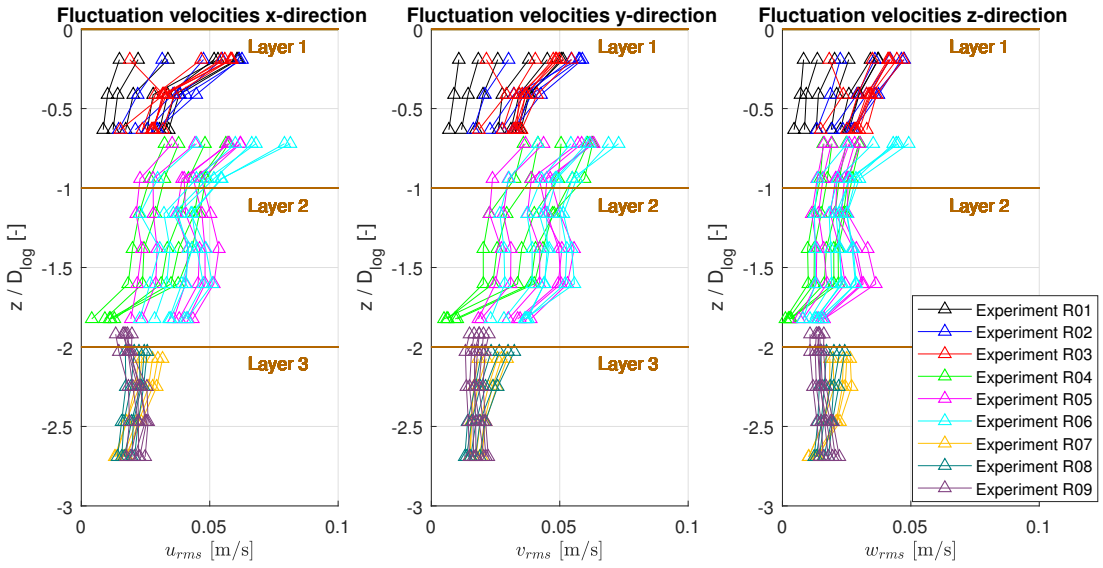

Figure C.8: Fluctuation velocities in all directions of all experiments over depth inside the filter.